Engineered Systems for Controlled Hypoxia and Thermogenesis

BY

MEGAN L. REXIUS

B.S., Boston University, 2009

THESIS

Submitted as partial fulfillment of the requirements
for the degree of Doctor of Philosophy in Bioengineering
in the Graduate College of the
University of Illinois at Chicago, 2017

Chicago, IL

Defense Committee:

David Eddington, Chair and Advisor
Jalees Rehman, Pharmacology and Division of Cardiology
Christos Takoudis, Bioengineering
Salman Khetani, Bioengineering
Ian Papautsky, Bioengineering

ACKNOWLEDGEMENTS

First and foremost, I am deeply grateful to my co-advisors, Dr. David Eddington and Dr. Jalees Rehman, for their continuous support and guidance. They have significantly contributed to my development as an engineer and a scientist, and I have appreciated their mentorship, patience, and input. I have greatly benefited from our exchange of ideas.

I would also like to thank the Department of Pharmacology for supporting me as a trainee on the NIH T32 Lung Biology and Pathobiology Training Grant during my initial years of study.

A special thanks goes to the Graduate College and the Dean's Scholar Fellowship selection committee for having enough confidence in me and my work to support the final year of my PhD research.

I sincerely thank Gerardo Mauleon for his oxygen measurements of several landscape designs, Dr. Ben Olenchock for his analysis of the metabolomics samples, the Advanced Imaging Center at the Howard Hughes Medical Institute Janelia Research Campus for use of their lattice light sheet microscope, and Seiichi Uchiyama for providing the ratiometric intracellular temperature thermometer.

Finally, to my colleagues, the laboratory experience is enhanced by those with whom you share it. Thank you for your knowledge, advice, and thoughtful discussions. You have been the most valuable resource when I've needed help.

Some parts of this thesis are reproduced from my published works [1, 2] with permission from the Royal Society of Chemistry.

CONTRIBUTION OF AUTHORS

Rexius-Hall, M. L., Mauleon, G., Malik, A.B., Rehman, J., and Eddington, D.T. (2014) Microfluidic platform generates oxygen landscapes for localized hypoxic activation, Lab Chip. 14(24):4688-95

Megan L. Rexius-Hall conceived and designed experiments, performed experiments, acquired data, analyzed data, drafted the manuscript, and revised the manuscript

Gerardo Mauleon acquired data and analyzed data

Asrar B. Malik conceived and designed experiments and revised the manuscript

Jalees Rehman conceived and designed experiments, interpreted data, and revised the manuscript

David T. Eddington conceived and designed experiments, interpreted data, and revised the manuscript

Brennan, M.D., Rexius-Hall, M.L., Elgass, L.J., and Eddington, D.T. (2014) Oxygen control with microfluidics, Lab Chip. 14(22):4305-18

Martin D. Brennan conducted literature review, interpreted research, drafted the manuscript, revised the manuscript, and finalized the submission for publication

Megan L. Rexius-Hall conducted literature review, interpreted research, drafted the manuscript, and revised the manuscript

Laura J. Elgass conducted literature review, interpreted research, drafted the manuscript, and revised the manuscript

David T. Eddington conceived the work and revised the manuscript

TABLE OF CONTENTS

1 INTRODUCTION AND BACKGROUND **1**

1.1 Engineered Microenvironments for Controlled Hypoxia . . . 1
1.1.1 Oxygenation of Cells and Tissues . . . 1
1.1.2 Hypoxic Signaling . . . 2
1.1.2.1 Hypoxia Inducible Factor (HIF) Family of Transcription Factors . . . 2
1.1.2.2 Differences Between HIF-1α and HIF-2α . . . 3
1.1.2.3 Biological Assessment of HIF Activation . . . 3
1.1.2.4 Chemical Induction of HIF . . . 4
1.1.3 Methods to Control Homogeneous Oxygenation . . . 5
1.1.3.1 Hypoxic Chambers . . . 5
1.1.3.2 Hypoxia Workstations . . . 6
1.1.3.3 Perfusion Chambers . . . 7
1.1.3.4 Motivation for Microfluidic Tools . . . 7
1.1.4 Diffusion, Solubility, and Transport of Oxygen in Microfluidic Devices 7
1.1.5 Measurement of Oxygen . . . 11
1.1.5.1 Clark-style electrodes . . . 11
1.1.5.2 Luminescent optical sensors . . . 12
1.1.6 Oxygen Control with Microfluidic Devices . . . 13
1.1.6.1 Diffusion from a Source Fluid . . . 14
1.1.6.2 Discrete Series of Constant Oxygen Concentrations . . . 17
1.1.6.3 Constant Oxygen Concentration . . . 19
1.1.6.4 Hydration Layer . . . 22
1.1.6.5 Binary Oxygen Environment . . . 24
1.1.7 Oxygen Gradients . . . 25
1.1.7.1 *In Vivo* Oxygen Gradients . . . 25
1.1.7.2 Generation of Microfluidic Oxygen Gradients . . . 26
1.2 Engineered Systems for Controlled Thermogenesis . . . 31
1.2.1 Temperature in Biological Systems . . . 31
1.2.2 Methods to Control Temperature . . . 31
1.2.2.1 Microenvironmental Temperature . . . 32
1.2.3 Engineered Temperature Control Platforms . . . 32
1.2.3.1 Peltiers . . . 34
1.2.4 Nonshivering Thermogenesis . . . 35
1.2.4.1 White, Beige, and Brown Adipocytes . . . 36
1.2.4.2 Brown Adipose Tissue in Humans . . . 37
1.2.4.3 Cold Exposure Induces Thermogenesis . . . 39
1.2.4.4 Therapeutic Potential . . . 39
1.2.4.5 Biological Assessment of Thermogenesis . . . 41

2 MATERIALS AND METHODS **44**
2.1 Large-Area Oxygen Landscape Cell Culture Platform . . . 44
2.1.1 Open-well Device Design . . . 44
2.1.2 Device Fabrication . . . 44
2.1.2.1 Dual Condition Device . . . 48
2.1.3 Oxygen Modulation Setup . . . 49
2.1.4 Oxygen Sensor Fabrication . . . 50
2.1.5 Oxygen Profile Validation . . . 50
2.1.6 Dissolved Oxygen Measurements . . . 51
2.1.7 Cell Culture . . . 51
2.1.8 In-device Immunofluorescent Staining . . . 52
2.1.9 Protein Extractions and Western Blotting . . . 52
2.1.10 Quantitative Real-time PCR . . . 53
2.1.11 Statistical Analysis . . . 54
2.2 Linear Oxygen Gradient Device . . . 54
2.2.1 Device Fabrication . . . 54
2.2.2 Oxygen Modulation Setup . . . 56
2.2.3 Oxygen Sensor Fabrication . . . 56
2.2.4 Oxygen Profile Validation . . . 56
2.2.5 Cell Culture . . . 58
2.2.6 In-device Immunofluorescent Staining . . . 58
2.2.7 Microscopy and Image Analysis . . . 59
2.2.8 Statistical Analysis . . . 59
2.3 Temperature Control of the Adipocyte Microenvironment . . . 60
2.3.1 Preadipocyte and Adipocyte Cell Culture . . . 60
2.3.2 Introduction of the Fluorescent Thermoprobe into Cells . . . 60
2.3.3 Confocal Microscopy and Image Analysis . . . 61
2.3.4 Lattice Light Sheet Microscopy and Image Analysis . . . 61
2.3.5 Quantitative Real-time PCR . . . 62
2.3.6 Immunoblot Analysis . . . 62
2.3.7 Extracellular Flux Analysis . . . 63
2.3.8 Metabolomics . . . 63
2.3.9 Statistical Analysis . . . 64
2.4 Temperature Gradient Co-culture Platform . . . 64
2.4.1 Platform Design . . . 64
2.4.2 COMSOL Temperature Simulation . . . 66
2.4.3 Cell Culture . . . 66
2.4.4 Temperature-controlled Co-culture . . . 66
2.4.5 Quantitative Real-time PCR . . . 67

3 RESULTS **68**
3.1 Large-area Oxygen Landscapes . . . 68
3.1.1 Dual Condition Oxygen Landscape . . . 68
3.1.2 Hypoxic Response of Human Microvascular Endothelial Cells . . . 70

3.1.3 Metabolic Specificity of Bone Marrow-derived Mesenchymal Stem Cells . . . 72
3.1.4 Differential Expression of Genes in the Oxygen Landscape . . . 73
3.2 Stable Linear Oxygen Gradients . . . 75
3.2.1 Linear Gradient Profile . . . 76
3.2.2 Linear Gradient in the Presence of Cells . . . 76
3.2.3 HIF-1α Activation . . . 78
3.2.4 HIF-2α Activation . . . 79
3.3 Adipocyte Cold Exposure . . . 81
3.4 Characterization of Adipogenic Differentiation . . . 81
3.4.1 Intracellular Temperature Increases in Adipocytes Exposed to Cold . . . 81
3.4.2 Adipogenic Differentiation Enhances Glycolysis . . . 84
3.4.3 Cold Exposure Increases Glucose Uptake and Metabolic Flux . . . 88
3.4.4 Glycolysis is Required for Rapid Cold-induced Thermogenesis . . . 89
3.5 Adipocyte Co-culture Platform . . . 91
3.5.1 Temperature Gradient Simulation . . . 91
3.5.2 PGC1α mRNA Upregulation in Adipocytes Exposed to Cold . . . 92
3.5.3 Modulation of Thermogenic Signaling in a Temperature Gradient . . . 95

4 DISCUSSION **98**
4.1 Large-area Oxygen Landscapes . . . 98
4.2 Dual Condition Oxygen Landscape Device . . . 99
4.2.1 Limitations and Future Directions . . . 101
4.3 Stable Linear Oxygen Gradient Device . . . 104
4.4 Cold-induced Adipocyte Thermogenesis . . . 107
4.5 Temperature-Controlled Adipocyte Co-culture Platform . . . 110
4.6 Conclusion . . . 112

A Protein Lysis Protocol **114**

B Western Blot Protocol **116**

C PCR Protocol **121**

D Stern-Volmer Code **122**

E COMSOL Material Properties in the Heat Transfer Simulation **123**

F Peltier Thermoelectric Device Specifications **124**

G Copyright Permissions Statement **125**

CITED LITERATURE **127**

LIST OF TABLES

1.1 The physiologic oxygen levels vary for different human tissues. The indicated normoxic levels are all below atmospheric (21%) oxygen. Values compiled from refs. [3–6]. 1
1.2 Differences among the three types of adipocytes. Adapted from [114] 38

C.1 cDNA Synthesis Reagent Volumes 121
C.2 cDNA Synthesis Thermocycle 121
C.3 PCR Reaction Reagent Volumes 121

LIST OF FIGURES

1.1 An off-chip bubbling experimental setup demonstrates generation of an oxygen gradient using equilibrated liquid. Reproduced from ref. [53]. 15
1.2 An early microfluidic bioreactor demonstrates enhanced oxygen modulation. Reproduced with permission from ref. [54]. 17
1.3 Two devices for generating discrete series of gas concentrations in chambers for various cultures. In the drawing of the two devices in (A) and (B) the gray serpentine mixing channels determine the dissolved gas environment of the culture region (black vertical channels). The individual lengths of the serpentine channels vary in the two devices to determine the degree of mixing from the two gas inlets. Reproduced from ref. [46] 19
1.4 Oppegard *et al.* microfluidic insert for 6-well plate with Boyden chamber. Reproduced from ref. [58]. 20
1.5 Microbioreactor with *in situ* oxygen sensors for live computer oxygen monitoring. Reproduced with permission from ref. [59]. 21
1.6 A hydration layer of PBS between the gas layer and blood layer prevents dehydration of the blood sample. Reproduced with permission from ref. [64]. 24
1.7 A hydration layer is incorporated into this device to prevent dehydration of bacterial cell culture chambers. The green layer is gas, the purple is the hydration layer, and the blue is the culture chamber. Reproduced from ref. [63]. 24
1.8 Lo *et al.* devices with associated oxygen concentrations. The inlets were supplied with a 100% and 0% oxygen source. Oxygen measurements demonstrated the gradient profiles generated from each mixing design. Reproduced from ref. [74]. 27
1.9 Modeling of the oxygen gradient in a flat-plate bioreactor with dimensions of 28 mm x 55 mm and 100 μm in height. Computational models were created to produce a gradient depending on consumption of oxygen by a cell culture with media of different initial pO_2 levels and flow rates. An example gradient predicted by the model with inlet pO_2 of 158 mmHg and a media flow rate of .035 mL/min demonstrates a linear gradient across the bioreactor as media flow from left to right (A). Measured experimental inlet and outlet pO_2 levels were compared to numerical and analytical model predictions for verification (B). Reproduced with permission from ref. [75]. . 28

1.10 (A) Schematic of an oxygen scavenging device showing the serpentine channel scavenging layer (red), separated by a thin PDMS layer (yellow) from the culture chamber (green) and the oxygen sensor lid (purple). (B) Image of the device with the serpentine scavenging channel (blue) and culture chamber (yellow). (C) A comparison of simulated oxygen gradients along the chamber (dotted lines) with measured oxygen levels (solid lines) under three different flow rates. (D) Images of stained bacteria in the device at different positions along the gradient. A culture at atmospheric conditions (above) is compared to a culture with a gradient applied resulting in oxygen saturations of 97%, 79%, 60%, and 41% from atmospheric (from left to right). Reproduced from ref. [77]. 29
1.11 (A) Schematic of a device that initiates oxygen-generating and oxygen-scavenging reactions with on-chip mixers, resulting in an oxygen gradient across a central cell culture channel. (B) Image of the device with the central cell culture channel (red) flanked by the chemical reaction channels (green and blue). (C) a cross-sectional view of the device shows the path of oxygen diffusion from the H_2O_2 + NaOCl channel across the culture channel to the Pyrogallol + NaOH channel where it is consumed. Reproduced from ref. [78]. 30
1.12 An oxygen scavenger flowing in a channel creates an oxygen gradient. Oxygen is depleted most in the center of the channel and against the gas impermeable wall and is replenished from the surrounding PDMS bulk. Reproduced from ref. [79]. 31
1.13 Schematic of the microfluidic device with a bidirectional flow syringe pump and two distinct temperature zones. Adpated from ref. [111]. 36

2.1 Oxygen Landscape Designs 45
2.2 Microfabrication of an SU-8 master 47
2.3 Large-area Open-well Cell Culture Platform 48
2.4 Open-well Schematic 49
2.5 Linear Gradient Schematic 55
2.6 Linear Gradient Oxygen Modulation Setup 57
2.7 Peltier Co-culture Design 65

3.1 Large-area Oxygen Validation 69
3.2 Dual Condition Oxygen Characterization 71
3.3 Hypoxic Response 72
3.4 Metabolic Genes in MSCs 74
3.5 Dual Condition Hypoxia Enhances PFKFB3 Compared to Homogeneous Hypoxia 75
3.6 Linear Oxygen Gradient Profile 77
3.7 Linear Gradient in the Presence of Cells 78
3.8 HIF-1α Activation 80
3.9 HIF-2α Activation 82
3.10 Characterization of Adipogenic Differentiation 83

3.11 Fluorescent Thermoprobe Demonstrates Cold-Induced Thermogenesis in Adipocytes . . . 85
3.12 Heat Production Maps to Mitochondria in Thermogenic Adipocytes . . . 86
3.13 Adipogenic Differentiation Upregulates Glycolytic Genes . . . 87
3.14 Adipogenic Differentiation Enhances Glycolysis . . . 88
3.15 Cold Exposure Enhances Glucose Uptake . . . 89
3.16 Cold Exposure Increases the ATP:ADP Ratio . . . 90
3.17 Cold Exposure Increases Metabolic Flux . . . 91
3.18 Impaired Glucose Metabolism Prevents Thermogenesis . . . 92
3.19 The Co-culture Platform Creates a Linear Temperature Gradient . . . 93
3.20 Sustained Cold Exposure Upregulates PGC1α mRNA . . . 94
3.21 Real-time PGC1α Upregulation in Cold . . . 95
3.22 A Temperature Gradient Modulates Gene Expression in Adipocytes . . . 97

E.1 The Material Properties of the Glass Coverslips. . . . 123
E.2 The Material Properties of the PDMS Gaskets. . . . 123
E.3 The Material Properties of the Cell Culture Media. . . . 123

F.1 The Specifications of the TE Device . . . 124

LIST OF ABBREVIATIONS

O_2	oxygen
CO_2	carbon dioxide
N_2	nitrogen
HIF	hypoxia inducible factor
PHD	prolyl hydroxylase
ODD	oxygen-dependent degradation domain
HRE	hypoxia response element
PCR	polymerase chain reaction
2-OG	2-oxoglutarate
$CoCL_2$	cobalt (II) chloride
DFO	desferrioxamine
DMOG	dimethyloxaloglycine
DHB	dihydrobenzoic acid
PDMS	polydimethylsiloxane
PTFE	polytetrafluoroethylene
FLIM	Fluorescence Lifetime Imaging Microscopy
PtOEPK	platinum (II) octaethylporphyrinketone
DO	dissolved oxygen
PMMA	polymethylmethacrylate
PC	poly carbonate
ECM	extracellular matrix
HbS	sickle cell hemoglobin
CO	carbon monoxide
pO_2	partial pressure of oxygen
PQM	Phosphorescence Quenching Microscopy
ROS	reactive oxygen species
TE	thermoelectric
PCB	printed circuit board
UCP1	uncoupling protein 1
BAT	brown adipose tissue
WAT	white adipose tissue
PET	positron emission tomography
FDG	2-[^{18}F]fluoro-2-deoxyglucose
GLUT	glucose transporter
CT	computer tomography
NE	norepinephrine
PKA	protein kinase A
FFA	free fatty acid
DNP	dinitrophenol
HFD	high fat diet
PGC1α	peroxisome proliferator-activated receptor-gamma coactivator
Dio2	iodothyronine deiodinase 2

CCCP	**carbonyl cyanide 3-chlorophenyl-hydrazone**
PS	**polystyrene**
HLMVEC	**human lung microvascular endothelial cell**
FBS	**fetal bovine serum**
PBS	**phosphate buffered saline**
MSC	**mesenchymal stem cell**
PDK	**pyruvate dehydrogenase kinase**
LDH	**lactate dehydrogenase**

For my parents whose curiosity and chosen careers in science and engineering have greatly influenced me, my 7th and 8th grade science teacher Pam Riss who gave me the confidence to pursue a STEM education, and my wonderful husband, Lance, who has been alongside me during these years I have sought my advanced degree.

SUMMARY

Cells adapt to microenvironmental alterations in oxygen levels and temperature by shifting metabolic processes and initiating transcriptional programs. Engineered systems have been developed to probe the biological responses of cells to their microenvironment. Our microfluidic platforms for gas control have allowed us to generate oxygen landscapes and gradients found in the physiological setting as a result of metabolic consumption and oxygen transport limitations. For gas control, we studied the hypoxic activation of the hypoxia inducible factor (HIF) family of transcription factors HIF-1α and HIF-2α in human endothelial cells, and we demonstrated differential hypoxic activation of HIF-1α and HIF-2α in a spatial linear oxygen gradient. Our temperature control studies have focused on nonshivering thermogenesis in human subcutaneous adipocytes. We used a ratiometric cell-permeable thermoprobe to demonstrate intracellular heat generation in adipocytes. Demonstrable single-cell thermogenesis during cold exposure allowed study of the requirement of glucose in cold-induced thermogenesis. Additionally, one of the fundamental questions in studying temperature-regulated transcription in human adipose tissue is whether cold-exposed cells in proximity to the skin surface undergoing browning release paracrine factors that induce the transcriptional program for conversion of adipocytes in deeper layers of fat which are not being directly exposed to cold. For this purpose, we developed an engineered system which generates temperature gradients and allows us to study paracrine interactions between warm and cold fat cells. Our findings suggest adipocytes exposed to cold temperature may modulate cellular responses in neighboring warm cells.

CHAPTER 1. INTRODUCTION AND BACKGROUND

Portions of this content have previously been published in Brennan, M.D., Rexius-Hall, M.L., Elgass, L.J., and Eddington, D.T. (2014) Oxygen control with microfluidics, Lab Chip. 14(22):4305-18.

1.1 Engineered Microenvironments for Controlled Hypoxia

1.1.1 Oxygenation of Cells and Tissues

Oxygen accounts for nearly 21% of the earth's atmosphere. Although inhaled air is typically a 21% oxygen (O_2) gas mixture, cells and tissues experience a partial pressure of oxygen, or oxygen tension, well below ambient atmospheric oxygen tension. Normoxia, the term for the normal physiologic level of oxygenation in the body, is cell- and tissue-specific. The most oxygenated parts of the body—the arteries, lungs, and liver—experience 10-13% oxygen [3]. In contrast, various regions of the brain and bone marrow vary from a maximum of around 7% O_2 to a minimum of 0.5%-1% O_2 [4, 5] (reported physiologic oxygen levels for different human tissues is listed in Table 1.1). In standard cell culture, physiologic oxygen tension is largely neglected as incubators maintain cells at 37°C in 5% CO_2, balanced atmospheric air. The use of ambient levels of O_2 does not reflect oxygenation *in vivo*. Despite this fact, oxygen tension is a parameter of *in vitro* engineered microenvironments that is often overlooked.

TABLE 1.1: The physiologic oxygen levels vary for different human tissues. The indicated normoxic levels are all below atmospheric (21%) oxygen. Values compiled from refs. [3–6].

Tissue	Physiologic Oxygen (%)
Lung alveoli	13
Liver	10–13
Arterial blood	10–13
Venous blood	5
Bone marrow	0.5–7
Brain	0.5–7
Cartilage	1

1.1.2 Hypoxic Signaling

Cellular function and behavior are affected by oxygen levels in the microenvironment. Oxygen levels impact a broad array of critical biological processes including angiogenesis [7, 8], embryonic development [9, 10], stem cell differentiation [11, 12], extracellular matrix remodeling [13], tumor growth and progression [14], and metastasis [15]. Cells adapt to environmental oxygen levels by shifting metabolic processes and initiating transcriptional programs. When oxygen demand exceeds the supply, the intracellular oxygen levels decrease, and cells experience hypoxia. Virtually all hypoxia-related alterations in gene expression rely on the transcriptional activity of the hypoxia-inducible factor family of transcriptional factors.

1.1.2.1 Hypoxia Inducible Factor (HIF) Family of Transcription Factors

Hypoxia-inducible factors (HIFs) are a family of transcription factors that are the central regulators of the transcription of hypoxia-responsive genes, including growth factors, receptors, and metabolic enzymes. The key α-subunits, HIF-1α and HIF-2α, are subject to rapid turnover under normal physiological oxygen (normoxic) conditions via the action of prolyl-hydroxylases (PHDs) which hydroxylate proline residues within the oxygen-dependent degradation domain (ODD) of HIFs and promote ubiquitination and proteasomal degradation [16]. Hypoxia suppresses PHD activity because PHD enzymes use oxygen as a substrate for hydroxylation, thus allowing HIF-1α and HIF-2α to accumulate and translocate to the nucleus where they bind to the ubiquitously expressed HIF-1β (also known as ARNT). The heterodimer forms a functional transcription factor that can then bind to DNA at a site in a HIF target gene known as a hypoxia response element (HRE) and initiate hypoxia-activated transcription [7, 17, 18].

1.1.2.2 Differences Between HIF-1α and HIF-2α

Although HIF-1α and HIF-2α both bind HIF-1β and initiate the transcription of hypoxia-responsive target genes, differences between the α-subunits have been determined. For example, HIF-2α has an amino acid sequence that shares only 48% homology with that of HIF-1α [19]. Additionally, while HIF-1α is present in nearly all cell types, HIF-2α is less widely expressed. HIF-2α is specifically expressed in cell types including but not limited to endothelial cells, cardiomyocytes, kidney fibroblasts, glial cells, and hepatocytes [20]. The temporal patterns of induction differ with HIF-1α mediating acute responses to hypoxic insult, accumulating rapidly and transiently, while HIF-2α seems to mediate a gradual and sustained response that persists during prolonged hypoxia [21]. Furthermore, HIF-1α and HIF-2α play nonredundant biological functions; studies suggest that HIF-1α and HIF-2α regulate different target genes [22].

1.1.2.3 Biological Assessment of HIF Activation

At the cellular level, HIF activation requires α-subunit stabilization, accumulation, and nuclear translocation. The biological assays to measure HIF activation include fluorescent imaging of the protein [23–25], immunoblotting of the protein [25–28], determining relative gene expression of downstream HIF target genes [29–32], and monitoring luminescent HIF promoter activity [26, 28, 33, 34]. Imaging and immunoblotting techniques can both be used to evaluate accumulation of HIF α-subunits wherein intensity of the protein signal increases as compared to a negative control. Imaging can be used as a method to determine nuclear translocation; nuclear dyes are used to label the nuclei and imaging can demonstrate colocalization of the protein with the site of a nucleus. Immunoblotting can also be used to determine the extent of nuclear translocation, but this requires nuclear fractionation of cell samples.

Polymerase chain reaction (PCR) can be used to indirectly show HIF activation by measuring messenger ribonucleic acid (mRNA) levels of known target genes. The mRNA

levels of HIF α-subunits are not typically thought to be important. Research of HIF regulation suggests α-subunits are subject to post-translational regulation rather than transcriptional regulation. Emerging evidence suggests that there may be biologically significant HIF α-subunit regulation at the mRNA level [21, 35, 36]. However, the pathways and their function are not fully understood.

HIF promoter reporter assays are commonly used to study HIF-regulated signal transduction. Promoter reporter constructs contain HREs which drive the expression of a frequently quantified protein such as green fluorescent protein (GFP) or luciferase. Increases in units of relative luminescent intensity compared to controls are readouts for the specific ability of HIF transcription factors to bind HREs and initiate transcriptional activity.

1.1.2.4 Chemical Induction of HIF

Standard biomedical laboratories are often not equipped with tools to modulate oxygen levels exposed to cell samples. As a result, there has been considerable interest in identifying compounds that activate HIF by mimicking the effect of a reduced-oxygen environment on the HIF signaling pathway, namely by preventing HIF α-subunit degradation. Chemical inducers of HIF are frequently PHD inhibitors because PHDs (also known as EGLN enzymes) are the molecular oxygen sensors that regulate HIF. PHDs require iron, oxygen, and 2-oxoglutarate (2-OG) to hydroxylate proline residues [16]. The compound Cobalt (II) Chloride ($CoCl_2$) and desferrioxamine (DFO) are commonly-used PHD inhibitors. Both compounds inhibit PHDs by intervening with iron availability; $CoCl_2$ replaces iron (Fe) with cobalt (Co) and DFO is an iron chelator. Dimethyloxaloglycine (DMOG) and dihydrobenzoic acid (DHB) are also widely used PHD inhibitors. These compounds are both 2-OG analogs and inhibit PHDs by acting as competitive inhibitors against 2-OG for binding to the enzyme active site.

Although hypoxia mimetics are often employed in hypoxia studies as a positive control for HIF analysis, drugs can have off-target effects and alter cellular behavior otherwise unaffected by oxygen tension. Among the compounds themselves, not all PHD inhibitors are created equal. There is evidence that different PHD inhibitors have distinct cellular effects [37, 38]. Adopting the use of tools to control oxygenation has the advantage of avoiding drugs that may or may not mimic the entire hypoxic response pattern, preserving the natural dynamics of oxygen tension-mediated events, and allowing obtained research results to truly reflect cellular oxygen-sensing mechanisms.

1.1.3 Methods to Control Homogeneous Oxygenation

The most widely used tools to create hypoxic environments to study cellular behavior have been (1) hypoxic chambers, (2) hypoxia workstations, and (3) perfusion chambers. These tools can only produce a single, homogeneous oxygen level at a time. They are also unable to replicate oxygen gradients found *in vivo* which form from radial and axial diffusion of oxygen from the microvasculature and metabolic consumption of oxygen by surrounding cells. Ultimately, the single oxygen level macroenvironments in such culture systems do not establish oxygen gradients that are physiologic.

1.1.3.1 Hypoxic Chambers

Hypoxic chambers remain as the tool of choice for imposing distinct oxygen conditions because they are small enough to be housed inside a standard incubator, do not require specialized equipment for operation, and have the added advantage of being inexpensive ($\sim$\$500) as compared to hypoxic workstations ($\sim$\$50,000). Their price has made hypoxic chambers an attractive tool for labs interested in studying cells in low oxygen tension but not necessarily specializing in hypoxia. The hypoxic chamber consists of a vessel in which to place cell culture plates and dishes that can then be purged with a gas mixture of interest, sealed, and placed in an incubator. However, hypoxic chambers are prone

to leaks, have inherently low throughput, require considerable incubator space, cannot replicate anoxic conditions even when purged with nitrogen, equilibrate slowly (on the scale of several hours), and are not compatible with microscopic analysis. Additionally, the oxygen level within a hypoxic chamber is imprecise. The oxygen concentration is not the same stable concentration as the infused gas throughout the chamber because transport limitations create a discrepancy between the gas concentration within the infused headspace and the gas concentration at the bottom of the culture dish.

1.1.3.2 Hypoxia Workstations

The hypoxia workstation is a relatively large, sealed biosafety cabinet purged with a gas of interest, monitored with oxygen sensors, and equipped with its own incubator in one corner of the cabinet. Due to its cost, the hypoxia workstation is generally only found in labs specializing in hypoxia research. A workstation is attractive because, as compared to the hypoxic chamber, it is equipped with a small, gas-modulated benchtop to perform conventional biological assays such as western blot and PCR preparations. The workspace is useful because hypoxic factors, like the HIF family of transcription factors, degrade rapidly upon re-equilibrating with atmospheric oxygen. Therefore, performing such assays in a sealed, hypoxic environment is ideal to achieve the best results. Atmospheric equilibration is a concern when using hypoxic chambers, rather than hypoxic workstations, as they must be opened to retrieve cell culture contents or even to change media, forcing equilibration with ambient surroundings and an unintended intermittent hypoxia exposure which has been found to alter cell fate and function [39, 40].

Though the workstation offers a precisely controlled, homogeneous oxygen environment and space to perform biological assays, the setup is cumbersome. Small, delicate manipulations must be done from outside the cabinet while wearing bulky, integrated rubber gloves. Additionally, like the hypoxic chamber, the workstation cannot be easily

coupled to live-cell microscopy unless a microscope is housed within the incubator. Overall, the hypoxic workstation is expensive and leaves too large of a footprint to be readily accessible to a wide population of researchers.

1.1.3.3 Perfusion Chambers

Another option is a commercially available perfusion chamber in which oxygen concentration is able to be modulated by alternating the flow of oxygenated and deoxygenated liquid that is mixed to defined ratios through the chamber. Like the hypoxic chambers and workstations, perfusion chambers lack spatial control. The effect of the added shear stress that comes along with the flow must also be considered with use of perfusion chambers. Shear stress is known to alter cell morphology and gene expression [41–43], so the consequences of non-negligible shear stress should not be underestimated.

1.1.3.4 Motivation for Microfluidic Tools

Current global methods to study cellular behavior in low levels of oxygen tension lack spatial control, equilibrate slowly, and are difficult or impossible to couple to live-cell microscopy. To fulfill these unmet needs, a variety of microfluidic devices have been developed to permit tight control of oxygen levels in cultured cells. In order to understand how the microscale can be leveraged for oxygen control of cells and tissues within microfluidic systems, some background understanding of diffusion, solubility, and transport at the microscale is necessary.

1.1.4 Diffusion, Solubility, and Transport of Oxygen in Microfluidic Devices

Because microfluidic systems are characterized by low Reynolds numbers, no turbulent flow is present to enhance mixing within a microfluidic system, and so simple diffusion adequately describes the transport of diffusive species within a microchannel. Simple—or

Fickian—diffusion is described by

$$J = -D(\frac{\partial C}{\partial x}) \tag{1.1}$$

where J is the diffusive flux, D is the coefficient of diffusion for a chemical species in a given medium, and C is the concentration of the chemical species. The relationship

$$x^2 = 2Dt \tag{1.2}$$

describes the mean-square displacement of a particle in relation to time lapsed in the system. Because time depends on the square of displacement, diffusion on the microscale takes much less time because the displacement is orders of magnitude smaller than diffusion on the macroscale. In order to illustrate the effect of scale on diffusion time, consider two observers in a room with a jar of sulfur. Observer one is positioned 10 micrometers away from the jar, while observer two is positioned one million times farther away at 10 meters from the jar. At $t = 0$, the jar is opened and at t_1 the sulfur molecules (and odor) reach observer one at 10 micrometers. At t_2 the sulfur molecules reach observer two at 10 meters. Considering only Fickian diffusion as a method of transport and making use of equation (1.2), it would take 10^{12} times longer for the molecules to reach observer two at 10 meters as it would to reach observer one at 10 micrometers. Using a realistic diffusion coefficient of 0.16 cm^2sec^{-1} for sulphur in air, observer one would smell the sulphur in 30 nanoseconds while observer two would be spared for 8 hours and 40 minutes. In reality, of course, an observer on the macroscale would be able to smell the sulfur rather quickly, but that is due to the presence of turbulent flow and thermal gradients which facilitate transport in the air. While relying on diffusion for an experiment at the macroscale would be an either costly or impossible time commitment, diffusion can be a readily leveraged mode of transport at the microscale and within microfluidic devices.

PDMS (polydimethylsiloxane) is a commonly used polymer in microfluidics due to

its many desirable qualities, including but not limited to optical clarity, biocompatibility, and its ability to be molded down to sub-micron resolution. For this discussion, though, of interest is its high permeability to gas, as it is the most permeable of the elastomeric polymers [44]. Microfluidic experiments for oxygen control frequently involve gas diffusion from a channel through a thin PDMS layer (or membrane) into another area of the device—perhaps another channel or a reservoir.

From Fick's Law, one can determine that, at steady-state and when either side of the membrane is exposed to gas, the permeability P of a polymer membrane to a gas can be described by

$$P = J\left(\frac{dx}{dp}\right) \tag{1.3}$$

where dx is the membrane thickness and dp is the difference in pressure experienced by the two sides of the membrane. From this equation, it is simple to see that diffusive flux through a membrane will increase with greater pressure difference across the membrane and with decreased membrane thickness.

When considering a typical diffusion membrane in a device as an example, one side of the membrane has gas flowing from a pressurize tank and the other side has ambient air, the diffusive flux experienced by either side is dependent on the net flux of a diffusive species into or out of the membrane. It is important to note that this is really a dynamic process as the gas entering or exiting the membrane can be offset somewhat by sorption to or desorption from the membrane of the same chemical species. At equilibrium, this should result in a constant net flux into and out of the membrane, and the flux through any single step (gas channel to membrane, through the membrane, and membrane to reservoir) is considered the same as the flux through the membrane, and may be defined as

$$J = k_1 \frac{D}{D(k_1 + k_2) + k_1 k_2 dx}(c_1 - c_2) \tag{1.4}$$

where D is the diffusivity of the gas through the membrane, k_1 and k_2 are the desorption

rate constants at each interface of the membrane, and c_1 and c_2 describe the concentrations of the gas in the polymer, according to

$$c = pS \tag{1.5}$$

where p is the gas pressure on either side of the membrane and S is the solubility of the gas in the polymer. However, when one side of a membrane is exposed to a liquid, this relationship is no longer accurate because gas flux, J, is reduced, and the desorption rate constant of the side of the membrane exposed to liquid, k_2, is different than the rate constant of the side of the membrane exposed to gas, and can now be described by

$$k_2 = \frac{Dk_1}{D + k_1 \triangle x + \rho_w k_1 D} \tag{1.6}$$

where ρ_w is the wet mass transfer resistance.

In addition to changes in the behavior of sorption and desorption from polymeric membranes depending on the surrounding medium, it is also important to note the differences in the way gas—specifically oxygen for the purposes of this paper—behaves in PDMS versus water. For an excellent in depth analysis, Kim *et al.* present a mathematical analysis of oxygen transport in microfluidic systems [45]. Under identical conditions, oxygen gas is 1.7 times more diffusive in PDMS than in water, and six times more soluble in PDMS than in water [46].

Oxygen control is permitted by diffusion of compressed gases across a 100 μm thin polydimethylsiloxane (PDMS) membrane. With such a thin membrane, the time to achieve equilibrium of gas conditions is on the scale of 20 seconds. The partial differential equations of Fick's second law of diffusion can be solved with specific initial and boundary conditions to plot the period of non-steady state diffusion of gas into the PDMS. The result is the oxygen partial pressure as a function of spatial position and time. The case of

gas A diffusing into a solid B can be solved as:

$$\frac{C_s - C_x}{C_s - C_o} = erf\left(\frac{x}{2\sqrt{Dt}}\right) \tag{1.7}$$

with the assumption that the solute is semi-infinite. C_s is the surface concentration of the element in gas diffusing into the solid. C_o is the initial uniform concentration of the element in the solid. C_x is the concentration at a position x, where the variable x is the distance from the surface of the solid. D is the diffusivity of the diffusing solute element, and t is the time. The erf function is the mathematical error function which is defined as:

$$erf(y) = \frac{2}{\sqrt{\pi}} \int_0^y e^{-t^2} dt \tag{1.8}$$

1.1.5 Measurement of Oxygen

Measuring the oxygen concentration in the microenvironment or within cell cultures presents specific challenges. Samples are not large enough for the Winkler method [47], in which dissolved oxygen (DO) is fixed and measured with stoichiometric methods. Many times, experiments require real-time measurement as well as high spatial resolution of oxygen tension. Several tools have been adapted for measuring oxygen tension in the microenvironment, including employing either Clark-style electrodes or luminescent optical sensors.

1.1.5.1 Clark-style electrodes

Clark-style electrodes [48] typically use a platinum working electrode and silver chloride reference electrode with potassium chloride for the electrolyte. A voltage of about 800 mV, which is sufficient to reduce oxygen, is applied across the electrodes. Oxygen is reduced at the working electrode, thus producing electrons or current proportional to the

amount of oxygen present. The electrodes and electrolyte are protected behind a gas-permeable layer of polytetrafluoroethylene (PTFE) to prevent adsorption of proteins or interfering ions from fouling the electrodes. Because Clark-style electrodes consume oxygen in order to detect it, stirring of the sample is usually required for fast response measurements. The electrode is also very sensitive to changes in sample temperature. Clark electrodes are unreliable for long-term measurements for a number of reasons which contribute to unstable readings: depletion of the electrolyte, the production of OH^- ions affecting the pH causing zero drift, and the anode becoming coated in AgCl. If used with biological samples, the protective, PTFE membrane will also lose permeability over time due to the adsorption of protein and other residues. Clark-style electrodes also suffer from low temporal and spatial resolution due to the time it takes for oxygen to diffuse across the PTFE membrane and to the electrodes. In addition, the relative size of these probes ($\sim$3+ mm diameter probe) makes interfacing with microfluidic channels problematic.

1.1.5.2 Luminescent optical sensors

For microfluidic systems, optical oxygen sensors are the tool of choice. They have several advantages over Clark-style electrodes. They do not consume oxygen so they can be used in low or no flow environments and do not suffer from fouling, making them stable for long-term studies. Where Clark electrodes require an electrical connection to each position to be measured and only provide a single, low spatial resolution measurement, optical sensors allow measurement over the entire area of the sensor and at any number of discrete points.

These sensors take advantage of oxygen-indicating fluorophores (e.g. ruthenium or platinum-based compounds) that are quenched in the presence of oxygen. The degree of quenching is determined by the oxygen partial pressure. The relationship between

intensity and oxygen partial pressure is described by the Stern-Volmer equation:

$$\frac{\tau_0}{\tau} = \frac{I_0}{I} = 1 + K_q \tau_0 [\mathrm{O_2}] \tag{1.9}$$

where I_0 and τ_0 are the intensity and excited state lifetime in the absence of oxygen, τ is the excited state lifetime in the presence of oxygen, $[\mathrm{O_2}]$ is oxygen concentration, and K_q is the quenching constant. A Stern-Volmer calibration curve must be made for each sensor and application. When a sensor is calibrated, a corresponding Stern-Volmer curve is created by measuring the intensity at no fewer than two known oxygen partial pressures. The intensity data collected is fitted to the Stern-Volmer equation to elicit the corresponding oxygen partial pressure. Typically, a basic fluorescent microscopy setup is sufficient to monitor a fluorescent sensor-equipped device, although custom excitation/detector modules can also be created for portability, miniaturization, or placement in an incubator [49]. Fluorophores are sensitive to photobleaching, where the intensity becomes attenuated after long term constant excitation, but short periodic exposures are typically used to avoid photobleaching. In addition to simple intensity-based measurements, fluorescence lifetime imaging microscopy (FLIM) uses a modulated excitation source and detects the decay in intensity in either the time or frequency domain. This method can be used to reduce background luminescent artifacts, sensitivity to ambient light sources, and variations in intensity due to the concentration of the dye [50].

1.1.6 Oxygen Control with Microfluidic Devices

In order to overcome the inherent limitations of current oxygen modulation methods, microfluidic platforms have been developed to take advantage of rapid diffusion and advances in oxygen measurement technologies. Microfluidic oxygen control has been applied to different biological systems, and serves purposes outside of solely controlling oxygen concentration. Some of these applications include improving the quality of an experiment, creating a more physiologically realistic environment in which to grow cells,

and studying the mechanisms of different diseases. Several variations of microfluidic platforms have been used to generate the desired oxygen environment for these experiments, including devices that rely on diffusion from fluid, utilizing on-or-off-chip mixers and equilibration steps, leveraging cellular oxygen uptake to deplete the oxygen, and using chemical, electrolytic or photocatalytic reactions to produce oxygen directly on chip. Microfluidics platforms have been used to control the oxygen microenvironment and to measure the effect of oxygen concentration on biological materials in a variety of ways, including exposing biological specimens to various constant concentrations of oxygen, discrete regions of different oxygen concentrations, and oxygen gradients. Microfluidic systems for controlling oxygen at the microscale have been applied to address a variety of physiologically relevant questions, for examining the behavior of cells in different and tightly-controlled oxygen environments, and they have been applied to studying specific pathologies including cancer, strokes, and sickle cell disease.

1.1.6.1 Diffusion from a Source Fluid

Perhaps the most popular and straightforward method for oxygen control in microdevices is by diffusion from a source or control channel across a thin, gas-permeable PDMS membrane and into the cell culture region. The source fluid in the control channel rapidly diffuses to control the dissolved gas environment experienced by the cells.

Equilibrated Liquid. Exposing cells and tissues to different oxygen levels can be accomplished by flowing a pre-equilibrated liquid through the device's control channels. In many cases, media is equilibrated with the appropriate gas before introducing it to cultures. For instance, a commonly used method to mimic the induction of hypoxia is to place cell cultures in medium that has been bubbled with nitrogen [51]. The equilibration of media with nitrogen is frequently done in addition to housing the cultures in a hypoxic chamber or gas-controlled incubator [52] to reach even lower levels of oxygen.

In microfluidic systems, cell culture media is also frequently equilibrated with appropriate gas mixtures to control oxygen content. In these systems, constant perfusion of the equilibrated media is usually necessary to maintain the desired oxygen level. Without an ideal, closed system, the oxygen concentration of media will re-equilibrate with ambient surroundings (i.e. the atmosphere) over time.

One example is the work by Grist *et al.* where diffusion from liquids was used to establish oxygen gradients across a central channel. To create the on-chip oxygen gradient, off-chip gas bubbling flasks produced deoxygenated and oxygenated water which was fed via oxygen-impermeable tubing into designated control water channels (Fig. 1.1). A deoxygenated control water channel flanked one side of a media perfusion chamber containing cells while an oxygenated water channel flanked the other side. Only a thin, PDMS membrane of $\sim$100 μm separated the control water channels from the cell chamber. The high gas permeability of PDMS and the difference in the oxygen level in the control water channels allowed for the spatial gradient generation in the cell chamber. The perfusion rate of the oxygenated or deoxygenated water (100 μL/min) was maintained by syringe pumps which withdrew media, creating negative pressure to pull the liquid through the device. The media perfusion rate in the cell chamber was purposely maintained at a value several magnitudes lower (0.3 μL/min) than the control water channels to permit the formation of a stable oxygen gradient in the cell chamber.

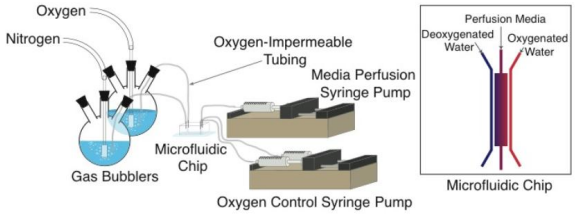

FIGURE 1.1: An off-chip bubbling experimental setup demonstrates generation of an oxygen gradient using equilibrated liquid. Reproduced from ref. [53].

Integrated platinum (II) octaethylporphyrinketone (PtOEPK) sensors monitored the

oxygen gradient and simulation modeling was undertaken to predict the oxygen gradient profile. However, the model did not fit the acquired data. Namely, the range of oxygen concentrations created experimentally was not as large as that predicted in the simulation. It is suggested that this discrepancy was due to the gas-permeable nature of PDMS and the rapid re-equilibration of the device's channels with the ambient partial pressure of oxygen. The researchers expect that coating the outside of the PDMS block with an oxygen-impermeable coating (e.g. with Parylene) could improve oxygen control [53].

Gas Perfusion. Flowing gas directly though the control channels eliminates the need for the pre-equilibration of liquid off-chip. Gas also has the advantage of having a lower viscosity than water allowing for more rapid mixing. Additionally, flow is driven with large pressurized sources (gas tank) eliminating the need for syringe pumps. The convenience and simplicity of gas perfusion makes it an easy choice for researchers wishing to accomplish more complicated experimental schemes discussed in detail below. The following devices demonstrate oxygen control in a variety of ways, including discrete control (obtaining multiple, uniform oxygen concentrations), spatial control (binary oxygen concentrations, and spatial gradients of oxygen concentrations), and temporal control (switching between oxygen concentrations at set time intervals or maintaining a constant oxygen concentration over time).

Leclerc *et al.* present an early demonstration of oxygen modulation in a microfluidic device. The system is a bioreactor composed of four microfluidic cell culturing regions stacked one on top of the other, with a media perfusion channel providing flow to the cell culture chamber. Inserted into the middle of the bioreactor (flanked above and below by two cell culturing regions) is what the authors call an "oxygen chamber," which is connected via channels to the environment outside of the bioreactor [Fig. 1.2]. This served as a way to allow gas from the outside environment to easily modulate the oxygen conditions within the culturing chamber. After culturing, this oxygen chamber design resulted

in a 5-fold increase in cell growth compared to a 2-layer bioreactor and 8-fold increase compared to a 4-layer bioreactor without the oxygen chamber. Additionally, albumin production was monitored from cultured hepatocytes and only the cells grown in the 4-layer bioreactor with the oxygen chamber showed increased albumin production over a 12-day experiment [54]. Although the oxygen modulation is completely passive in this device, it represents a conceptual prototype for the more intricate control devices to follow.

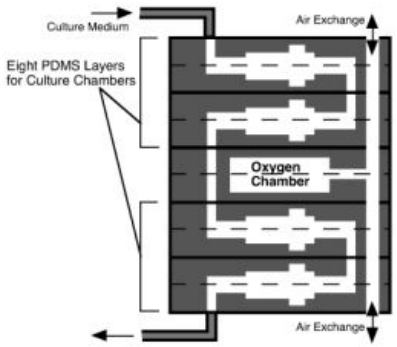

FIGURE 1.2: An early microfluidic bioreactor demonstrates enhanced oxygen modulation. Reproduced with permission from ref. [54].

1.1.6.2 Discrete Series of Constant Oxygen Concentrations

A number of devices exist for exercising discrete control of oxygen levels in a microfluidic platform. These devices may be designed such that one device contains several isolated regions of discrete oxygen concentrations, or such that they maintain constant oxygen concentrations over a period of time. Vollmer *et al.* presented a system for dynamic delivery and sensing of oxygen in perusing medium when oxygen is delivered via a gas channel. PtOEPK oxygen sensors are placed in etched wells of a glass slide at the inlets and outlets of a microfluidic network to monitor oxygen levels. A custom excitation/collection module was created to house the device and monitor oxygen levels from the sensors. Again, oxygen diffuses from a gas channel across a PDMS membrane and

into liquid channels. While this system is not applied to biological studies, it is an early example of the use of *in situ* PtOEPK sensors for oxygen characterization, and is a major advance in the development of microfluidic platforms for oxygen control of the microenvironment [55].

Polinkovsky *et al.* present two devices in which individual growth chambers within two microfluidic devices take on discrete values ranging linearly between 0 and 100% oxygen concentration over nine chambers in one device, and exponentially from 0 to 21% oxygen concentration over nine channels in the second device. (Fig. 1.3) In these experiments, Ruthenium dye was used to characterize the oxygen levels. For each device, the oxygen concentrations in the gas channels are achieved by flowing two gases through a three-step, on-chip mixing channel network, culminating in nine separate channels of discrete concentration that flow over the growth chambers, which contain media. The growth chambers can be used to culture yeast, bacteria, or mammalian cells. For the purposes of their experiment, *E. coli* division rates as a function of oxygen concentration were determined [56]. This device is a step forward in oxygen control systems because it presents a means to use one device to deliver many different oxygen concentrations. Combining this ability with multiple growth chambers means that high-throughput, oxygen-controlled experiments can be conducted.

Lam *et al.* present a microfluidic platform for culturing aerobic and anaerobic bacteria and mammalian cells. An on-chip mixer creates a series of discrete oxygen concentrations by mixing oxygen and nitrogen that range linearly from 0 to 42%, and cells were cultured in channels at these oxygen concentrations. Incorporated into the device is a valve multiplexer, which was used to replace media in each of the eight wells at regular intervals. A custom excitation module was designed using LEDs as the excitation source and paired with a custom infrared detection module. PtOEPK polystyrene sensors were embedded in wet-etched wells of a glass slide. The sensors were calibrated using water with different concentrations of oxygenated water and correlated with the Stern-Volmer

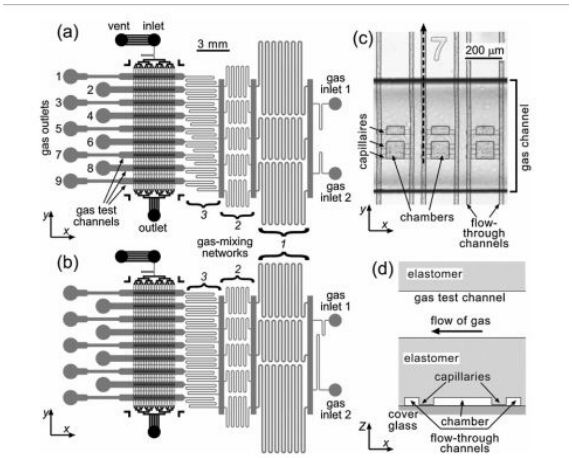

FIGURE 1.3: Two devices for generating discrete series of gas concentrations in chambers for various cultures. In the drawing of the two devices in (A) and (B) the gray serpentine mixing channels determine the dissolved gas environment of the culture region (black vertical channels). The individual lengths of the serpentine channels vary in the two devices to determine the degree of mixing from the two gas inlets. Reproduced from ref. [46]

analysis. Cell density and growth rates were studied with *E. Coli*, *A. Viscosus*, *F. Nucleatum*, and embryonic fibroblast cells [49]. This device couples oxygen and valve control, and demonstrates that techniques necessary for cell culture (media replacement, in this case) can be incorporated into these experiments.

1.1.6.3 Constant Oxygen Concentration

In addition to microfluidic culture chambers of custom microfluidic devices, Oppegard *et al.* developed a microfluidic insert for a standard 6-well plate, which can be used to modulate oxygen concentration in cell culture in lieu of a hypoxic chamber, and with better oxygen control than a hypoxic chamber. The device's oxygen concentration is characterized using a ruthenium coated substrate, and was further validated by monitoring HIF-1α expression in cells, to ensure that it agreed with expression levels from traditional methods. The device is an insert which nests into standard six-well plate leaving a designated gap from the bottom of the plate. Gas is constantly perfused across the gas permeable membrane (PDMS) where it diffuses to oxygenate or deoxygenate the multiwell

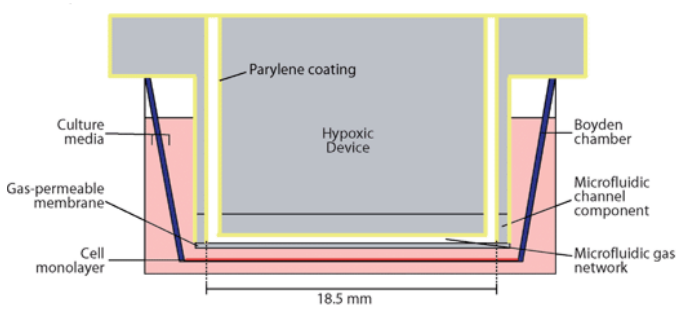

FIGURE 1.4: Oppegard *et al.* microfluidic insert for 6-well plate with Boyden chamber. Reproduced from ref. [58].

plate at the culture surface. The oxygen concentration within the device rapidly changes when the input gas is changed, and can maintain a steady oxygen concentration over five days [57]. The main innovation of this work was adapting microfluidic oxygen control to the 6-well plate which is a standard workhorse of biomedical research. In a follow up paper they expanded on this theme to develop an insert for Boyden chambers which also nest into a multiwell plate for cell migration studies (Fig. 1.4). The ability to maintain an oxygen concentration in addition to the ability to quickly adjust to a new oxygen concentration when a new gas is flowed through the device makes this system very useful for both constant oxygen concentration studies and intermittent hypoxia studies. Hypoxia studies were conducted using an invasive breast cancer cell line and it was found that intermittent hypoxia resulted in different migration than constant hypoxia [58].

Abaci *et al.* present a microbioreactor for consistent, long-term oxygen control of the microenvironment with live computer monitoring of oxygen concentration in the device. The format of the device is a top gas channel which is used to diffuse oxygen into a lower, closed culture channel via a PDMS membrane. Both channels are etched into polymethylmethacrylate (PMMA). Fluorescent sensors were used to monitor the device's dissolved oxygen level. The system is composed of sensor patches (flat 3 mm discs), fiber-optic guides, and a 4-channel transmitter device which interfaces with a computer. Figure 1.5 shows a schematic of the device. Media was constantly perfused at a relatively slow flow

rate of 0.02 ml/h. The temporal responses of the oxygen tension in the channel in static conditions in which the gas channel was supplied with discrete oxygen levels (21%, 5%, and 1%) was compared to dynamic conditions which utilized the same discrete oxygen levels in the gas channel but also media perfusion in the culture channel at 0.5 ml/h were compared, and resulted in similar oxygen profiles. The shear stress introduced by perfusion was negligible compared to shear stress levels reported to affect cell behavior. To demonstrate the bioreactor's abilities, fibrosarcoma cells were cultured and cell viability, cell density and circularity tests were performed at 1% and 21% dissolved oxygen concentrations [59].

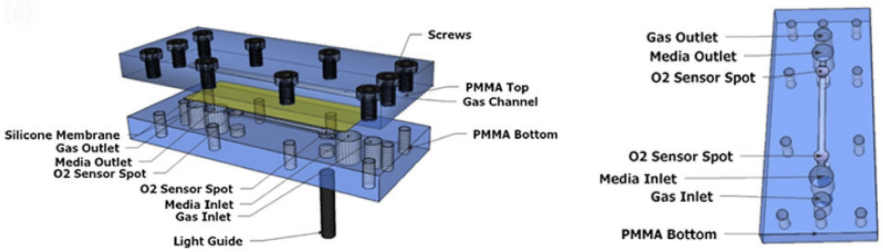

FIGURE 1.5: Microbioreactor with *in situ* oxygen sensors for live computer oxygen monitoring. Reproduced with permission from ref. [59].

Another example of a microfluidic device used to study the behavior of cancer cells in hypoxic and normoxic environments is presented by Funamoto *et al.*, who designed a PDMS microfluidic device with an integrated 3D gel for cell culture flanked by media channels. Each media channel was separated from a gas channel by a 150 μm diffusion gap. Oxygen diffusion between the incubator environment and the PDMS device was inhibited by a polycarbonate (PC) film bonded above the channels. The device was validated using a ruthenium-coated glass cover slip as an oxygen sensor. The device's utility was demonstrated by studying the migration of human breast cancer cells (MDA-MB-231) in hypoxia. Time-lapse live-cell 3D confocal imaging was acquired to determine the cancer cell migration within the gel extracellular matrix (ECM). Cells in the

gel showed increased net displacement, total path length, and their ratio (persistence) increased under hypoxia as compared to normoxia. Despite demonstrating that the device design lends itself to establish a gradient across the gel, cells were not studied in a gradient. Increased migration corresponds with increased invasive behavior of breast cancer cells reported in other studies [60].

In another example, oxygen was used to control the polymerization of sickle-cell hemoglobin (HbS) blood as a model of a vaso-occlusive crisis in sickle cell disease. Again, gas diffuses from a gas channel, across a PDMS membrane, and into the blood perfusion network. Occlusive and relaxation events due to HbS polymerization and depolymerization, respectively, are measured as a function of oxygen concentration by monitoring blood flow velocity in their microfluidic device. The device is presented as a tool to study sickle cell disease and possible future clinically useful agents to block HbS polymerization. CO binding is used to demonstrate that HbS polymerization can be blocked even in cases of extreme deoxygenation [61]. This device represents the first model of the dynamic sickling process without influences of endothelial cells and a follow-up study will be discussed in a later section.

Lo *et al.* demonstrate a diffusion-from-gas device for a wound healing study in mice. The device was designed for a live active mouse to wear the device as a topical oxygen therapy method. 100% oxygen was delivered to the device where it diffused across a 100 μm PDMS membrane placed in conformal contact with the wound. The study demonstrated improved collagen maturity in treated mice, although the oxygen therapy did not improve wound closure rates, or microvasculature development [62].

1.1.6.4 Hydration Layer

A common disadvantage of controlling gas in microfluidic cell culture systems is evaporation of culture media which is accelerated by the flow of dry gas past the diffusion

membrane. Using equilibrated liquids to modulate gas concentrations prevents dehydration but may be slow and cumbersome if multi-condition or rapid changes in oxygen levels are required. Pre-humidification of gas, by off-chip bubbling, reduces but does not prevent dehydration [63]. A hydration layer is an additional liquid filled channel between the gas layer and culture layer through which the delivered gas must diffuse before it reaches the culture layer. In this way, the gas is humidified directly on-chip as it diffuses to the culture area preventing dehydration.

Wood *et al.* demonstrate the utility of a PBS layer in preventing dehydration of blood while allowing the transport of oxygen in a microfluidic device designed to assess vaso-occlusive risk in sickle cell disease [64]. In cross section, the design consists of a gas channel stacked on top of a PBS channel on top of the blood sample channel (Fig. 1.6). Oxygen concentration in the gas channel of the chip was modulated with solenoid valves from N_2 and air sources, and oxygen levels were monitored with a fiber optic O_2 sensor at the outlet of the gas channel. Deoxygenation of blood from sickle cell patients resulted in a reduction of flow velocity and blood conductance under the same pressure drop across the device. The reduction of flow velocity is due to the sickle shape adopted by the red blood cells (RBCs) as they became deoxygenated. The molecular basis for the shape change is a variant hemoglobin molecule, HbS, which is the result of a mutation in the gene coding the β-globin protein. Deoxygenation of these RBCs causes HbS to polymerize into long chains which stiffens the cell and leads to the shape change. The morphological change then causes changes in flow by increasing the apparent viscosity of blood, resulting in differences in the rates of change in blood conductance (defined as the velocity per unit pressure drop). The rate of change in blood conductance was leveraged to measure disease severity.

Cui *et al.* demonstrated what they refer to as a "water jacket" in a device for long-term studies of bacterial cell growth behaviors. An additional layer is added to a diffusion-from-gas device that serves as a hydration layer. This work also features modeling of

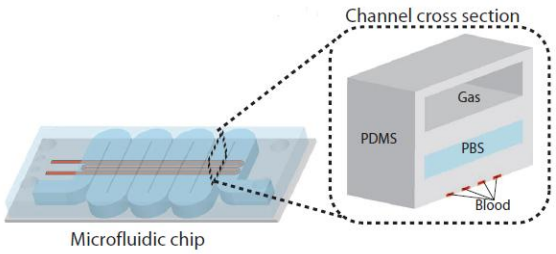

FIGURE 1.6: A hydration layer of PBS between the gas layer and blood layer prevents dehydration of the blood sample. Reproduced with permission from ref. [64].

humidity within the device due to the hydration layer as well as comparison of dehydration rates in the culture chamber, while using dry gas, humidified gas with an off-chip bubbling method, and their hydration layer with and without humidified gas [63].

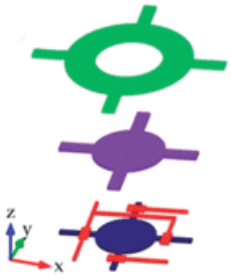

FIGURE 1.7: A hydration layer is incorporated into this device to prevent dehydration of bacterial cell culture chambers. The green layer is gas, the purple is the hydration layer, and the blue is the culture chamber. Reproduced from ref. [63].

1.1.6.5 Binary Oxygen Environment

For some experiments, a binary oxygen concentration profile is useful to elicit a biological response as a result of exposure to two distinct oxygen regions. In the previously mentioned paper, Oppegard *et al.* show that an oxygen profile of a dual-condition microchannel can maintain a stable binary oxygen profile over fourteen days. Additionally, the author presents an interdigitated microfluidic channel network that generates a cyclic oxygen profile [57]. Mauleon *et al.* modified an existing brain slice chamber with a PDMS

membrane and microfluidic channel layer. This device allows different areas of a 350 μm thick brain slice to be exposed to different oxygen concentrations independently. Oxygen levels and calcium-sensitive dyes were used to validate delivery of oxygen to discrete regions of brain slice anatomy [65, 66].

1.1.7 Oxygen Gradients

1.1.7.1 *In Vivo* Oxygen Gradients

Oxygen supply to cells and tissues is not homogeneous; oxygenation is characterized by oxygen gradients *in vivo*. These oxygen gradients occur naturally due to transport limitations of oxygen and the metabolic consumption of oxygen by surrounding cells. Within tissue, different cells are exposed to distinct oxygen levels because the oxygen supply to a given cell is limited by the diffusion distance of the cell from microvessels [67].

Much of the oxygen exchange that occurs is across capillary walls. However, studies have also found precapillary oxygen losses [68], and it is now recognized that a longitudinal gradient of oxygen is found in the arteriolar network [68–70]. The difference in the partial pressure of oxygen across the vascular wall drives oxygen out of the blood and into the tissue. The pO_2 progressively falls along an arteriole in concert with hemoglobin saturation [71]. The pO_2 of blood along a capillary also declines, and the longitudinal oxygen profile along a capillary is nonlinear due to the sigmoidal shape of the hemoglobin oxygen dissociation curve. A longitudinal capillary oxygen gradient has been confirmed by direct Phosphorescence Quenching Microscopy (PQM) [72]. Radial oxygen gradients also exist as oxygen diffuses in the radial direction from blood in the capillary into the tissue. Overall, homogeneous oxygenation models do not reflect *in vivo* oxygen gradients that occur both radially and longitudinally in the microvasculature. Tissue oxygenation decreases rapidly with increased distance from a microvessel.

1.1.7.2 Generation of Microfluidic Oxygen Gradients

To better model oxygenation found in the physiologicial setting, diffusion of gas in microfluidic devices has been used to control oxygen at the microscale and generate gradients of oxygen concentration within a device. As a continuation of the work previously described by Polinkovsky *et al.*, Adler *et al.* modified this device by controlling input to nine gas channels with computer-actuated, three-way solenoid valves, which produce different mixtures to feed into the channels. Additionally, channel wall thicknesses were decreased so different gas concentrations generate a gradient rather than discrete oxygen concentrations. Here, as well, ruthenium dye was used to characterize the oxygen gradient. The authors proposed that this device be used to study the responses of unicellular organisms to chemotactic gradients, and noted that the device design would allow a user to modify the gradient intensity of specific regions of interest within the device [73].

Most microfluidic oxygen control devices are limited to oxygen control within microfluidic channels, but a demonstration by Lo *et al.* presented gas channels buried within a gas permeable substrate of a larger open well for two different microfluidic networks. One design relied on the diffusion between parallel flow gas channels, and the second design operated via direct mixing of gas in network channels. The oxygen profile generated via the parallel channel device was more linear compared to the mixing network device, from which the profile was strongly sigmoidal (Fig. 1.8). The devices were characterized using a ruthenium substrate placed directly against the PDMS diffusion membrane. This device was used to determine the reactive oxygen species (ROS) response of cells exposed to 0-100% oxygen gradients. The results indicated that the ROS response is modulated by oxygen microgradient profiles as expected in hypoxia and hyperoxia [74].

Consumption of oxygen by cells can also be combined with constant flow of fresh media to modulate oxygen tension in the microenvironment. In order to study liver zonation Allen *et al.* cultured hepatocytes in a flat plate bioreactor with a 100 μm by 28 mm by 55 mm channel through which media was flowed (Fig. 1.9). The reactor was designed so

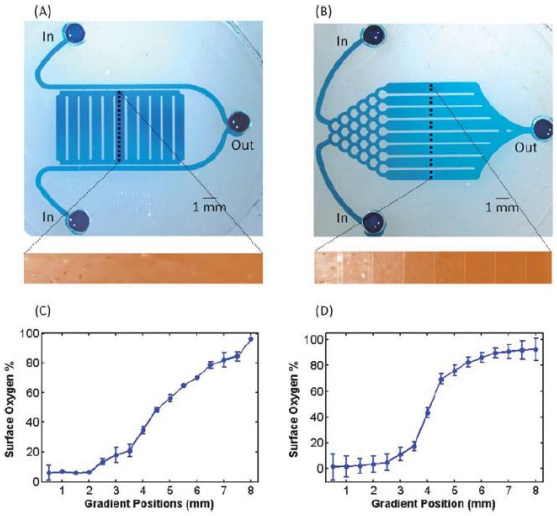

FIGURE 1.8: Lo *et al.* devices with associated oxygen concentrations. The inlets were supplied with a 100% and 0% oxygen source. Oxygen measurements demonstrated the gradient profiles generated from each mixing design. Reproduced from ref. [74].

that cells upstream consumed oxygen leaving less for downstream cells. In this sense, cell media was progressively depleted of oxygen as it flowed through the device. By controlling the oxygen level of media entering the channel and the flow of media through the reactor, a steady-state oxygen gradient was formed along the length of cell culture. The gradient could also be shifted along the length of the channel by changing the inlet oxygen partial pressure, and could be made steeper by decreasing the flow rate. This study was performed prior to the development of optical luminescent probes and verification of the gradient was performed with a hypoxia cell assay dye. Also, corresponding inlet and outlet pO_2 levels were shown to correlate strongly with model predictions. In addition to validating oxygen levels, they found biological evidence of zonation by the heterogeneous distribution of proteins phosphoenolpyruvate carboxykinase (PEPCK) and cytochrome P450 2B (CYP2B) along the length of the bioreactor, correlating with what is known to occur in physiological oxygen gradients *in vivo* [75, 76].

Oxygen can also be modulated by on-chip reactions that either generate or consume oxygen. The advantage of this method is that it eliminates the need for pressurized gas

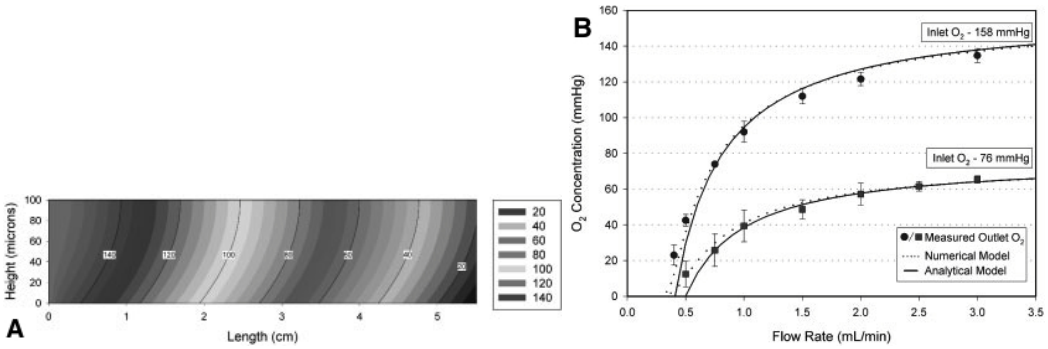

FIGURE 1.9: Modeling of the oxygen gradient in a flat-plate bioreactor with dimensions of 28 mm x 55 mm and 100 μm in height. Computational models were created to produce a gradient depending on consumption of oxygen by a cell culture with media of different initial pO_2 levels and flow rates. An example gradient predicted by the model with inlet pO_2 of 158 mmHg and a media flow rate of .035 mL/min demonstrates a linear gradient across the bioreactor as media flow from left to right (A). Measured experimental inlet and outlet pO_2 levels were compared to numerical and analytical model predictions for verification (B). Reproduced with permission from ref. [75].

tanks, although it typically requires syringe pumps to deliver the reagents. It also requires the careful modeling and balancing of reaction kinetics to achieve desired dissolved gas partial pressures.

Skolimowski *et al.* were the first to use an oxygen scavenger to create a gradient in a microfluidic cell culture device. A biofilm of *P. aeruginosa* was cultured on a thin PDMS membrane below which a serpentine channel carried the scavenger (10% sodium sulfite with 0.1 mM $CoSO_4$ as a catalyst) which irreversibly consumed oxygen from the culture above. A glass slide with a PtOEPK sensor formed the top of the culture chamber and was used to characterize the effect of media flow on the gradient and to monitor oxygen levels of the culture. A media flow rate was chosen to apply a gradient that reduced oxygen saturation at the end of the device by 60% from ambient. Attachment of *P. aeruginosa* was shown to gradually decrease along the length of the decreasing oxygen gradient (Fig. 1.10) [77].

Chen *et al.* took this idea one step further by developing a device that generated and scavenged oxygen on chip using a pair of chemical reactions. The device consisted of a

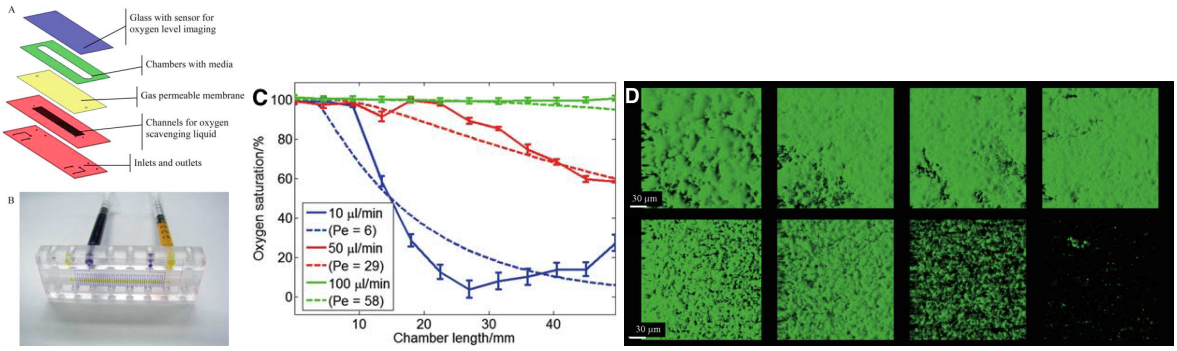

FIGURE 1.10: (A) Schematic of an oxygen scavenging device showing the serpentine channel scavenging layer (red), separated by a thin PDMS layer (yellow) from the culture chamber (green) and the oxygen sensor lid (purple). (B) Image of the device with the serpentine scavenging channel (blue) and culture chamber (yellow). (C) A comparison of simulated oxygen gradients along the chamber (dotted lines) with measured oxygen levels (solid lines) under three different flow rates. (D) Images of stained bacteria in the device at different positions along the gradient. A culture at atmospheric conditions (above) is compared to a culture with a gradient applied resulting in oxygen saturations of 97%, 79%, 60%, and 41% from atmospheric (from left to right). Reproduced from ref. [77].

central cell culture channel that is flanked on either side with a chemical reaction channel. An oxygen gradient was formed across the central channel by an oxygen-generating reaction, H_2O_2 + NaOCl, and an oxygen-scavenging reaction, pyrogallol + NaOH. Each chemical species entered the chip through a dedicated channel, and both respective reactions were initiated on chip by a serpentine mixer just before meeting the cell culture channel (Fig. 1.11). With proper throttling of flow in each channel, a steady, linear gradient could be formed across the cell culture and was characterized with a liquid ruthenium-based dye. Carcinomic human alveolar basal epithelial cells were cultured in the device under oxygen gradient and with or without Tirapazamine (TPZ), an anti-cancer drug that is activated to a toxic radical at low oxygen levels, to verify the oxygen sensitive effects on cancer cells [78].

Wang *et al.* demonstrate the formation of an oxygen gradient within a channel by matching the flow of a scavenger with diffusion of oxygen from the surrounding PDMS. With the scavenger flowing through the channel as oxygen diffuses from the PDMS bulk

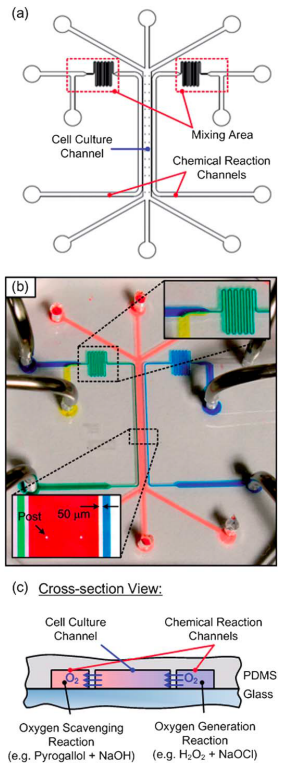

FIGURE 1.11: (A) Schematic of a device that initiates oxygen-generating and oxygen-scavenging reactions with on-chip mixers, resulting in an oxygen gradient across a central cell culture channel. (B) Image of the device with the central cell culture channel (red) flanked by the chemical reaction channels (green and blue). (C) a cross-sectional view of the device shows the path of oxygen diffusion from the H_2O_2 + NaOCl channel across the culture channel to the Pyrogallol + NaOH channel where it is consumed. Reproduced from ref. [78].

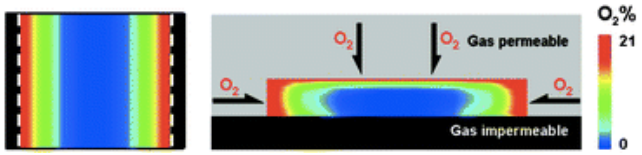

FIGURE 1.12: An oxygen scavenger flowing in a channel creates an oxygen gradient. Oxygen is depleted most in the center of the channel and against the gas impermeable wall and is replenished from the surrounding PDMS bulk. Reproduced from ref. [79].

the result is greater depletion in the center of the channel and ambient conditions near the PDMS walls. The fourth wall of the channel is a glass slide which, because it is gas impermeable, does not contribute oxygen creating a near-zero oxygen level for the culture surface (Fig. 1.12). Because the scavenger used is non-toxic (sodium sulfite), cultures of two cancer cell lines were grown directly in the channel and treated with oxygen sensitive TPZ as bio-verification of the gradient [79].

1.2 Engineered Systems for Controlled Thermogenesis

1.2.1 Temperature in Biological Systems

Temperature is a key parameter affecting biological processes. Many biological processes are temperature-dependent, including cytoskeletal dynamics [80–83], cell division [84–87], enzyme kinetics [88–92], calcium signaling [93–95], and activation of ion channels [96–101].

1.2.2 Methods to Control Temperature

To control temperature as a parameter of biological studies, the microscope incubation box and temperature-controlled stage inserts are the most common tools used during cellular imaging studies. The precision is often $0.1°$C resolution, but at the scale of these

instruments, temperature changes of several degrees take tens of minutes to several minutes to achieve, respectively. The macroscopic methods are also prone to heterogeneous temperature fields, with temperature gradients of $2°C$ - $3°C$ arising [102].

In the past, quick temperature changes have been achieved with microperfusion of different temperature-controlled solutions. However, microperfusion introduces shear stress to adherent cells. Shear stress has been shown to have biological effects such as alterations in cell morphology and gene expression [41–43]. This is a non-negligible consequence of employing perfusion systems, especially to achieve rapid temperature changes for experimental studies.

1.2.2.1 Microenvironmental Temperature

Rapid diffusive heat and mass transfer at the microscale allows for fast temperature control. Microscale characteristic times are on the scale of 10^{-3} s - 1 s as compared to 10^{2} s - 10^{4} s at the macroscale [102]. This fact has been leveraged in a host of microengineered systems to control temperature.

1.2.3 Engineered Temperature Control Platforms

Some microfluidic tools have integrated temperature control. Several groups have used laminar flow in a microfluidic channel to generate different temperature conditions. The laminar flow available at the microscale can be leveraged to create a temperature gradient because there is only local diffusive heat transfer at the interface of the flow streams. In the work of Luccheta *et al.*, laminar flow was used to create a temperature step gradient from $17°C$ - $27°C$ to which drosophila embryos were exposed [103]. Results showed that a temperature step between the anterior and posterior halves of the embryo caused development at different rates. Pearce *et al.* cultured neurons in a dual condition temperature gradient where one microchannel was kept warmer than a second microchannel and the two streams met at a Y-junction and continued laminar flow downstream. A steep spatial

gradient generated by laminar flow was demonstrated using temperature measurements in the channel using an aquarium thermometer and COMSOL simulation [104].

Another method to control temperature has been the creation of bilayer devices in which the upper layer was used as a temperature control layer through which to flow temperature-controlled liquid. Such devices have been used to study cytoskeletal dynamics [83], activation and deactivation of temperature-sensitive gene products [105], and growth of bacterial and yeast cultures [106].

The tightest temperature control has involved incorporation of integrated electrode arrays made from materials that are not optically clear, and are therefore not compatible with microscopy. Integrated electrode arrays allow changes on the scale of tens of degrees within seconds, so these arrays have been used in such applications as on-chip PCR [107]. Thin film heaters have also been used in continuous flow PCR microfluidic chips, but the polyimide material is still not ideal for experimental needs requiring microscopy [108].

Controlled temperature increases are often less challenging than temperature decreases. To increase temperature, electric resistance or burning of fuel, for example, converts energy into heat. By the Second Law of Thermodynamics, transfer of heat will always be from a hotter object to a colder object in an isolated system due to entropy. However, actively cooling an object requires work to be done in opposition to the tendency toward disorder. Entropy in the cooled object decreases and the entropy of the environment around the system increases enough to compensate and then some, so that there is an overall increase in the entropy of the universe. As an example, there is no active cooling associated with cooling a standard laboratory hot plate to room temperature. Cooling usually consists of turning off the heating element and allowing the spontaneous process of the hot plate decreasing in entropy and the cooler air of the room increasing more in entropy.

1.2.3.1 Peltiers

Few methods exist for active cooling. One widely used method for small-scale biological studies makes use of the thermoelectic effect in which a temperature difference between two dissimilar conductive or semiconductive materials produces a voltage difference between the two materials. Conversely, when a voltage is applied to two dissimilar conductive or semiconductive materials, a temperature difference is created. The effect is also referred to as the Peltier-Seebeck effect, named after two physicists who each independently discovered the physical process [109, 110]. Peltier thermoelectric (TE) devices can actively cool one of their surfaces at the expense of the other side of the device being warmed. The choice of which TE device to use in an application is made based on its specifications:

V_{max} = max voltage at which the unit will be run (volts, V)

I_{max} = current drawn at V_max (amperes, A)

DT_{max} = difference in temperature between the hot and cold sides when run at V_{max} (degrees, °C)

Q_{max} = heat from the hot side at high load (watts, W)

When the TE device is run at a voltage less than V_{max}, called V current draw is

$$I = I_{max} \times \frac{V}{V_{max}} \tag{1.10}$$

and power draw is

$$P = I \times V \tag{1.11}$$

the thermoelectric cooler resistance is

$$R = \frac{V_{max}}{I_{max}} \tag{1.12}$$

and the Peltier constant, C, is

$$\frac{(Q_{max} + (I_{max})^2 \times \frac{R}{2})}{I_{max}} \tag{1.13}$$

The specifications of a commercially available peltier, including how the heat removed, waste heat, current drawn, and the coefficient of performance depend on input voltage and the temperature difference between the hot and cold sides are included in the appendices.

Peltiers have been used in several microengineered systems. In-line flow-through peltiers have been used to quickly change the temperature of a liquid injected into the temperature control layer of a bilayer microlfuidic device for studying microtubule dynamics in fission yeast [83]. In an application unrelated to cellular biology, peltier elements were integrated at the back of a printed circuit board (PCB) of a microfluidic chip (Fig. 1.13) for studying the extraction process of polymeric compounds during thermocycling of saltwater samples from the Jade Bay on the North Sea coast of Germany [111]. Pump and withdraw modes on a syringe pump were used to pump a sample into the hot zone and then back into the cold zone after thermal treatment to complete the desired amount of thermal cycles. Using the peltier elements, temperature in the chip reached equilibrium after 5 seconds.

Another approach was the miniaturization of the peltier to create a micro-peltier cooler encapsulated within a chip. A so-called "peltier junction" was created in which the peltier was used to pump heat from a chamber and into an adjacent microchannel, resulting in cooling of the chamber [112]. Depending on the current applied, different final temperatures were reached in the chamber. On average, a temperature decline from room temperature in the chamber to a specified temperature between $0°$-$10°$C took 10 s.

1.2.4 Nonshivering Thermogenesis

Warm-blooded animals (endotherms) try to maintain a homeostatic body temperature despite fluctuations in ambient temperature. Adipose tissue plays a key function in the

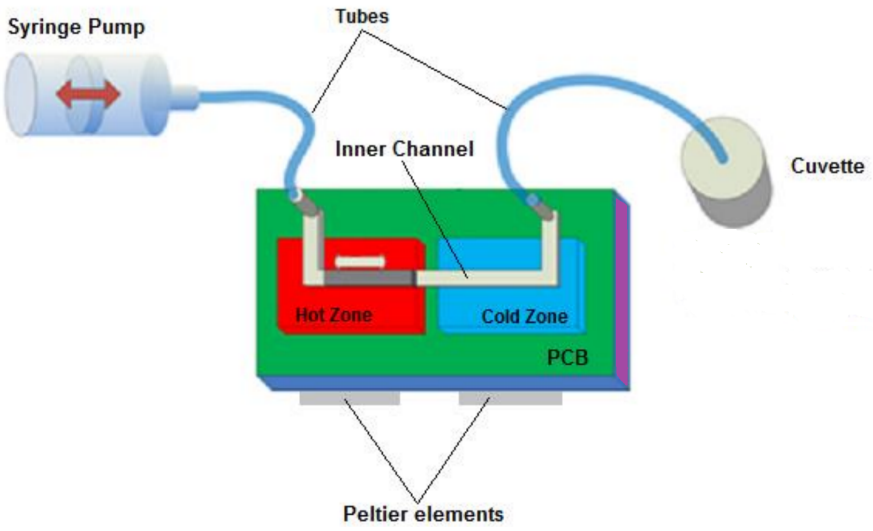

FIGURE 1.13: Schematic of the microfluidic device with a bidirectional flow syringe pump and two distinct temperature zones. Adpated from ref. [111].

adaptive mechanism to regulate body temperature. Specialized adipocytes respond to environmental decline in temperature by generating heat in a process known as nonshivering thermogenesis [113]. The heat-producing adipocytes that participate in nonshivering thermogenesis are called brown adipocytes and beige (also known as brite) adipocytes.

1.2.4.1 White, Beige, and Brown Adipocytes

The role of adipocytes is at the intersection of nutrition, energy expenditure, and health. White adipocytes are the most common type of adipocyte and primarily store energy, whereas brown and beige adipocytes dissipate energy by burning calories as heat. Brown adipocytes are named for their red-brownish appearance due to their large amount of iron-rich mitochondria. While there are designated depots of brown fat in humans, beige adipocytes are embedded in white fat depots. The other name for beige adipocytes—brite ("brown in white") adipocytes—is derived from that aspect. Brown adipocytes are usually smaller than white and beige adipocytes. Brown and beige adipocytes also have multiple lipid droplets while classical white adipocytes have a single, large lipid droplet.

Other differences include the location of the different kinds of adipocytes *in vivo*, specific biomarkers, and vascularization. A table summarizing the main differences among the three types of adipocytes is included (Table 1.2).

Brown adipocytes are believed to share the same myogenic factor 5 (Myf-5+) precursor cell as skeletal muscle. Beige and white adipocytes have been shown to originate from both Myf-5- and Myf-5+ precursors [115, 116]. Both brown and beige cells express uncoupling protein 1 (UCP1) in the mitochondrial inner membrane, and it is UCP1 that mediates heat generation in nonshivering thermogenesis. UCP1 creates a proton channel and collapses the proton gradient normally present across the inner mitochondrial membrane, thereby short circuiting ATP synthase [117]. As a result, the proton motive force is dissipated as heat rather than used to drive the motor on ATP synthase [118, 119] to generate ATP.

1.2.4.2 Brown Adipose Tissue in Humans

It was known that infants had large interscapular brown adipose tissue (BAT) depots, but the BAT was thought to not persist into adulthood. The serendipitous discovery of BAT in human adults reinvigorated research interest in BAT regulation. During functional imaging using positron emission tomography (PET) of breast cancer patients, highly metabolic regions not related to any pathology were appearing at the back of the neck [120]. These regions turned out to be metabolically active brown fat. The increased uptake of 2-[^{18}F]fluoro-2-deoxyglucose (FDG) is a hallmark of glycolytic tumors which is leveraged to localize tumors during PET scans. FDG is taken up by the GLUT family of glucose transporters (GLUT1, GLUT3, and GLUT4) and then phosphorylated by the enzyme hexokinase. Once phosphorylated, FDG cannot be further metabolized and thus it accumulates inside the metabolically active glycolytic cells [121].

At first, the symmetrical neck regions were attributed to false-positives caused by muscle tension due to anxiety [122]. However, computer tomography (CT) with its higher

TABLE 1.2: Differences among the three types of adipocytes. Adapted from [114]

Characteristic property	White	Brown	Beige
Morphology			
(i) Shape	Spherical	Ellipsoid/ polygonal	Spherical
(ii) Cell size	Variable, large (25–200 μm)	Small (15–60 μm)	Variable, smaller than white
(iii) Lipid droplet (LD)	Single large LD	Multiple small LD	Multiple LD with variable size
(iv) Mitochondria	+	+++	++ (upon stimulation)
Development	From Myf5- or Myf5+ precursors	From Myf5+ precursors	From Myf5- or Myf5+ precursors
Location	Subcutaneous and visceral	Suprarenal, paravertebral, supraclavicular	Inguinal, neck (near carotid sheath and musculus longus colli), other locations?
Function	Energy storage	Heat production	Adaptive thermogenesis
Uncoupling protein	Nearly undetectable	+++	++ (upon stimulation)
Adipocyte-type-specific markers	PPARγ, PLIN1, HOXC9, TCF21, TLE3, C/EBPα, Rb, Rip140	LHX8, ZIC1, EPSTI1, PRDM16, CIDEA, ELOVL3	HOXC8, HOXC9, CITED1, CD137, TMEM26, TBX1, CD40
Vascularization	Low	High	High (upon stimulation)
Impact on obesity	Positive	Negative	Negative
Correlation with insulin resistance	Yes	Probably yes	Probably yes

spatial resolution than PET, visualized the CT density of these neck regions and determined the density to be characteristic of adipose tissue [123, 124]. It has now been established that in adults, the largest depots of BAT are localized to supraclavicular and neck regions. Smaller depots can be found in some people in paravertebral, para-aortic, pericardial, and perirenal areas [125].

In the process of uncovering BAT by its uptake of FDG in PET scans, it was determined that a reduction in ambient temperature increased the uptake of FDG in the BAT. The scanners were kept in rooms with a cold ambient temperature, and cold temperature is a potent activator of nonshivering thermogenesis.

1.2.4.3 Cold Exposure Induces Thermogenesis

The canonical mechanism behind the adipocyte thermogenic response to cold is activation of the sympathetic nervous system which senses cold temperature. Released norepinephrine (NE) binds to β-adrenergic receptors and activates adenylyl cyclase. Increased production of cyclic adenosine monophosphate (cAMP) activates protein kinase A (PKA) and leads to subsequent activation of lipases to increase hydrolysis of triglycerides. The released free fatty acids (FFAs) bind UCP1 and activate its proton conductance [126–128]. Additionally, recent work has reported that mitochondrial reactive oxygen species are needed to sulfenylate a cysteine residue on UCP1 to sensitize the protein to FFAs [129]. Recent studies also show that adipocytes can directly sense cold temperature and respond by initiating thermogenesis without input from the sympathetic nervous system [130]. The mechanism by which adipocytes directly sense temperature remains unknown.

1.2.4.4 Therapeutic Potential

Manipulating thermogenesis could be an effective strategy to fight obesity. As of 2010, nearly 69% of adults aged 20 and over are overweight (25<BMI<29.9) or obese (BMI>30).

Strikingly, about one-third of children and adolescents ages 6-19 years of age are overweight or obese. Obesity is associated with such health risks as cardiovascular disease, type 2 diabetes, high blood pressure, stroke, nonalcoholic fatty liver disease, osteoarthritis, and certain types of cancer, including breast, colon, endometrial, and kidney. White adipose tissue (WAT) depots store energy in the form of triglycerides. The distribution of WAT influences the risk of metabolic disease. The accumulation of visceral fat (the intra-abdominal fat located around organs) is associated with higher health risk than the accumluation of subcutaneous fat (the fat under the skin) around the thighs and hips. In contrast, the activation of brown adipose tissue (BAT) promotes energy expenditure. In humans, BAT has such a large thermogenic capacity that it has been estimated that 50 g of maximally active BAT could utilize up to 20% of daily energy expenditure [131]. With such a substantial capacity to expend energy, there has been increased interest in targeting nonshivering thermogenesis in treating or preventing obesity-associated diseases.

Interest in the therapeutic potential of nonshivering thermogenesis has been split into two different approaches. The first is to expand the amount or increase the activity of one's endogenous thermogenic BAT. Transcriptional regulators, such as PRDM16, are believed to drive differentiation of precursors toward brown-like adipocytes. In human skin fibroblasts, PRDM16 has been shown to be sufficient to drive differentiation into cells with characteristics like those of a brown adipocyte [132]. Pharmacological small molecule intervention has also shown potential. For instance, dinitrophenol (DNP), a nonselective uncoupler of mitochondrial oxidation, has been shown to successfully increase energy expenditure, but serious side effects and known fatalities prevent its widespread use. Some candidate thermogenic compounds have been successful in reported research as weight loss drugs in humans, including sibutramine [133] and phentermine-topiramate [134]. The second approach is to transplant functional BAT or progenitors cells. Indeed, studies have shown that adult BAT transplantation had a beneficial effect on metabolic abnormalities in high fat diet (HFD)-induced obese, insulin-resistant mice [135, 136] and

genetically obese leptin-deficient mice [137].

1.2.4.5 Biological Assessment of Thermogenesis

Common methods to assess thermogenesis include *in vivo* and *in vitro* techniques. Core body temperature and respirometry are the most frequently employed *in vivo* measurements. Among *in vitro* measurements, cellular oxygen consumption, gene expression, and intracellular temperature have been used to demonstrate activation of thermogenesis.

***In Vivo* Respiration and Core Body Temperature** Many studies in mice have used a combination of respirometry and core body temperature measurements to demonstrate thermogenesis [92, 101, 138]. Respirometry is an indirect calorimetry approach that links respiratory oxygen and carbon dioxide exchange to metabolic heat production to measure energy expenditure. Generback *et al.* used both respirometry and core body temperature to show mice lacking UCP1 are cold-sensitive but not obese [138]. A study by Zhang *et al.* acquired respirometry and core body temperature measurements and demonstrated that the compound berberine activates thermogenesis in white and brown adipose tissue [139]. Ukropec *et al.* also used both techniques in demonstrating UCP1-independent thermogenesis in white adipose tissue of mice [140]. As a final example, Albert *et al.* used a combination of core body temperature and maximal respiration to demonstrate adipose tissue-specific inactivation of mTORC2 in mice created a hypothermic phenotype in which the mice were unable to maintain stable body temperature upon cold exposure [92].

Gene Expression. Assessment of thermogenesis has relied heavily on PCR data to show upregulation of thermogenic genes (e.g. UCP1, PGC1α, Dio2) [141–144]. These genes have been shown to be vastly upregulated in response to cold and are considered the canonical cold-induced genes in thermogenic adipocytes [130, 145]. The protein UCP1 is in the inner mitochondrial membrane and thought to be responsible for

nonshivering thermogenesis (see section 1.2.4.1). The protein peroxisome proliferator-activated receptor-gamma coactivator (PGC1α) is a protein that plays a central role in cellular energy metabolism regulation and mitochondrial biogenesis. Mitochondrial biogenesis is important to give thermogenic adipocytes more mitochondrial mass to meet the demand for increased respiratory activity during thermogenesis. Iodothyronine deiodinase 2 (Dio2) is the enzyme that converts thyroid hormone intracellular thyroxine (T4) into 3,5,3-triiodothyronine (T3) previously found to be essential for adaptive thermogenesis in BAT [146]. Studies in mice often include expression levels of thermogenic genes in adipose tissue [92, 129, 140]. Studies that do not have an *in vivo* component, such as the demonstration of direct sensing of temperature by adipocytes, largely measured the upregulation of thermogenic genes as the readout for thermogenesis [130, 147, 148].

Oxygen Consumption. Thermogenic capacity of adipocytes is thought to be reflected in the ability of adipocytes to increase oxyen consumption in response to the addition of the sympathetic neurotransmitter norepinephrine. The oxygen consumption rate (OCR) is routinely measured *in vitro* as an indicator of enhanced thermogenesis. In earlier studies, *in vitro* oxygen consumption was measured with Clark-style electrodes [149–152]. In more recent studies, commercially available extracellular flux analyzer instruments (Agilent Seahorse XF Analysis) have become the most popular method to measure OCR [148, 153, 154].

Intracellular temperature Despite the fact that thermogenesis at the cellular level is intracellular heat generation, there is little data on the actual intracellular temperature changes within adipocytes. Numerous technologies to measure intracellular temperature have been developed. Methods include the use of quantum dots[137, 155] fluorescent thermometers[156–160]and contact-based microcantilevers [161] or microthermocouples [162, 163]. To date, some of these tools have demonstrated cellular thermogenesis or mitochondrial thermogenesis in a variety of cell types including brown adipocytes [157,

161, 164], but intracellular temperature measurements in adipocytes have always been in response to chemical induction of thermogenesis by carbonyl cyanide 3-chlorophenylhydrazone (CCCP), NE, or isoproterenol as opposed to direct cold exposure.

CHAPTER 2. MATERIALS AND METHODS

Portions of this content have previously been published in Rexius-Hall, M. L., Mauleon, G., Malik, A.B., Rehman, J., and Eddington, D.T. (2014) Microfluidic platform generates oxygen landscapes for localized hypoxic activation, Lab Chip. 14(24):4688-95 and Rexius-Hall, M.L., Rehman, J., and Eddington, D.T. (2017) A microfluidic oxygen gradient demonstrates differential activation of the hypoxia-regulated transcription factors HIF-1α and HIF-2α, Integr. Biol. Advance Article DOI 10.1039/C7IB00099E.

2.1 Large-Area Oxygen Landscape Cell Culture Platform

2.1.1 Open-well Device Design

Building on the methods developed in our laboratory [65, 66, 74], a large-area open-well device was developed to maintain a stable oxygen gradient and accommodate standard biochemical assays to permit real-time monitoring of interactions between differentially oxygenated cells.

2.1.2 Device Fabrication

Designs for large-area binary, square wave, oscillating, and linear gradient oxygen profiles for a cell culture platform were developed (2.1). Channel network designs were made in AutoCAD, and the design elements in black (bottom row) represented the microchannels. The dual condition binary landscape was created using two microfluidic perfusion networks (500 μm wide and 300 μm deep) separated by a 500 μm wide gap (Fig. 2.1A). A gas composition of 5% CO_2, balanced nitrogen was designed to flow through the left network and 5% CO_2, balanced air was designed to through the right network. The square wave landscape consisted of two separate networks (500 μm wide and 300 μm deep) with 500 μm spacing between channels (Fig. 2.1B). The outer network was designed to be supplied with 5% CO_2, balanced nitrogen and the central, inner network with 5% CO_2,

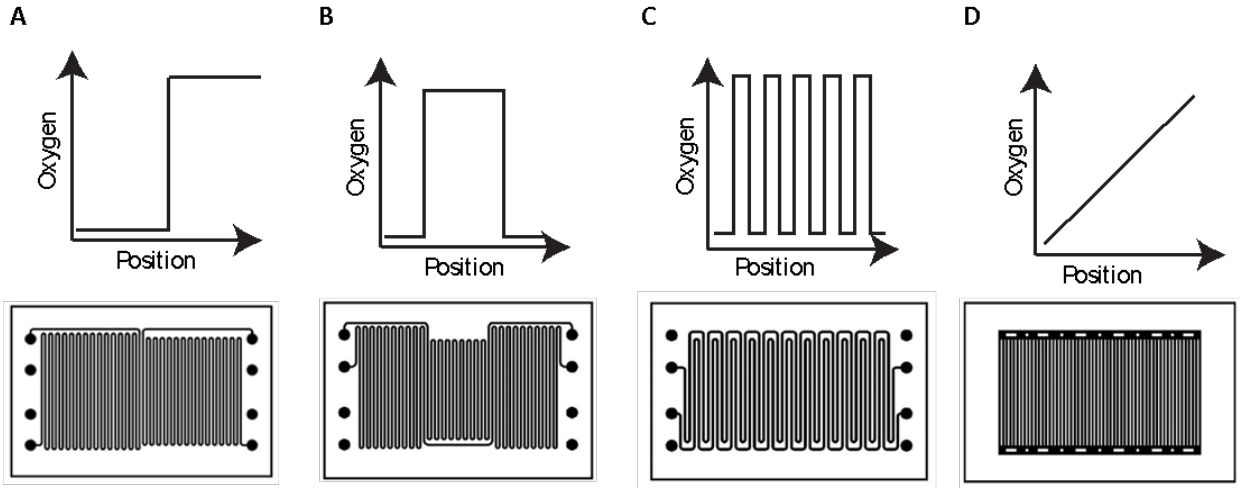

FIGURE 2.1: Microfluidic network designs allow for a variety of oxygen landscapes. The ideal oxygen profile as a function of position in the x-direction and the gas network channel design is shown for the (A) binary dual condition, (B) square wave, (C) oscillating, and (D) linear oxygen landscape.

balanced air. The oxygen profile for an oscillating oxygen landscape was created with a channel pattern of two interdigitated serpentine networks (Fig. 2.1C) (one to be perfused with 5% CO_2, balanced air and the other with 5% CO_2, balanced nitrogen), resulting in oscillations in the x-direction. Channels were 625 μm wide and 300 μm deep with 625 μm spacing between channels. A near-linear gradient was designed to use 5 oxygen compositions as inputs. Five inlet and five outlet ports (3.2 mm diameter) were at the sites of the five small, white circles (1 mm diameter) for 0%, 5%, 10%, 15%, and 21% O_2 introduction into the inlet ports from left to right, respectively (Fig. 2.1D). The design was a single chamber (200 μm deep) with a series of barrier walls (500 μm wide) spaced 500 μm apart. The different gas compositions mix and perfuse the spaces separated by the walls to distribute a relatively linear gradient in the x-direction.

Standard soft lithography techniques were used for microfabrication. To make an SU-8 master mold, a layer of SU-8 2150 negative photoresist (MicroChem) was spun on a dehydrated 100 mm diameter silicon wafer (University Wafer) at 2000 rpm for 30 seconds (s) (Fig. 2.2A-B). The wafer was then pre-baked at 65°C for 5 minutes (min) and

soft-baked at 95°C on a hotplate for 120 min. The wafer was then removed from the hotplate and allowed to cool to room temperature. The microchannel network design file from AutoCAD was printed as a high-quality photomask (Fineline Imaging). The desired photomask was placed onto the SU-8 surface of the wafer (Fig. 2.2C) and was exposed to a UV light source at 100% intensity for a duration defined as

$$\text{Exposure Time} = \frac{\text{Exposure Energy} \times \text{Surface Area}}{\text{Lamp Output}} \tag{2.1}$$

where the exposure energy ($\frac{mJ}{cm^2}$) was provided by the SU-8 manufacturer, the surface area of the 100 mm diameter wafer was 78.54 (cm^2), and the lamp output ($\frac{mJ}{s}$) was measured on the UV light source from a radiometer. In practice, the exposure time given by equation 2.1 was then doubled to better cross-link the SU-8. The wafer was then post-exposure pre-baked at 65°C for 5 min and post-exposure baked at 95°C for 30 min. After cooling to room temperature, the wafer was immersed in SU-8 developer (MicroChem) for 30 min with gentle agitation on a benchtop shaker to dissolve the SU-8 that was not cross-linked into the pattern design during UV exposure (2.2D). The end result was rinsed in acetone and isopropyl alcohol (IPA) and dried under an N_2 stream to finalize the SU-8 master mold.

Channel features were replicated in polydimethylsiloxane (PDMS) (Sylgard 184 Silicone Elastomer; Dow Corning Corp., Midland, MI). PDMS was chosen for its well-characterized oxygen diffusivity, biocompatibility, and optical clarity. PDMS prepolymer was added with the curing agent at a weight ratio of 10:1 (polymer:curing agent). The PDMS was mixed and degassed in a planetary centrifugal mixer (Thinky; Laguna Hills, CA) and cast on a silicon master containing SU-8 (MicroChem) microchannel features.

The PDMS platform (Fig. 2.3) was a multilayer construction. First, a PDMS channel network layer (cured at 85°C on a hot plate for 2 h) was punched with inlet/outlet ports (3.2 mm diameter). Second, the thin, PDMS membrane was made by spinning uncured, degassed PDMS on a 100 mm diameter silicon wafer (Silicon Sense, Inc., Nashua, NH) at 800 rpm for 30 s using a spin coater (Laurell Technologies Corporation, North Wales, PA).

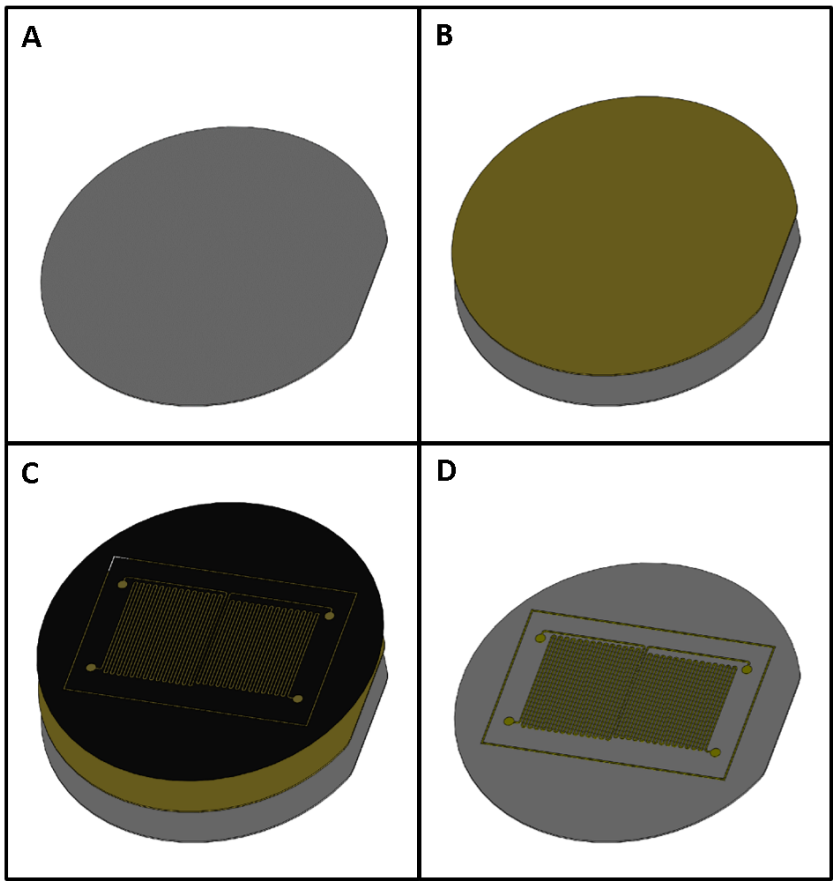

FIGURE 2.2: (A) A clean 100 mm diameter silicon wafer was dehydrated on a 120°C hotplate for 5 min. (B) A negative photoresist was spin-coated on the silicon wafer and soft-baked. (C) A photomask with the desired design was placed on the negative photoresist surface and exposed to UV light. (D) Developer removed all the unexposed regions of the photoresist, leaving behind the microchannel design.

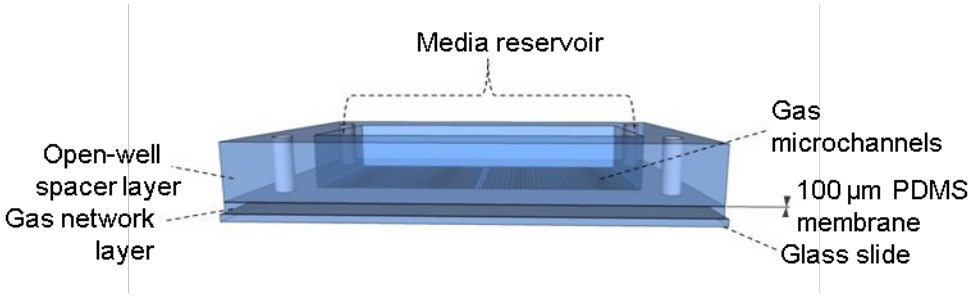

FIGURE 2.3: The open-well microfluidic platform generates oxygen landscapes across a cell culture. The multi-layered construction consists of a glass slide, gas network layer with microchannels, 100 μm thick PDMS diffusion membrane, and open-well spacer layer which forms the media reservoir.

After curing at $60°$C for 50 min, the 100 μm-thick membrane was bonded to the channel network layer using a 3 min surface treatment from a handheld corona discharge device (Electro Technic Products, Chicago, IL). The corona discharge device was used in room air at room temperature at its maximum output power of 30 watts. The bonded membrane was punched with inlet/outlet ports, and the PDMS construct was then bonded on a 75 mm x 50 mm glass slide (Fisher Scientific). The open-well spacer layer was cut as a rectangle of PDMS (8 mm thick) with outer dimensions equal to those of the channel network construct with matching access ports. An inner rectangle of PDMS (offset 9.35 mm from the shorter of the rectangular edges and 11.6 mm from the longer edge) was removed to create the walls of the open well. The open-well spacer layer was punched with matching access ports and bonded on top of the PDMS membrane.

2.1.2.1 Dual Condition Device

Utilization of the binary dual condition device was the focus of further details concerning device layout and design (Fig. 2.4). The device dimensions gave an approximately $14\,\mathrm{cm}^2$ cell culture area (Fig. 2.4A) which was approximately 1.5 times the area of a well in a standard 6-well plate. Using the binary dual condition design with hypoxic oxygen levels flowing through one network and normoxic oxygen levels flowing through the adjacent network, distinct regions of differential oxygenation and a steep gradient in the

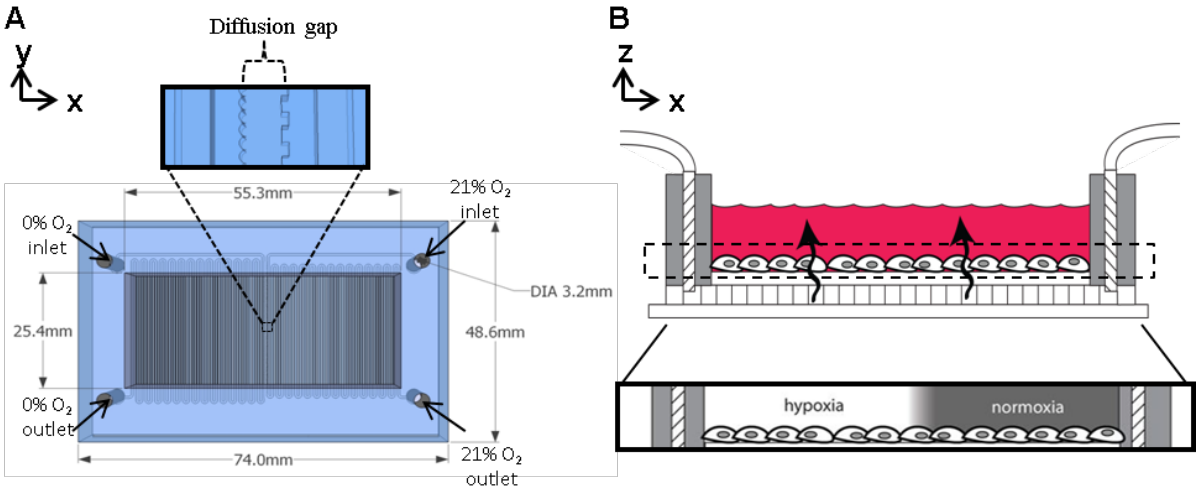

FIGURE 2.4: Device schematic of the open-well microfluidic platform for generating oxygen landscapes across a cell culture. (A) Dimensions detail the device layout and provide a large culture area. Adjacent serpentine networks are separated by a 500 μ diffusion gap designed with edge microfeatures for easy identification under a microscope. (B) The cross-sectional schematic demonstrates how the device functions. The choice of inlet gases permits a dual condition oxygen landscape to be established close to the membrane with a steady hypoxic region (white), a steady normoxic region (grey), and a steep gradient in the diffusion gap.

diffusion gap was designed to be imposed on a cell monolayer (Fig. 2.4B). In homogeneous hypoxia control devices, 5% CO_2, balanced nitrogen flowed through both the left and right network. Similarly, in homogeneous normoxia control devices, 5% CO_2, balanced air flowed through both the left and right network.

2.1.3 Oxygen Modulation Setup

Oxygen modulation was performed by constant perfusion of desired gas compositions from compressed gas tanks. Plastic connectors (McMaster-Carr) were inserted into the cored access ports of the device. Tygon tubing with a 1/16 inch inner diameter and 1/8 inch outer diameter (Cole-Parmer, Vernon Hills, IL) interfaced with the device, and a glass tube rotameter (Omega Engineering, Inc., Stamford, CT) was used to control the gas flow rate. Gases were flowed at a rate of 30 mL/min through the device.

2.1.4 Oxygen Sensor Fabrication

The surface oxygen profile was characterized using gas-permeable 100 μm PDMS membrane impregnated with platinum(II) octaethylporphyrinketone (PtOEPK). The fluorescence of the PtEOPK fluorophore in the membrane was quenched in the presence of oxygen. First, polystyrene (PS) (pellets 200,000 MW, Sigma-Aldrich) was dissolved in toluene (35% w/w toluene/PS). The solution was tightly sealed to prevent toluene evaporation and was placed on a benchtop shaker for 24 hours for complete dissolution. PtOEPK was added at 0.5 mg/mL of PS/toluene mixture. The mixture was spin-coated on a cured PDMS membrane at 2000 rpm and left under a fume hood to evaporate the toluene for 24 hours. The PS/toluene-coated wafer was exposed to light during the evaporation process to reduce the photobleaching observed during experiments. The dried polystyrene was washed away with isopropanol, leaving behind a PDMS membrane impregnated with PtOEPK that could easily be cut to convenient sizes for desired sensors.

2.1.5 Oxygen Profile Validation

With the sensor on top of the PDMS membrane, the device was filled with 5 mL of water prior to beginning gas perfusion. Scanning imaging was used to determine the surface percent oxygen profile. Scans were taken 1 h after introducing gas flow. Fluorescent intensity in the images was converted to percent oxygen by solving the Stern–Volmer equation.

$$\frac{I_0}{I} = 1 + K_{sv}[Q] \tag{2.2}$$

where I_0 is the intensity of the sensor in the absence of oxygen, K_{sv} is the Stern-Volmer constant, and Q is the oxygen concentration. K_{sv} can be solved for using two known calibration points where one calibration point is in the absence of oxygen (0% O_2):

$$K_{sv} = \frac{I_0 - I_c}{I_c[Q_c]} \tag{2.3}$$

Scans of the sensor in 5% CO_2, balanced nitrogen and 5% CO_2, balanced air were used to calibrate the sensor measurements.

2.1.6 Dissolved Oxygen Measurements

The dissolved oxygen content was measured using a hand-held optical sensor (Neofox; Ocean Optics). The tip of the oxygen probe contains a ruthenium compound that is quenched in the presence of oxygen. Sensor calibration was performed according to the manufacturer's instructions. During calibration, first 5% CO_2, balanced nitrogen was injected into both microfluidic networks, and then only 5% CO_2, balanced air was injected through the device. An electronic micromanipulator was used to hold the oxygen probe and adjust the x, y, and z planes with a resolution of 0.1 μm inside the open well. We used the electronic micromanipulator to precisely adjust the vertical distance of the probe's tip from the surface of the PDMS membrane within the well.

2.1.7 Cell Culture

Fabricated devices were autoclaved at 121°C for 30 min prior to use. Then, 2 mL of 0.1% gelatin (porcine skin type A; Sigma-Aldrich) in E-pure water (Barnstead Thermolyne, Dubuque, IA) was added to the open-well reservoir and incubated at 37°C overnight. After excess gelatin was aspirated, cells were seeded at 300,000 cells per device in 5 mL of the associated culture media. HLMVECs (HMVEC-L; Lonza) were cultured in EGM-2 with supplements (EGM-2 MV with bullet kit; Lonza). Human bone marrow-derived MSCs (hMSC; Lonza) were cultured in complete culture medium (CCM) with fetal bovine serum (FBS), which is comprised of Minimum Essential Medium Alpha (αMEM), 20% FBS, 2 mM L-glutamine, and 100 units/mL penicillin and streptomycin. Devices seeded with cells were placed in Petri dishes and housed in a standard incubator at 37°C in 5% CO_2, balanced air. Prior to oxygen modulation studies, media was changed every 24 h until cells reached >90% confluency.

2.1.8 In-device Immunofluorescent Staining

Immunofluorescent staining of transcription factor HIF-1α was performed on a confluent monolayer of HLMVECs after 12 h of dual condition constant perfusion. Cell culture media was carefully aspirated, and the cells were then washed three times with 4°C PBS, fixed with 4% paraformaldehyde for 10 min at room temperature, and washed three additional times with PBS. Cells were permeabilized in 0.2% Triton X-100 in PBS for 10 min at room temperature, washed three times with PBS, and blocked in blocking buffer (X0909; Dako, Carpinteria, CA) for 1 h at room temperature. Cells were subsequently incubated with anti-HIF-1α antibody (Novus Biologicals, Littleton, CO) with a 1:100 dilution in antibody diluent (S3022; Dako) in a humidified chamber overnight at 4°C. After three washes with Tris-buffered saline with Tween-20 (TBST; Boston Bioproducts, Boston, MA), cells were incubated with fluorescent secondary antibody (Alexa Fluor 488; Invitrogen, Carlsbad, CA) in antibody diluent with a 1:300 dilution for 2 h at room temperature. Cells were washed three times with TBST and nuclei were stained (Hoechst 33342; Invitrogen) with a 1:5000 dilution in washing buffer (10 mM Tris HCl, pH 7.4, 100 mM NaCl, and 0.10% Tween-20 in distilled water) for 20 min at room temperature.

2.1.9 Protein Extractions and Western Blotting

With the injected gases still flowing through the device, the device was placed on ice. Media was aspirated, and the cells were washed twice with cold phosphate buffered saline (PBS) containing 10 mM phenylmethylsulfonyl fluoride (PMSF). A volume of 100 μL PBS was added back to the well and cells were separately scraped from the leftmost third of the device (a 25.4 mm by 18.4 mm area) and the rightmost third of the device with a cell scraper. In the dual condition configuration, the leftmost third corresponded to a region of steady hypoxia and the rightmost third corresponded to a region of steady normoxia. Cells cultured on the central third of the device's membrane, containing the gradient region of the dual condition configuration, were also collected for analysis (data

not shown). Then, the cells from each of these regions were collected in a separate pipet tip and transferred to a microcentrifuge tube.

The cells were centrifuged at 1400 rpm for 5 min at a temperature of 4°C. The remaining PBS was aspirated from the cell pellet, and the pellet was resuspended in 50 μL of RIPA buffer (10 mM Tris [pH 8.0], 140 mM NaCl, 1% Triton X-100, 1% sodium deoxycholate, and 0.1% sodium dodecyl sulfate [SDS]) for total cell lysis. Lysates were incubated on ice for 15 min with intermittent vortexing. Protein concentration of each lysate was determined by the BCA assay (Pierce BCA Protein Assay Kit; Thermo Scientific) using bovine serum albumin as the protein concentration standard. Equivalent amounts of protein (30 μg) were separated by SDS-PAGE and then transferred to nitrocellulose membranes using standard procedures. The membrane was blocked with 3% bovine serum albumin (BSA) in Tris-buffered saline (TBS) for 1 h. After blocking, membranes were incubated at 4°C overnight with 3% BSA in TBS, containing anti-LDHA (Santa Cruz Biotechnology, Dallas, TX). After 3 washes in TBS with 0.05% Tween (TBST), membranes were incubated with corresponding horseradish peroxidase-conjugated secondary antibodies in 5% milk in TBST (1:5000) for 1 h. A final series of three washes (10 min each) in TBST were performed before developing the blots according to kit directions (SuperSignal West Pico Chemiluminescent Substrate; Thermo Scientific).

2.1.10 Quantitative Real-time PCR

After 24 h of dual condition constant perfusion, relative gene expression of Glut1, PDK isozymes, and LDHA in human MSCs was determined using quantitative real-time PCR. First, media was aspirated and cells were washed three times with room temperature PBS. The device was cut in equal thirds (a left, middle, and right section) to ensure separation of the cells subjected to distinct oxygen levels. The cells were then scraped off each section with a cell scraper and lysed in 300 μL of lysis buffer. Lysis buffer consisted of 10 μL of β-mercaptoethanol (Sigma Aldrich) per 1 mL of lysis buffer (PureLink

RNA Mini Kit; Invitrogen). The lysates were collected in a pipet tip and transferred to an RNAse/DNAse-free microcentrifuge tube and placed in -80°C for storage prior to RNA isolation. RNA was extracted with a PureLink RNA Mini Kit (Invitrogen) according to the manufacturer's instructions. Synthesis of cDNA from total RNA was performed using a High-Capacity cDNA Reverse Transcription Kit (Applied Biosystems, Foster City, CA), and RT-PCR was carried out on Applied Biosystems ABI PRISM 7000 detection system in 25 μL reactions containing 12.5 μL of TaqMan Gene Expression Master Mix. Relative gene expression of target gene mRNA was performed using TaqMan Gene Expression Assays (Applied Biosystems) and was calculated using beta-2-microglobulin (B2M) as the endogenous control.

2.1.11 Statistical Analysis

All human cell culture experiments were repeated at least three independent times, and data are expressed as the mean $\pm$ SEM. Significance was determined from one-way ANOVA with Tukey's multiple comparison post-test. Analyses were performed with Prism 5 by Graphpad.

2.2 Linear Oxygen Gradient Device

2.2.1 Device Fabrication

The microchannel layer was fabricated using standard soft lithography techniques. Briefly, polydimethylsiloxane (PDMS) (Sylgard 184 Silicone Elastomer, Dow Corning) base was added to the curing agent at a weight ratio of 10:1. The mixture was mixed and degassed in a planetary centrifugal mixer (Thinky; Laguna Hills, CA) and cast on a silicon master containing SU-8 (MicroChem) microchannel features. The microchannel dimensions were 500 μm (width) x 20 mm (length) x 100 μm (height). The PDMS channel layer was cured at 85°C on a hot plate for 2 h and inlet/outlet ports were punched with a 15 gage (1.37 mm ID, 1.83 mm OD) blunt needle. The PDMS membrane was fabricated by

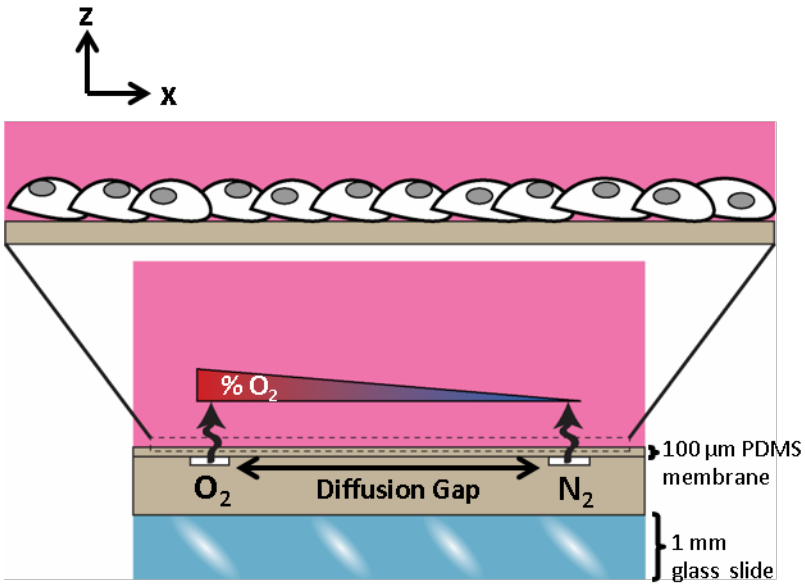

FIGURE 2.5: Constant perfusion of the compressed gases oxygen and nitrogen into microchannels separated by a diffusion gap exposes cells to a spatial linear oxygen gradient. A schematic cross-sectional view of the microchannel device demonstrates diffusion from an oxygen channel and a nitrogen channel across a thin PDMS membrane establishes an oxygen gradient to which cells cultured on the membrane are exposed.

spinning uncured, degassed PDMS (10:1 weight ratio of base to curing agent) on a 100 mm diameter silicon wafer (University Wafer, Boston, MA) at 1000 rpm for 30 s using a spin coater (Laurell Technologies Corporation, North Wales, PA). After curing at 60°C for 40 min, the membrane was bonded to the microchannel layer using surface treatment from a handheld corona discharge device (Electro Technic Products, Chicago, IL). The bonded membrane was punched with inlet/outlet ports, and the PDMS construct was then bonded on a 75 mm x 50 mm glass slide (Fisher Scientific).

Two microfluidic perfusion channels were separated by varying widths of a diffusion gap (Fig. 2.5). One channel was continuously perfused with 5% CO_2, balanced air and the second channel was continuously perfused with 5% CO_2, balanced nitrogen. Diffusion of the gases across the 100 μm membrane and into the bulk created a linear gradient surface oxygen profile to which the cells cultured on the membrane were exposed.

2.2.2 Oxygen Modulation Setup

Improving upon the experimental setup of Section 2.1.3, the linear oxygen gradient device incorporated mini gas regulators and manometers to stabilize and monitor the pressure in the microchannels, respectively. Oxygen conditions were modulated by introducing desired gas compositions from compressed gas tanks. Plastic connectors (McMaster-Carr) interfaced between the access ports of the device and the tubing (Tygon 1.59 mm (1/16 inch) ID and 3.18 mm (1/8 inch) OD; Cole-Parmer) supplying the compressed gas. The gas pressure was stabilized by running polyurethane tubing (6.35 mm (1/4 inch) OD, McMaster-Carr) from the gas regulator on the compressed gas tank to a glass tube rotameter (Omega Engineering, Inc., Stamford, CT) and then to a mini gas regulator (Marsh Bellofram, Newell, WV) and into a microchannel of the device (Fig. 2.6). The connection of a manometer (Dwyer Instruments, Michigan City, IN) by a three-way valve allowed for real-time monitoring of the pressure within the microchannel. The pressure in the two microchannels was kept equal at 5 psi (34.5 kPa) to establish a stable oxygen gradient and minimize variation within and between experiments.

2.2.3 Oxygen Sensor Fabrication

The same methods used to fabricate sensors for the large-area oxygen landscape cell culture platforms was employed. See Section 2.1.4 for details.

2.2.4 Oxygen Profile Validation

Prior to beginning perfusion of compressed gas, the PDMS oxygen sensor was placed on top of the device's PDMS membrane and the open well was filled with 5 mL of PBS. Scans across the sensor were used to determine the surface percent oxygen profile. Scans were taken over a 4 h period after introducing gas flow. Percent oxygen was plotted from the fluorescent intensity by solving the Stern–Volmer equation. The hypoxic channel was perfused with 5% CO_2, balanced nitrogen, and the normoxic channel was perfused with

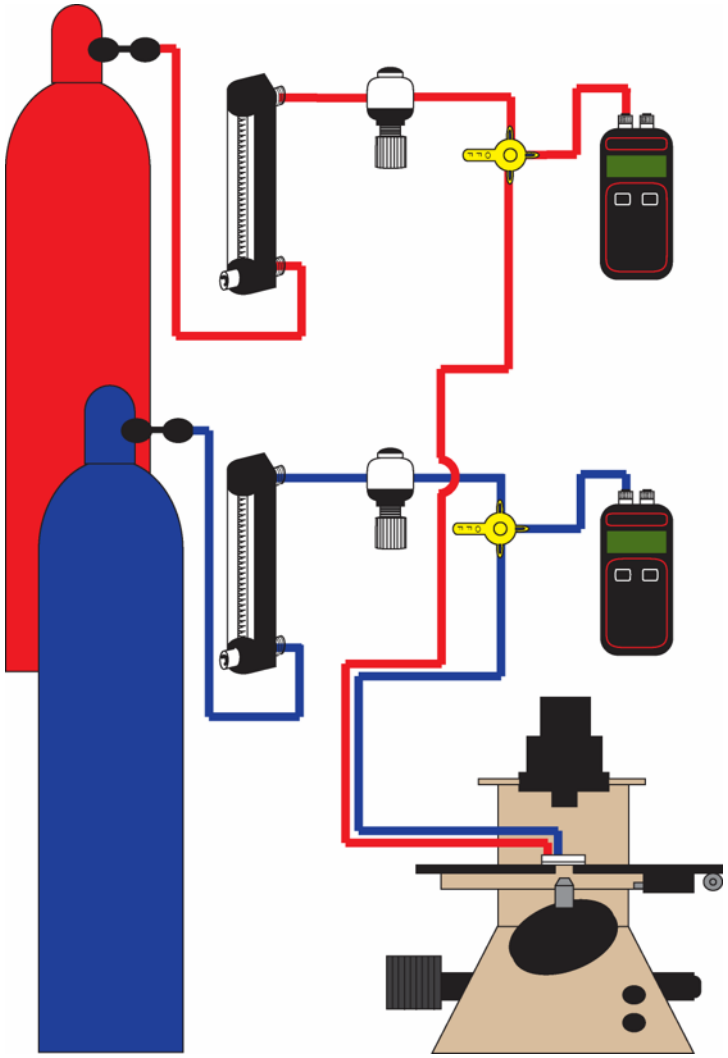

FIGURE 2.6: The experimental setup schematic for gas perfusion shows flow from a compressed gas tank to a glass tube rotometer and then through a mini gas regulator and into a microchannel of the device. The connection of a manometer by a three-way valve is used to monitor equal pressure within each microchannel.

5% CO_2, balanced air. The fluorescent intensity of the sensor at 4 h within the region directly above the hypoxic channel when perfused with 5% CO_2, balanced nitrogen while nitrogen gas was injected in the environment surrounding the device was used as the 0% O_2 calibration. The fluorescent intensity of the sensor directly above the normoxic channel under ambient conditions prior to gas perfusion was used as the 21% O_2 calibration. The fabrication and oxygen validation of the homogeneous control devices is reported in Section 2.1.2.

2.2.5 Cell Culture

Fabricated devices were autoclaved and then filled with 2 mL of 0.1% gelatin (porcine skin type A; Sigma-Aldrich) in water. Gelatin was incubated at 37°C overnight on the PDMS membrane. Gelatin was then aspirated, and endothelial cells were seeded at 250,000 cells per device. The human cerebral microvessel endothelial cell line hCMEC/D3 was cultured in EGM-2 MV (Lonza). Devices with cells were placed in Petri dishes and kept in a standard incubator at 37°C in 5% CO_2, balanced air. Media was changed every 24 h until cells reached >80% confluency.

2.2.6 In-device Immunofluorescent Staining

Cell culture media was aspirated, and the cells were washed twice with PBS, fixed with 4% paraformaldehyde for 10 min at room temperature, and washed two additional times with PBS. Cells were permeabilized in 0.2% Triton X-100 in PBS for 10 min at room temperature, washed three times with PBS, and blocked in 3% bovine serum albumin (BSA) in phosphate-buffered saline with Tween 20 (PBST) for 1 h at room temperature. Cells were subsequently incubated with anti-HIF-1α antibody or anti-HIF2α antibody (Novus Biologicals, Littleton, CO) with a 1:200 dilution in 3% BSA in PBST overnight at 4°C. After three washes with PBST, cells were incubated with fluorescent secondary antibody (Alexa Fluor 633; Invitrogen, Carlsbad, CA) in 3% BSA in PBST with a 1:300 dilution

for 2 h at room temperature. Cells were washed three times with PBST and nuclei were stained (Hoechst 33342; Invitrogen) with a 1:5000 dilution in PBST for 10 min at room temperature. Then a drop of antifade mounting solution (ProLong Gold AntifadeMountant; Thermofisher) was added directly to the immunostained cells on the membrane, a glass coverslip was placed on top, and left to cure in the dark for 24 h before imaging.

2.2.7 Microscopy and Image Analysis

Images were acquired using a confocal laser scanning microscope (Zeiss LSM 710). Devices were placed upside down in the slide-holding stage insert to be imaged on the inverted confocal microscope. The entire gradient was imaged using the tiling function in the Zen imaging software. A63X Plan-Apochromat (1.46NA) objective was used during acquisition. Images were processed using FIJI open-source software. Nuclear/cytosolic ratios were determined as follows: a nuclear mask was made from the Hoechst staining channel. Images acquired of the HIF staining channel were background subtracted and filtered (median). The nuclear mask was applied to quantify the mean pixel value of the 12-bit image (intensity min, max: 0, 4095) within the nuclear regions of the HIF staining channel per field of view frame. The mask was also used to subtract the area of the nuclei, leaving behind the cytosolic staining. The cytoplasmic signal was determined as the mean pixel value of the area in a field-of-view frame thresholded above a set background value (100 was used for HIF-1α and 200 was used for HIF-2α). The nuclear/cytoplasmic ratio was measured by dividing the mean nuclear value by the mean cytoplasmic value.

2.2.8 Statistical Analysis

Cell culture experiments were repeated three independent times. During each independent experiment, three scans of the cells across the gradient were acquired. The data are expressed as the mean $\pm$ SEM. Significance was determined from a two-way ANOVA

with Bonferroni's multiple comparison post hoc test. Analyses were performed using Prism 5 by Graphpad.

2.3 Temperature Control of the Adipocyte Microenvironment

2.3.1 Preadipocyte and Adipocyte Cell Culture

Human subcutaneous preadipocytes (SP-F-1, Zenbio) were cultured in preadipocyte medium (PM-1, Zenbio). Prior to differentiation, preadipocytes were plated according to the manufacturer's instructions. Briefly, preadipocytes were seeded at a density of 40,625 cells/cm^2. Twenty-four hours after plating, adipocyte differentiation was induced by aspirating preadipocyte medium from confluent preadipocytes and adding adipogenic differentiation medium (3% fetal bovine serum (FBS), 0.25 mM isobutylmethylxanthine (IBMX), 66 μM d-biotin, 34 μM d-pantothenate, 5 μM rosiglitazone, 1 μM dexamethasone, and 200 nM human insulin in DMEM/Ham's F-12). After 7 days of induction, cells were then maintained in adipocyte nutrition medium (prepared identically to adipogenic differentiation medium except it does not contain IBMX and the rosiglitazone concentration is reduced to 1 μM). Unless otherwise indicated, cells used in thermogenic studies were differentiated 11-14 days (7 days in adipogenic differentiation medium and 4-7 days in adipocyte nutrition medium).

2.3.2 Introduction of the Fluorescent Thermoprobe into Cells

Cell culture medium was aspirated, the cells were washed with a solution of 5% glucose in biological-grade water. Cells were then treated with a 5% glucose solution containing 0.05% w/v of the thermoprobe. After incubation at 4°C for 10 min, the cells were washed once with PBS and replaced with phenol red-free DMEM supplemented with 3% FBS for live-cell imaging.

2.3.3 Confocal Microscopy and Image Analysis

Human subcutaneous preadipocyte and adipocyte cells treated with intracellular thermometer were observed using a confocal microscope (LSM 710, Zeiss) with a 63x Plan-Apochromat (1.46NA. Zeiss) objective. The adherent cells were directly imaged in glass-bottom dishes (MatTek, Ashland, MA). Laser excitation of the temperature-sensitive channel was 458 nm, and the signal was collected from 559-621 nm. The reference (temperature-insensitive) channel was excited at 488 nm, and the signal was collected from 492-526 nm. The environmental temperature was controlled with a microscope cage incubation chamber (Heating Unit XL S, Zeiss). The media temperature was monitored using a dual automatic temperature controller (TC-344B; Warner Instruments) and an attached bead thermistor cable (TA-29; Warner Instruments). The ratiometric images were created and analyzed in FIJI open-source software.

2.3.4 Lattice Light Sheet Microscopy and Image Analysis

Images were collected on a custom lattice light sheet instrument. Imaging was conducted at room temperature (21°C) in phenol red-free DMEM supplemented with 3% FBS. Each sample was cultured on a 5 mm coverslip and mounted in a custom sample holder. Images were acquired using a Nikon CFI Apo LWD 25x water-dipping, 63x magnification, 1.1 NA, 3 mm working distance objective. The lattice light sheet instrument was equipped with 2 Hamamatsu Orca Flash 4.0 sCMOS cameras to capture the ratiometric probe emissions without temporal delay. The thermoprobe was excited at 488 nm and collected by the two cameras for ratiometric image analysis. Mitochondria were excited at 642 nm and captured sequentially after the thermoprobe per slice. Images were acquired every 5 min with a 3D stack of 256 slices for at least 24 time points. Lattice light sheet microscopy has been previously published [165–167]. Briefly, the instrument created a parallel array of regularly-spaced, coherently-interfering Bessel beams. The sample was moved through the lattice pattern, resulting in deskewed raw data. Deskewing and deconvolution were

performed using a custom Matlab-based GUI, and movies were made using the Imaris software (Bitplane).

2.3.5 Quantitative Real-time PCR

Total RNA was extracted with TRIzol (Invitrogen, Carlsbad, CA) according to the manufacturer's instructions. The relative expression of each gene was determined with real-time PCR. Briefly, cDNA was synthesized from total RNA using the High-Capacity cDNA Reverse Transcription Kit (Applied Biosystems, Carlsbad, CA). Real-time quantitative PCR was carried out on an Applied Biosystems ViiA7 instrument in 10 μl reactions containing 6.25 μl of FastStart Universal SYBR Green master mix. Relative gene expression of target gene mRNA was calculated using TATA-box binding protein (TBP) as the endogenous control.

2.3.6 Immunoblot Analysis

Cultures were washed twice with cold phosphate-buffered saline (PBS) and lysed in RIPA buffer (10 mM Tris [pH 8.0], 140 mM NaCl, 1% Triton X-100, 1% sodium deoxycholate, and 0.1% sodium dodecyl sulfate [SDS]) containing a protease inhibitor cocktail (cOmplete Mini EDTA-free, Roche, Indianapolis, IN) for total cell lysis. Collected lysates were incubated on ice for 15 min with intermittent vortexing. Protein concentration of each lysate was determined using the Bio-Rad Protein Assay (Bio-Rad Hercules, California) using bovine serum albumin as the protein concentration standard. For immunoblot analysis, 20 μg whole-cell extracts from undifferentiated subcutaneous preadipocytes or 14-day differentiated adipocytes were separated by SDS-PAGE and then transferred to nitrocellulose membranes. The membrane was blocked with 3% bovine serum albumin (BSA) in Tris-buffered TBS with 0.05% Tween (TBST) for 1 hr. After blocking, membranes were incubated at 4°C overnight with anti-PFKFB3 antibody (ab96699, Abcam, Cambridge,

MA) in 3% BSA in TBST. After 3 washes in TBST (10 min each), membranes were incubated with horseradish peroxidase-conjugated secondary antibodies in 5% milk in TBST (1:5000) for 1 hr. The loading control was anti-β-actin conjugated to HRP (sc-47778 HRP, Santa Cruz Biotechnology, Dallas, Texas). Before developing the blots, membranes were washed three times in TBST for 10 min each. Blots were then developed according to kit directions (SuperSignal West Pico Chemiluminescent Substrate, ThermoFisher Scientific, Waltham, MA). Antibody binding was visualized with an ImageQuant LAS 4000 (GE Healthcare Life Sciences, Pittsburgh, PA).

2.3.7 Extracellular Flux Analysis

Extracellular acidification rate (ECAR) and oxygen consumption rate (OCR) were measured at 37°C using adherent cells in a microplate-based extracellular flux analyzer (XF24, Seahorse Bioscience). Forty-five minutes before the measurement, cells were washed with unbuffered seahorse medium and placed in a 37°C incubator without CO_2. The XF24 instrument measured oxygen consumption and extracellular acidification (ECAR) rates. The mixing, waiting, and measurement times used were 3, 2, and 3 min, respectively. Measurements were normalized to the amount of protein per well.

2.3.8 Metabolomics

[13C6]D-glucose was obtained from Cambridge Isotope Laboratories (Tewksbury, MA) and dissolved in glucose-free Dulbecco's Modified Eagle Medium (DMEM) (11966-025, ThermoFisher Scientific, Waltham, MA). The final concentration was 25 mM [13C6]D-glucose. Medium on 14-day differentiated adipocytes was changed to fresh, unlabeled 25 mM glucose, 3% FBS DMEM 3 hours prior to starting the experiment, after which the medium was removed and cells were washed 2 times with 3 mL of warm PBS. After thorough aspiration, 25 mM [13C6]D-glucose, 3% dialysed FBS DMEM was added.

Cells exposed to cold were incubated at room temperature in a 5% CO_2, balanced air incubator. Control warm cells were incubated at 37°C in a 5% CO_2, balanced air incubator. At designated time points, cells were washed in cold 0.85% saline and metabolites were collected with a three-phase methanol–water–chloroform extraction using water spiked with norvaline as an internal standard.

2.3.9 Statistical Analysis

Cell culture experiments were repeated three independent times, with the exception of lattice light sheet microscopy (n=2). The intracellular temperature data are expressed as the mean $\pm$ SEM. Significance was determined from a two-way ANOVA with Bonferroni's multiple comparison post hoc test. PCR and Western blotting data are expressed as the mean $\pm$ SEM, and significance was determined from the two groups by the two-tailed Student's t-test. Analyses were performed using Prism 5 by Graphpad.

2.4 Temperature Gradient Co-culture Platform

A temperature control co-culture system with a gradient was developed to expose a monolayer of adipocytes to 30°C and an opposing monolayer of adipocytes to 37°C. The gradient profile allowed the cold-induced thermogenic fat and physiologically warm fat to be in the same media. The shared culture media enabled real-time paracrine interactions between the cold-induced adipocytes and warm adipocytes to determine whether co-culture modulated thermogenic signaling.

2.4.1 Platform Design

The platform was designed as an engineered system of two peltier thermoelectric devices (TE Technology, Traverse City, MI) integrated into a cell co-culture layout. Two distinct monolayers of cells were cultured on separate 25 mm diameter round glass coverslips. Peltier elements maintained the surface of each coverslip at a different temperature. One

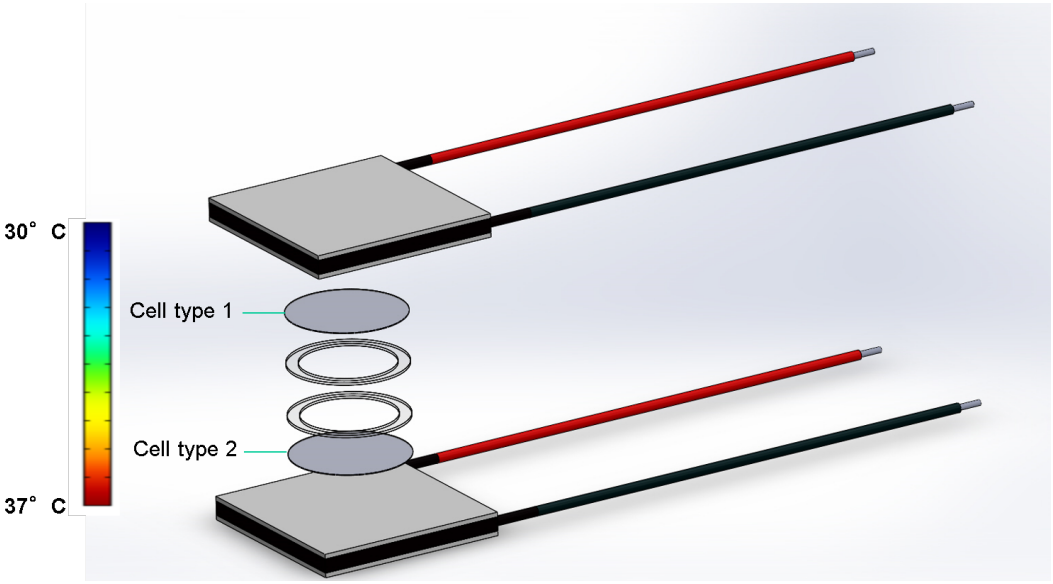

FIGURE 2.7: The co-culture platform exposes a cell monolayer to 30°C and an opposing monolayer to 37°C in shared culture media to allow paracrine interactions.

sample was exposed to 30°C while the other was exposed to 37°C (Fig. 2.7). PDMS gaskets separated the cells on the coverslips and created a shared media reservoir to allow for paracrine interactions between the cell monolayers. The thickness of the gaskets determined the distance between the 30°C and 37°C monolayers, which could be tuned to desired gap widths. A PDMS gasket was bonded to each glass coverslip using plasma surface treatment for 1 min from a handheld corona discharge device (Electro Technic Products, Chicago, IL).

The cells cultured on the coverslips were then exposed to desired temperature conditions by tightly controlling the surface temperature of each peltier with its own thermoelectric temperature controller (TC-720; TE Technology). A thermistor on the temperature-controlled side of the peltier provided feedback to the thermoelectric temperature controller to maintain the input target temperature. Two DC power supplies were used to power the system; one supply powered the temperature controllers (13.7 V) and one powered the peltier thermoelectric devices (6.7 V).

2.4.2 COMSOL Temperature Simulation

The heat transfer in the co-culture assembly between two peltiers was simulated using COMSOL. The model used $37.5°$C and $29.5°$C as the setpoints for the peltier surfaces in the warm and cold conditions, respectively. The distance between the glass coverslips, as determined by the thickness of the PDMS gaskets, was modeled as 1 mm. The material properties used in the heat transfer simulation are in Appendix .

2.4.3 Cell Culture

The glass coverslips with the PDMS gaskets bonded to the surface were autoclaved prior to cell culture. Then, 500 μl of 0.1% gelatin (porcine skin type A; Sigma-Aldrich) in E-pure water (Barnstead Thermolyne, Dubuque, IA) was added to the glass coverslip and incubated at $37°$C overnight. After excess gelatin was aspirated, human subcutaneous preadipocytes (SP-F-1, Zenbio) were seeded at a density of 200,000 cells per coverslip in 500 μl of preadipocyte growth medium (PM-1, Zenbio). Twenty-four hours after plating, the samples intended for differentiation into adipocytes were aspirated of preadipocyte and adipogenic differentiation medium (3% fetal bovine serum (FBS), 0.25 mM isobutyl-methylxanthine (IBMX), 66 μM d-biotin, 34 μM d-pantothenate, 5 μM rosiglitazone, 1 μM dexamethasone, and 200 nM human insulin in DMEM/Ham's F-12) was added. After 3 days of induction, cells were then maintained in adipocyte nutrition medium (prepared identically to adipogenic differentiation medium except it did not contain IBMX and the rosiglitazone concentration was reduced to 1 μM). Cells used in thermogenic studies were differentiated 5 days (3 days in adipogenic differentiation medium and 2 days in adipocyte nutrition medium).

2.4.4 Temperature-controlled Co-culture

For co-culture studies, two different coverslip samples were placed on top of each other with the PDMS gaskets in contact. The placement was performed while the samples were

completely immersed under DMEM supplemented with 3% FBS to prevent trapping air bubbles in the shared medium of the cell samples. The outside of the joined coverslip co-culture construct was wiped dry and placed on the surface of a peltier housed in a in a cell culture incubator specifically maintained at room temperature with standard 5% CO_2, balanced air. A second peltier was carefully placed on top of the co-culture construct to avoid shifting the PDMS-PDMS contact of the samples. The hot side of each peltier was in contact with a brass disk cooled with an ice pack to act as a heat sink for the hot sides of the powered peltiers. The temperature controllers allowed the surface of each peltier to reach its target temperature within 15 seconds. The temperature gradient was maintained for the duration of the 4 h co-culture studies.

2.4.5 Quantitative Real-time PCR

After the desired amount of temperature-controlled co-culture, the two coverslips were separated and washed twice with PBS. Total RNA was extracted with TRIzol (Invitrogen, Carlsbad, CA) according to the manufacturer's instructions. The relative expression of each gene was determined with real-time PCR. Briefly, cDNA was synthesized from total RNA using the High-Capacity cDNA Reverse Transcription Kit (Applied Biosystems, Carlsbad, CA). Real-time quantitative PCR was carried out on an Applied Biosystems ViiA7 instrument in 10 μl reactions containing 6.25 μl of FastStart Universal SYBR Green master mix. Relative gene expression of target gene mRNA was calculated using beta-2-microglobulin (B2M) as the endogenous control.

CHAPTER 3. RESULTS

Portions of this content have previously been published in Rexius-Hall, M. L., Mauleon, G., Malik, A.B., Rehman, J., and Eddington, D.T. (2014) Microfluidic platform generates oxygen landscapes for localized hypoxic activation, Lab Chip. 14(24):4688-95 and Rexius-Hall, M.L., Rehman, J., and Eddington, D.T. (2017) A microfluidic oxygen gradient demonstrates differential activation of the hypoxia-regulated transcription factors HIF-1α and HIF-2α, Integr. Biol. Advance Article DOI 10.1039/C7IB00099E.

3.1 Large-area Oxygen Landscapes

Prototypes of large-area oxygen landscape designs (see Fig. 2.1) were fabricated to characterize the surface oxygen profiles. The measured surface percent oxygen was plotted as a function of position (Fig. 3.1), and results closely approximated the idealized profiles for square wave, oscillating, and linear oxygen landscapes. The binary dual condition prototype also demonstrated a profile close to the idealized profile (shown in Fig. 2.1A). The oxygen validation plot and expanded function of the dual condition landscape device is the focus of Section 3.1.1.

3.1.1 Dual Condition Oxygen Landscape

The device was used in three configurations: (1) hypoxia (both channel networks 95% N_2/5% CO_2), (2) normoxia (both channel networks air/5% CO_2), or (3) dual condition (one network 95% N_2/5% CO_2, one network air/5% CO_2). A fluorescent PtOEPK thin film sensor placed on top of the PDMS membrane characterized the oxygen profiles (Fig. 3.2A). The surface percent oxygen was calculated from fluorescent intensities by solving the Stern-Volmer equation (see Section 2.1.5). Results were plotted as a function of position in the x-direction (Fig. 3.2B). The slope of the oxygen gradient between the two adjacent microfluidic networks was 11.4%/mm, which equates to a 1% change in oxygen tension every 87.7 μm. We measured the dynamics of inducing hypoxic conditions in the

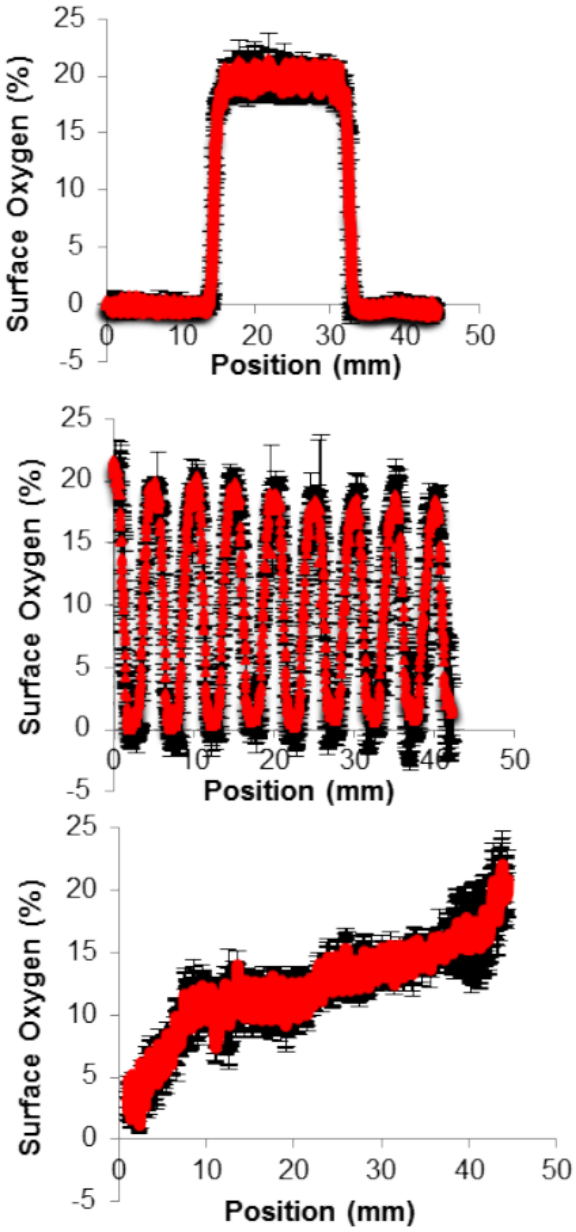

FIGURE 3.1: The microfluidic network design can generate a variety of oxygen landscapes. The surface oxygen profile as a function of the position is shown for the square wave (top), oscillating (middle), and linear (bottom) oxygen landscape.

device and plotted the percent oxygen at the surface of the membrane as a function of time (Fig. 3.2C). Our experimental data demonstrated that the time required to achieve steady-state diffusion of oxygen across a 100 μm PDMS membrane was approximately 20 seconds.

Constant perfusion of 95%N_2/5%CO_2 in the underlying microfluidic channels maintains severe hypoxic conditions for cells in the hypoxic region of the device when operated in the dual condition configuration and severe hypoxic conditions for the entire monolayer of cells when operated in the homogenous hypoxia configuration. The dual condition configuration maintained inlet gas oxygen levels within 100 μm of the membrane, making it ideally suited for studying cells or thin tissue slices (Fig. 3.2D). In hypoxia, we show that the dissolved oxygen increases rapidly as the distance from the membrane increases. This is caused by the gas exchange that occurs with the surrounding controlled gas conditions in the incubator (5% CO_2, balanced air at 37°C). While our oxygen measurements do not give us the resolution to precisely determine the hypoxic conditions experienced by the cells on the membrane, we estimate that they are $\leq$ 0.5% oxygen. The device was used to investigate a binary profile from 0% to 21% oxygen, but any binary condition could be studied by injecting different gases into the networks.

3.1.2 Hypoxic Response of Human Microvascular Endothelial Cells

We first tested the biological responsiveness of human cells in the platform. Hypoxia-induced alterations in gene expression rely on the transcriptional activity of the HIF family of transcriptional factors. Following low oxygen levels, HIF α-subunits (HIF-1α, HIF-2α, and HIF-3α) undergo nuclear translocation, heterodimerization with the β-subunit, and DNA binding to initiate transcription of target genes. Human lung microvascular endothelial cells (HLMVECs) cultured in the platform confirmed nuclear translocation of HIF-1α in the hypoxic region (Fig. 3.3A) as compared to the normoxic region (Fig. 3.3B). HLMVECs fixed in the device and stained for HIF-1α after 12 h of hypoxic oxygen

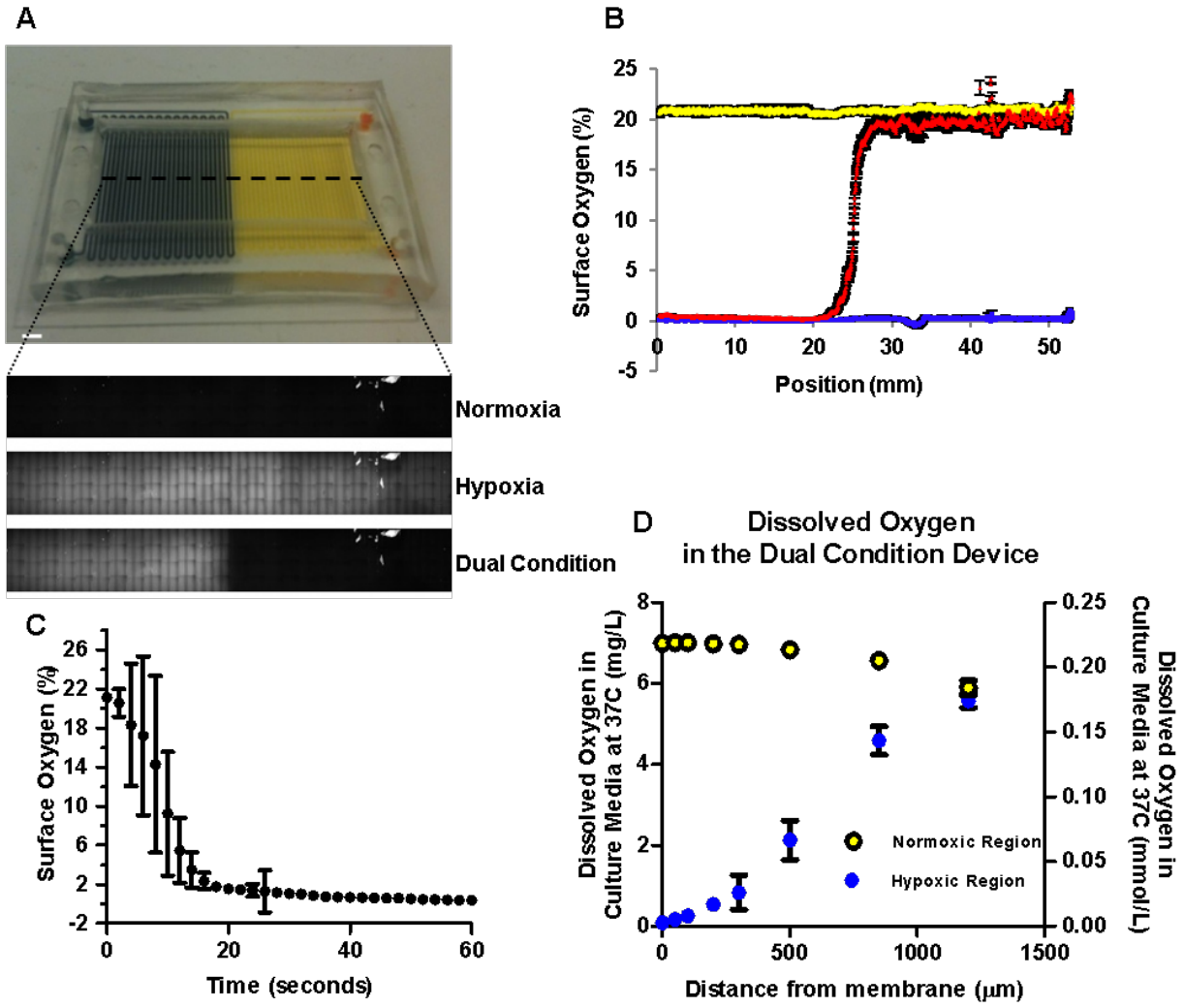

FIGURE 3.2: Sensor measurements characterized the dual condition oxygen profile. (A) Two dyes (blue and yellow) injected into the adjacent serpentine microchannel networks clearly delineate the boundaries. Scale bar: 4 mm. Fluorescent image scans were performed across the width of the culture space in three configurations: normoxia, hypoxia, and dual condition. (B) The surface percent oxygen is shown as a function of position with plots of normoxia (yellow), hypoxia (blue), and the dual condition (red) configuration (mean ± SEM, n=3). (C) The surface oxygen percent as a function of time demonstrates the rapid equilibrium of hypoxic induction in the device (mean ± SD, n=3). (D) In the open-well format, the concentration of dissolved oxygen equilibrates as the distance from the PDMS membrane increases due to exchange with the controlled 5% CO_2, balanced air and 37°C conditions inside the cell culture incubator (mean ± SD, n=3).

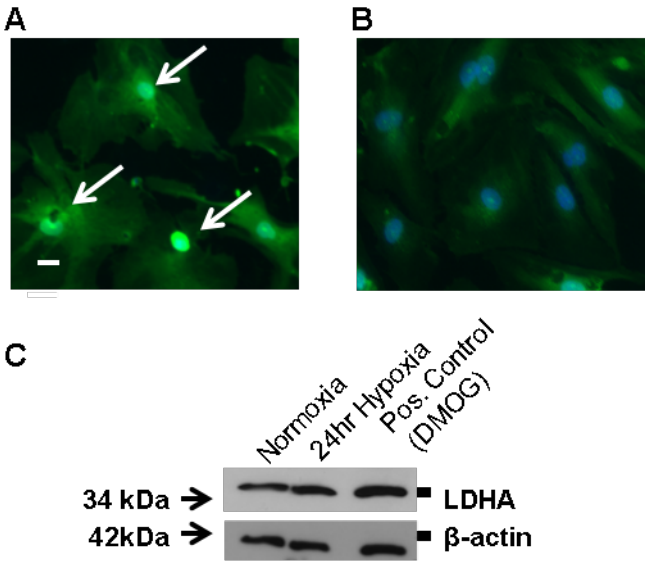

FIGURE 3.3: Cells respond to oxygen modulation in the platform. (A–B) In-device immunofluorescent staining shows HLMVECs after 12 h of oxygen modulation. HLMVECs were stained for HIF-1α (green), and nuclei (blue) were counterstained with Hoechst. Punctuated green nuclear staining (indicated by white arrows) shows translocation of HIF-1α to the nucleus in hypoxia (A) as compared to normoxia (B). Scale bar: 1 μm. (C) A representative Western blot demonstrates LDHA protein level in HLMVECS increased after 24 hr of hypoxia in the device compared to the normoxic control device. DMOG, a PHD inhibitor, served as a positive control. Beta-actin is shown as the loading control.

modulation had punctuated green fluorescent staining in the nuclei. As expected, HIF-1α activation in the device increased protein expression of a downstream target gene, lactate dehydrogenase A (LDHA), after 24 h of oxygen modulation (Fig. 3.3C). Dimethyloxalylglycine (DMOG) was used as a positive control for HIF activation because it is a prolyl hydroxylase domain (PHD) enzyme inhibitor. Hydroxylation of HIF-1α by a PHD will target the subunit for proteasomal degradation. Therefore, inhibition of PHDs stabilized HIF-1α protein (see Section 1.1.2). The protein β-actin served as the loading control.

3.1.3 Metabolic Specificity of Bone Marrow-derived Mesenchymal Stem Cells

After verifying HIF-1α induction in mature endothelial cells, we studied stem cell function in the oxygen landscape. Human mesenchymal stem cells (MSCs) *in vivo* are located

in the heterogeneous oxygen microenvironment of the bone marrow (BM) to support hematopoietic stem cells (HSCs) by secreting factors for their maintenance [168]. However, it is not understood if an oxygen landscape confers metabolic specificity underlying the dynamic interplay between MSCs and HSCs in the heterogeneous BM microenvironment. The glucose transporter Glut1, LDHA, and four known isozymes of pyruvate dehydrogenase kinase (PDK1, PDK2, PDK3, and PDK4) are genes downstream of HIF-1α that convert metabolic processes from oxidative phosphorylation to glycolysis under hypoxic conditions. Quantitative PCR in MSCs was used to investigate metabolic programs regulated by the oxygen landscape. Homogeneous hypoxia and dual condition hypoxia corresponded with upregulation of the relative gene expression of LDHA (Fig. 3.4A), indicating an enhanced glycolytic metabolic state during hypoxia compared to normoxia (Fig. 3.4B). Relative expression of Glut1, PDK1, and PDK3 were also upregulated in homogeneous hypoxia and dual condition hypoxia (Fig. 3.4C). PDK3 expression was more sensitive to the landscape than PDK1, and relative expression of PDK4 was too low for analysis (data not shown). The relative gene expression of PDK2 was insensitive to oxygen tension. Increased gene expression in hypoxia has been reported for PDK4 but not for PDK2 in long-term HSCs (LT-HSCs) [169]. Our results indicate not only differential regulation of PDKs dependent on oxygen tension in MSCs but also regulation of regional metabolic profiles in cells by the oxygen landscape itself.

3.1.4 Differential Expression of Genes in the Oxygen Landscape

The oxygen landscape was demonstrated to differentially regulate gene expression as compared to homogeneous controls in a human lung microvascular endothelial cells (HLMVECs).

6-Phosphofructo-2-Kinase/Fructose-2,6-Biphosphatase 3 (PFKFB3) is a glycolytic activator; PFKFB3 converts fructose-6-phosphate to fructose-2,6-bisP (F2,6BP), and F2,6BP is an allosteric activator of 6-phosphofructokinase-1 (PFK-1), stimulating a rate-limiting

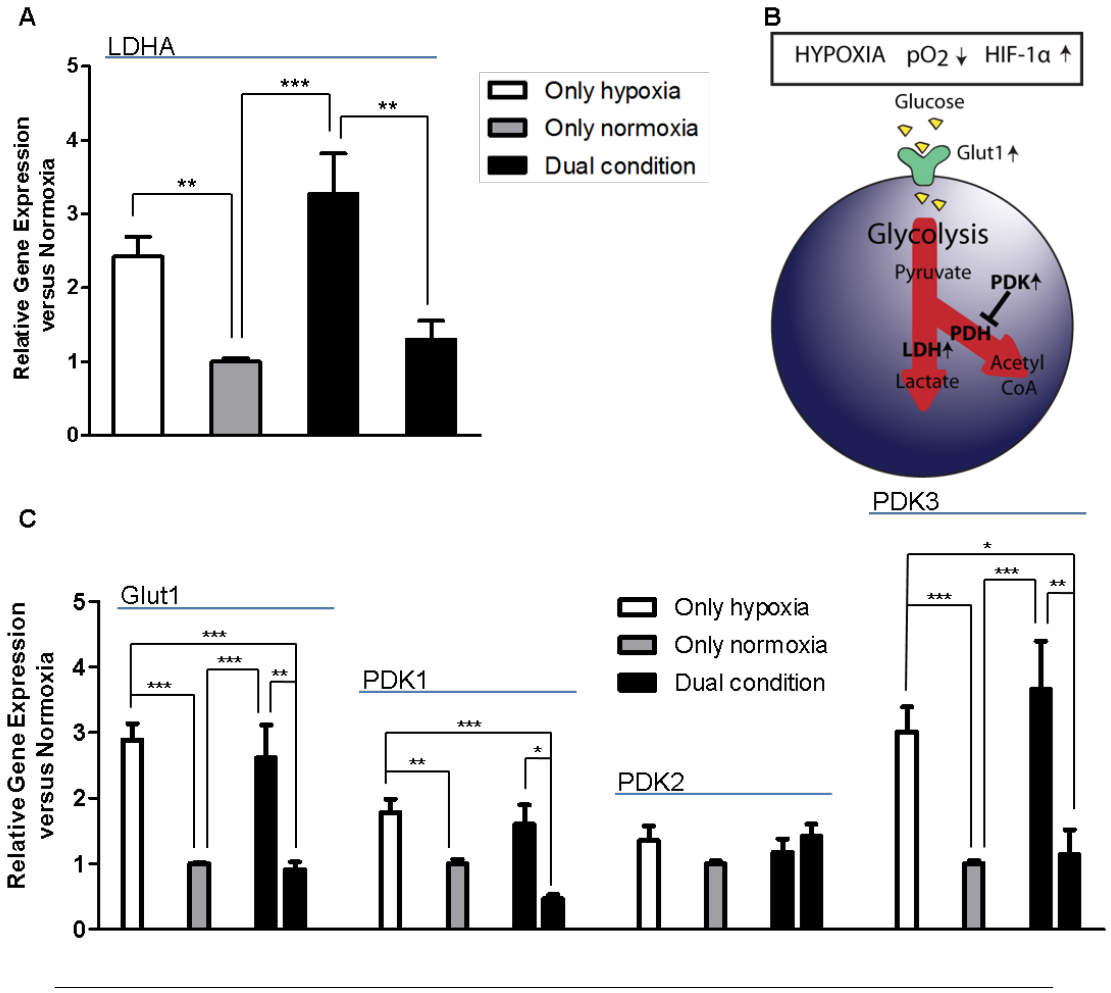

FIGURE 3.4: The oxygen landscape regulates regional metabolic profiles in bone marrow-derived human mesenchymal stem cells. (A) Quantitative PCR indicates LDHA gene expression is upregulated in the hypoxic region of the oxygen landscape (black, left) as compared to the normoxic region (black, right) and retains the metabolic character of homogeneous hypoxic controls (white). (B) The schematic represents the effect of hypoxia on energy metabolism in a cell. (C) Gene expression of Glut1 and the PDK isozymes in homogeneous control devices are compared to the dual condition landscape with the hypoxic region (black, left) and normoxic region (black, right). Statistical comparisons were performed with ANOVA and Tukey's multiple comparison post-test (mean $\pm$ SEM, n=4, * $p < 0.05$, ** $p < 0.01$, and *** $p < 0.001$).

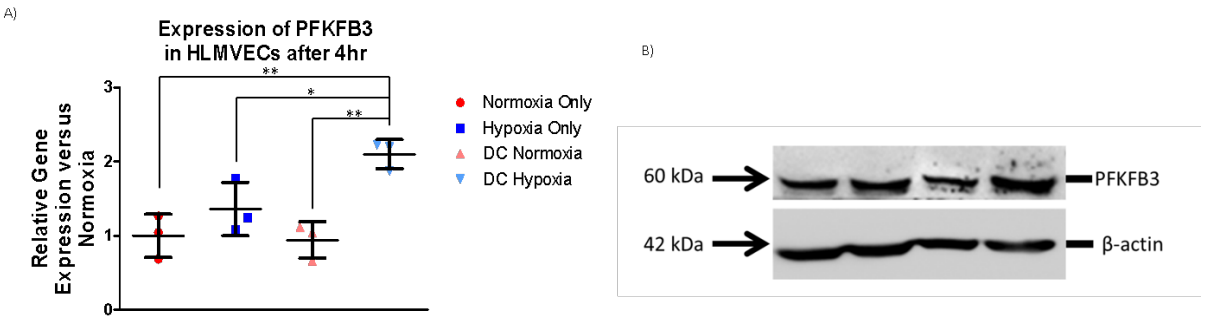

FIGURE 3.5: Dual condition hypoxia enhances PFKFB3 compared to homogeneous hypoxia. (A) PFKFB3 mRNA and (B) PFKFB3 protein expression is upregulated in hypoxic cells with nearby normoxic cells in the dual condition oxygen landscape after 24 h. Statistical comparisons were performed with ANOVA and Bonferroni's multiple comparison post-test (mean ± SEM, n=3, * $p < 0.05$, and ** $p < 0.01$).

enzyme in glycolysis. PFKFB3 has previously been shown to play a critical role in endothelial cells by regulating vascular sprouting, migration of endothelial tip cells, proliferation of stalk cells, lamellipodia formation, cell motility, and migration velocity [170]. In the dual condition oxygen landscape platform, the dual condition hypoxia cells had the highest mRNA level of PFKFB3 as compared to dual condition normoxia or either of the homogeneous controls after 4 hr (Fig. 3.5A). After 24 h of oxygen modulation, the dual condition hypoxia cells were also found to have the highest amount of PFKFB3 protein (Fig. 3.5B).

3.2 Stable Linear Oxygen Gradients

The large-area, linear profile required the inputs of 5 different compressed gas tanks due to its size (as discussed in Section 2.1.2). By downsizing the device and simplifying the design to two gas supply channels separated by a desired width, stable linear oxygen gradients were developed.

3.2.1 Linear Gradient Profile

Our microengineered device to generate a stable, linear oxygen gradient was used to study HIF activation in a monolayer of human endothelial cells exposed to a range of oxygenation from ambient 21% to 0% (see Fig. 2.5), thus better mimicking the physiologic oxygen microenvironment *in vivo* where gradients of oxygen exist in tissues and within the vasculature. The linear gradient allowed us to precisely assign a known level of oxygenation to which cells are exposed with a specific position. The linear gradient also allowed equal contribution of all the oxygen levels within the range of established oxygenation for the spatial profile. We first determined the oxygen gradient in the device as a function of the position along the x-axis (Fig. 3.6A-D). Devices with a diffusion gap of 3 mm (Fig. 3.6A), 5 mm (Fig. 3.6C), and 7 mm (Fig. 3.6B) were fully characterized with gradients from 21% to 0% O_2 over a 4-hour duration of oxygen modulation. The 5 mm diffusion gap device was further characterized in the range from 7.5% to 0% O_2 by substituting a 5% CO_2, 7.5% O_2, and balanced nitrogen tank for perfusion into the first microchannel (Fig. 3.6D) to demonstrate the usage of the device in a narrower range of oxygenation. The linear gradient developed over time, and by 2 hours of oxygen modulation, the established gradients were near equilibrium for all tested diffusion gaps. The slope of the gradient could be tuned by altering the width of the diffusion gap (Fig. 3.6E). The slope did not vary linearly with the diffusion gap width (Fig. 3.6F). However, a reduction in the diffusion gap resulted in a steepening of the oxygen gradient. The slopes characterized from the 21% to 0% range of the 3 mm, 5 mm, and 7 mm gaps were -5.5% $\pm$ 0.3%, -3.4% $\pm$ 0.1%, and -2.7% $\pm$ 0.1% O_2/mm, respectively.

3.2.2 Linear Gradient in the Presence of Cells

To determine whether the oxygen gradient was affected by cells cultured on the membrane, oxygen levels were determined in the presence of the cell monolayer to assess

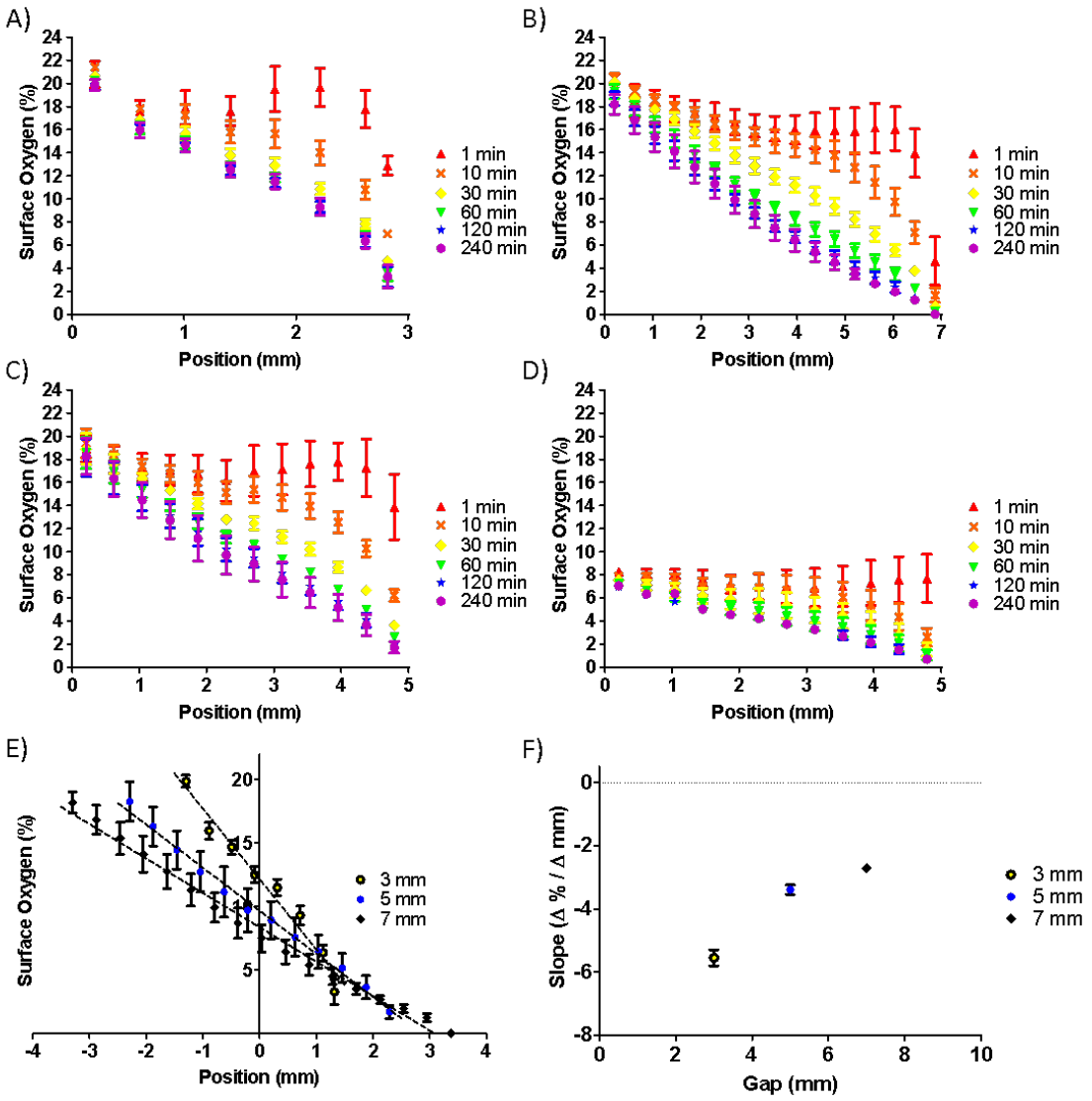

FIGURE 3.6: Sensor measurements characterized the oxygen gradient. (A-C) The surface percent oxygen over a 4 h duration is shown as a function of position with microchannel inputs of 21% O_2 and 0% O_2 for a 3 mm, 7 mm, and 5 mm diffusion gap, respectively. (D) Microchannel inputs of 7.5% O_2 and 0% O_2 for a 5 mm diffusion gap demonstrates that choice of inputs determines the range of the linear gradient. (E) The 21%-0% range for 3 mm, 5 mm, and 7 mm diffusion gaps are compared, demonstrating that the slope is tunable by altering the diffusion gap parameter. The middle of each diffusion gap is centered at the 0 mm position. (F) The slope is plotted as a function of the size of the diffusion gap.

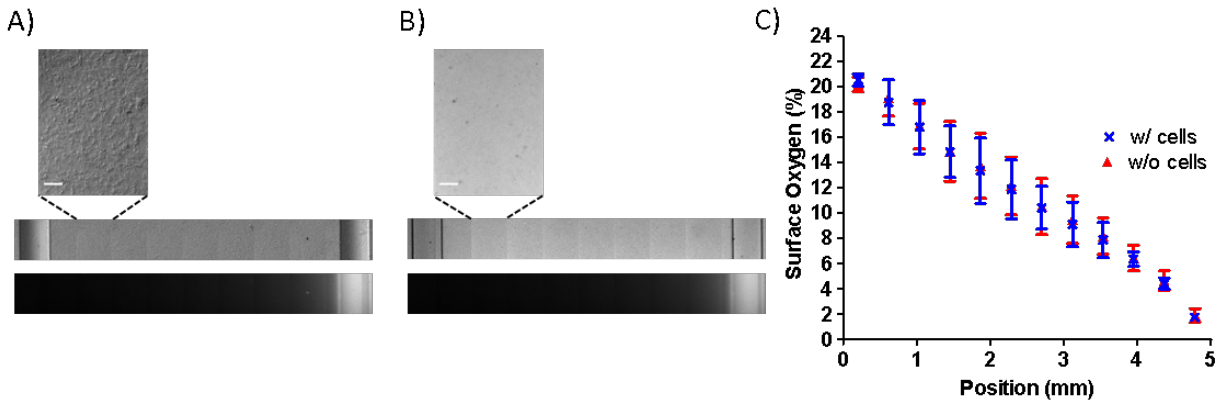

FIGURE 3.7: Cells cultured on the membrane do not affect the oxygen gradient to which the cells are exposed. Tiled scans of brightfield images of the membrane (top) and fluorescent images of the PtEOPK signal (bottom) demonstrate the presence of the oxygen gradient (A) with cells and (B) without cells. Scale bar: 100 μm. (C) The surface percent oxygen level as a function of position does not vary between the cell-occupied and cell-vacant condition.

whether the linear gradient was preserved. Cells were cultured directly on a PDMS membrane impregnated with PtOEPK. Tiled scans of the PtOEPK signal on the membrane were acquired after 4 h of oxygen modulation with cells (Fig. 3.7A) and without cells (Fig. 3.7B) on the membrane of the device. The post-Stern–Volmer analysis demonstrated that the spatial gradient was not affected by the presence of cells (Fig. 3.7C). As expected for such a device with constant perfusion of gas at constant, high pressure (5 psi) through the microfluidic channels, the cells do not consume oxygen at a rate fast enough to significantly alter the surface oxygen profile to which the cells were exposed. The slope of the gradient with cells and without cells was equal (-3.8 $\pm$ 0.2% O_2/mm).

3.2.3 HIF-1α Activation

We next evaluated the activation of HIF-1α and HIF-2α in human endothelial cells within the oxygen gradient. The 5 mm gap device was used for all subsequent cell studies. D3 endothelial cells were cultured in the device until approximately 80% confluency. The

cells were then subjected to 8 h of a linear oxygen gradient. Immunofluorescence imaging of HIF-1α in the spatial gradient clearly showed nuclear translocation of HIF-1α in the cells cultured directly above the device's hypoxic channel (Fig. 3.8D) and homogeneous hypoxic control devices (Fig. 3.8B) as compared to cells cultured above the normoxic channel (Fig. 3.8C) and homogeneous normoxic control devices (Fig. 3.8A). A tiled image scan of the entire gradient allowed us to determine the nuclear to cytosolic ratio for each field of view and these were plotted as the x-coordinate of the position at the center of the field of view. The nuclear to cytosolic ratios of cells within the oxygen gradient provided a measure of HIF-1α activation because active HIFs are translocated to the nucleus and were compared to the ratios found in cells exposed to homogeneous oxygen levels. The nuclear to cytosolic ratio of a homogeneous normoxic control device was normalized to 1. Nuclear to cytosolic ratio quantification of HIF-1α showed that the two closest fields of view to the hypoxic channel were statistically significantly different from the homogeneous normoxic control (Fig. 3.8E). Oxygen levels in the linear gradient below 2.5% resulted in statistically higher HIF activation. Importantly, all the positions with O_2 levels higher than 2.5% (x-axis coordinate lower than 4.8 mm) did not show any significant HIF-1α activation. Importantly, the degree of HIF-1α activation at the 0-1% level approximated that of cells placed in homogeneous hypoxia (blue range, Fig 3.8E).

3.2.4 HIF-2α Activation

In contrast to the narrowly confined range of HIF-1α activation at the extremely low O_2 levels (0-2.5%), HIF-2α activation was seen throughout the entire spatial gradient. Even cells exposed to normoxia (by diffusion of 5% CO_2, balanced air and cultured directly above the normoxic supply channel in the gradient device) had observable HIF-2α activation (Fig. 3.9C) when compared to cells cultured in homogeneous normoxic conditions (Fig. 3.9A). This suggests that normoxia within an oxygen gradient elicits HIF-2α activation whereas homogeneous normoxia does not. Quantification of images from a tiled

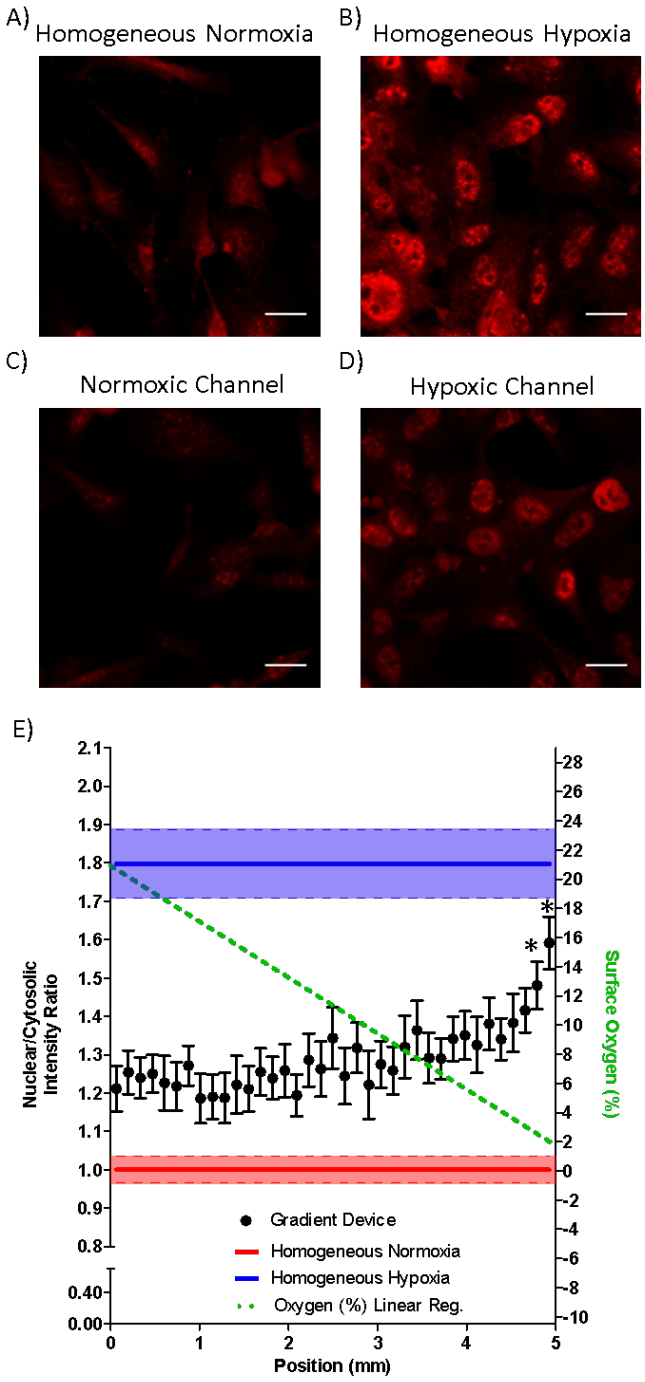

FIGURE 3.8: HIF-1α activation in endothelial cells occurs at low oxygen levels within a linear oxygen gradient. (A-B) Panels of HIF-1α immunofluorescent staining for normoxic and hypoxic homogeneous control devices. (C-D) HIF-1α immunofluorescent staining in the oxygen gradient device of cells directly above the normoxic gas supply microchannel and hypoxic gas supply microchannel, respectively. Scale bar: 20 μm. (E) Quantification of the nuclear to cytosolic ratio as a function of the position in the oxygen gradient. * $p < 0.05$ as compared to homogeneous normoxia.

scan of the gradient demonstrated widespread HIF-2α activation throughout the gradient when compared to cells exposed to homogeneous normoxia (Figure 3.9E).

3.3 Adipocyte Cold Exposure

3.4 Characterization of Adipogenic Differentiation

After 14 days of differentiation, adipocytes showed robust accumulation of lipid droplets as indicated by Oil Red O staining (Fig. 3.10A). The increased mRNA expression levels of the adipocyte-specific protein hormone adiponectin (AdipoQ) and fatty acid binding protein 4 (FABP4, also known as aP2) further confirmed the adipogenic differentiation (Fig. 3.10B). The adipogenic differentiation was also shown to induce the expression of the key thermogenic gene UCP1 (Fig. 3.10C).

3.4.1 Intracellular Temperature Increases in Adipocytes Exposed to Cold

A cell-permeable fluorescent polymer for ratiometric sensing of intracellular temperature was synthesized as previously described [160], and the polymer (indicated as thermometer 3 by Uchiyama *et al.*) was introduced into preadipocytes and differentiated adipocytes. To demonstrate cold-induced thermogenesis in adipocytes, the relationship between the environmental temperature and intracellular temperature was assessed in cells containing the thermoprobe under different temperature conditions (Fig. 3.11A-C). The media temperature was monitored throughout the course of the imaging during an environmental temperature decrease condition (blue) and steady, physiologic temperature control condition (red) (Fig. 3.11D). The physiologic temperature control condition was maintained at a constant 32.5°C while the temperature decline condition decreased from 33.3°C to 24.7°C over the duration of the study. Adipocytes exposed to the environmental temperature decline demonstrated increased intracellular temperature (Fig. 3.11A) while preadipocytes observed in the same decline in environmental temperature

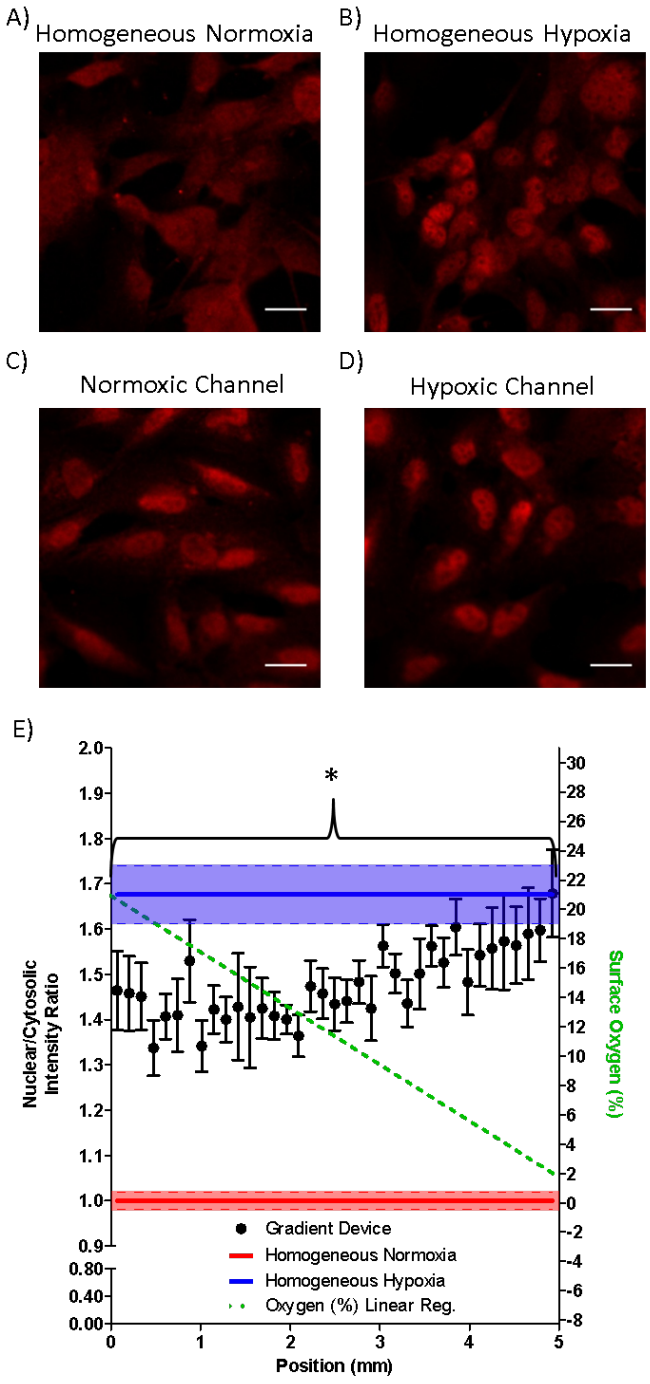

FIGURE 3.9: HIF-2α is activated throughout the entire linear gradient. (A-B) Panels of HIF-2α immunofluorescent staining for normoxic and hypoxic homogeneous control devices. (C-D) HIF-2α immunofluorescent staining in the oxygen gradient device of cells directly above the normoxic gas supply microchannel and hypoxic gas supply microchannel, respectively. Scale bar: 20 μm. (E) Quantification of the nuclear to cytosolic ratio as a function of the position in the oxygen gradient. * $p < 0.05$ as compared to homogeneous normoxia.

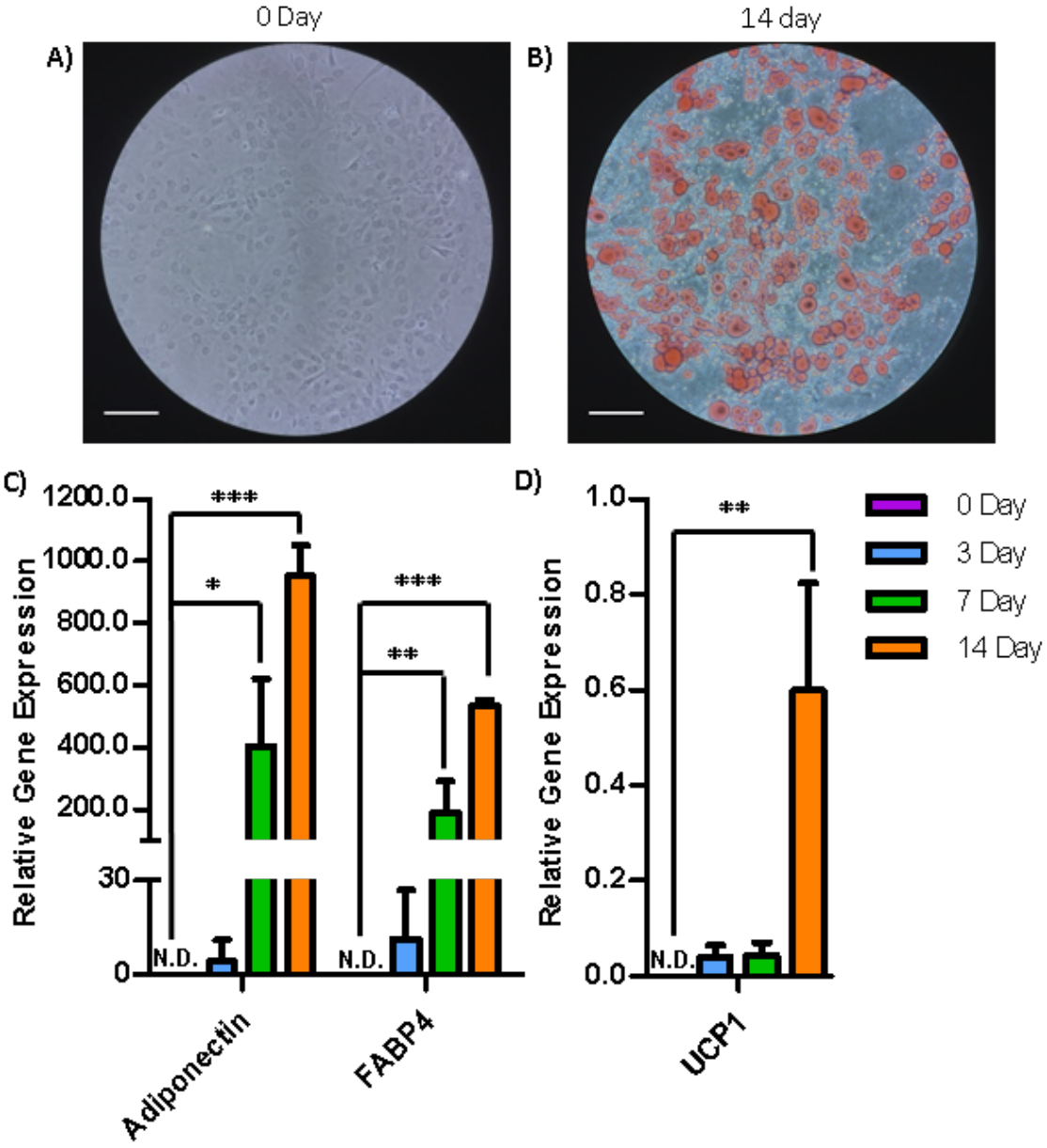

FIGURE 3.10: Subcutaneous preadipocytes underwent adipogenic differentiation. Oil Red O staining confirms accumulation of lipid droplets in (B) 14-day differentiated adipocytes compared to (A) undifferentiated preadipocytes. (C) Differentiation markers adiponectin and FABP4 were highly induced after 14 days. (D) RT-PCR data showed increased expression of UCP1 following adipogenic differentiation (n=3 for each group). * $p < 0.05$, ** $p < 0.01$, and *** $p < 0.001$.

showed a decrease in intracellular temperature (Fig. 3.11C). A change in the intracellular temperature was not observed in adipocytes in the physiologic temperature control condition (Fig. 3.11B). Normalized quantification of the thermoprobe ratio over time in cold-exposed adipocytes, cold-exposed preadipocytes, and physiologic temperature control adipocytes demonstrated significant intracellular temperature increase in the cold-exposed adipocyte condition 50 min after initiating the environmental temperature decline (Fig. 3.11E).

Lattice light sheet microscopy (LLSM) of the thermoprobe-containing adipocytes transfected with a mitochondrial HaloTag (Mito-HaloTag) and labeled with a fluorescent dye (Janelia Fluor 646) gave high-resolution mitochondrial mapping (Fig. 3.12A) and intracellular temperature mapping (Fig. 3.12B). Results showed the hottest regions during cold exposure correlated well with the location of the mitochondria. Therefore, local temperature near the mitochondria is higher than the temperature of the rest of the space in the cytosol, demonstrating heat-generating mitochondrial uncoupling in thermogenic adipocytes. Sectional views of the 3D imaging indicated that intracellular temperature varied with local position (Fig. 3.12C).

3.4.2 Adipogenic Differentiation Enhances Glycolysis

To determine alterations in glycolysis after adipogenic differentiation, the relative expression of glycolytic genes was determined. The genes in the glycolytic panel increased after 14 days with the exception of Glut1 and PDK3 (Fig. 3.13A). The role of the genes, including enzymes at glycolytic steps in metabolism, are summarized in the schematic (Fig. 3.13B). The expression of the allosteric activator of glycolysis PFKFB3 was induced ≈5- fold during differentiation (Fig. 3.13C), while the mRNA levels of the isozymes PFKFB1, PFKFB2, and PFKFB4 did not increase (n=3).

Extracellular acidification rate (ECAR), a surrogate measure of glycolytic activity, increased after 14 days of differentiation as compared to undifferentiated preadipocytes

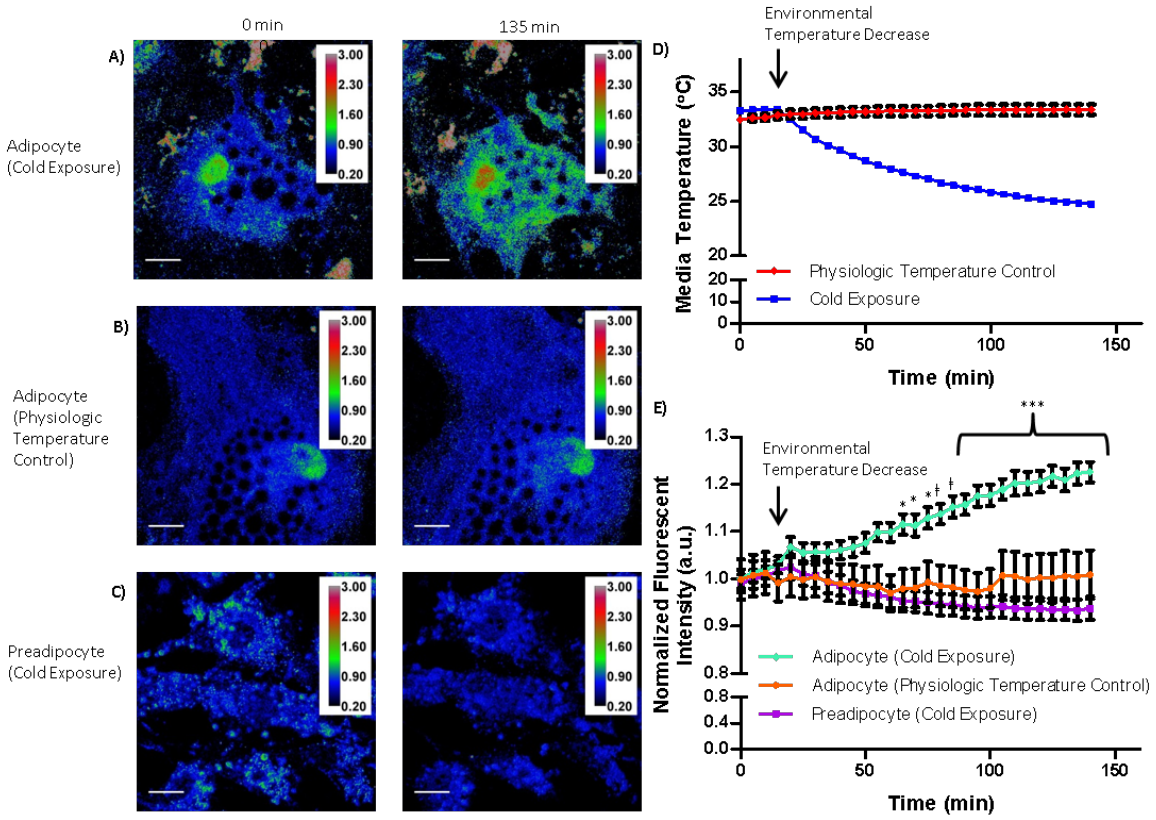

FIGURE 3.11: A fluorescent thermoprobe demonstrates adipocyte thermogenesis during environmental temperature decline. Representative images of the ratiometric fluorescent intracellular temperature probe are shown over time for (A) an adipocyte exposed to cold, (B) a control adipocyte maintained at constant physiologic temperature, and (C) preadipocytes exposed to environmental temperature decline. Scale bar: 20 μm. (D) The cell culture media temperature was recorded in the cold exposure condition (blue) and physiologic temperature control condition (red). (E) Ratiometric fluorescent intracellular temperature probe measurements were normalized in adipocytes exposed to cold (green), control adipocytes maintained at constant physiologic temperature (orange), and preadipocytes exposed to cold (purple) (n=3). * $p < 0.05$, ‡ $p < 0.01$, and *** $p < 0.001$.

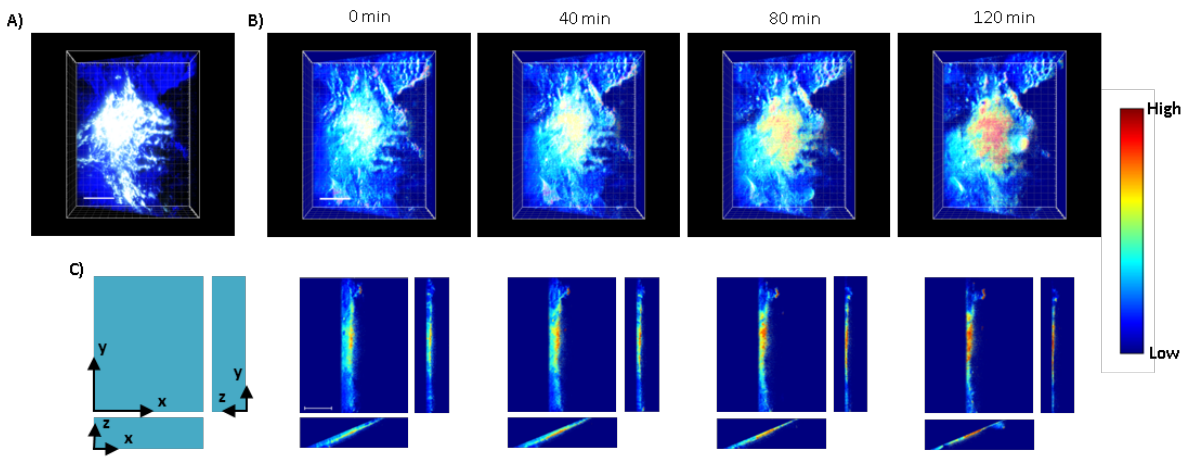

FIGURE 3.12: (A) Lattice light sheet microscopy (LLSM) shows a thermoprobe-containing adipocyte (blue) and the mitochondria (white). Scale bar: 20 μm. (B) LLSM imaging demonstrates the highest intracellular temperature regions during cold exposure map to the location of the mitochondria. Scale bar: 20 μm. (C) Sectional views of the three different planes for 3D-viewing map the thermoprobe measurements as a function of the position within the cell interior.

(Fig. 3.14A). Figure 3.14B shows ECAR levels during the glycolysis stress test. The addition of glucose supplied the substrate for glycolysis, and the difference in the ECAR before and after glucose is a measure of the glycolytic rate. The addition of oligomycin inhibited ATP synthase and was used to indicate the glycolytic reserve capacity of the cells. Thermogenic adipocytes are expected to have uncoupled mitochondria that already short-circuit ATP synthase, so it would be expected that oligomycin would not have an effect on ECAR. However, undifferentiated preadipocytes and early-differentiating adipocytes also do not respond to oligomycin, demonstrating that preadipocytes and differentiating adipocytes do not have a glycolytic reserve. As expected, 2-DG treatment drastically decreased ECAR as it inhibited further glycolysis. After differentiation, adipocytes exhibited higher oxygen consumption (Fig. 3.14C), suggesting that differentiation increased not only glycolysis but also oxidative phosphorylation.

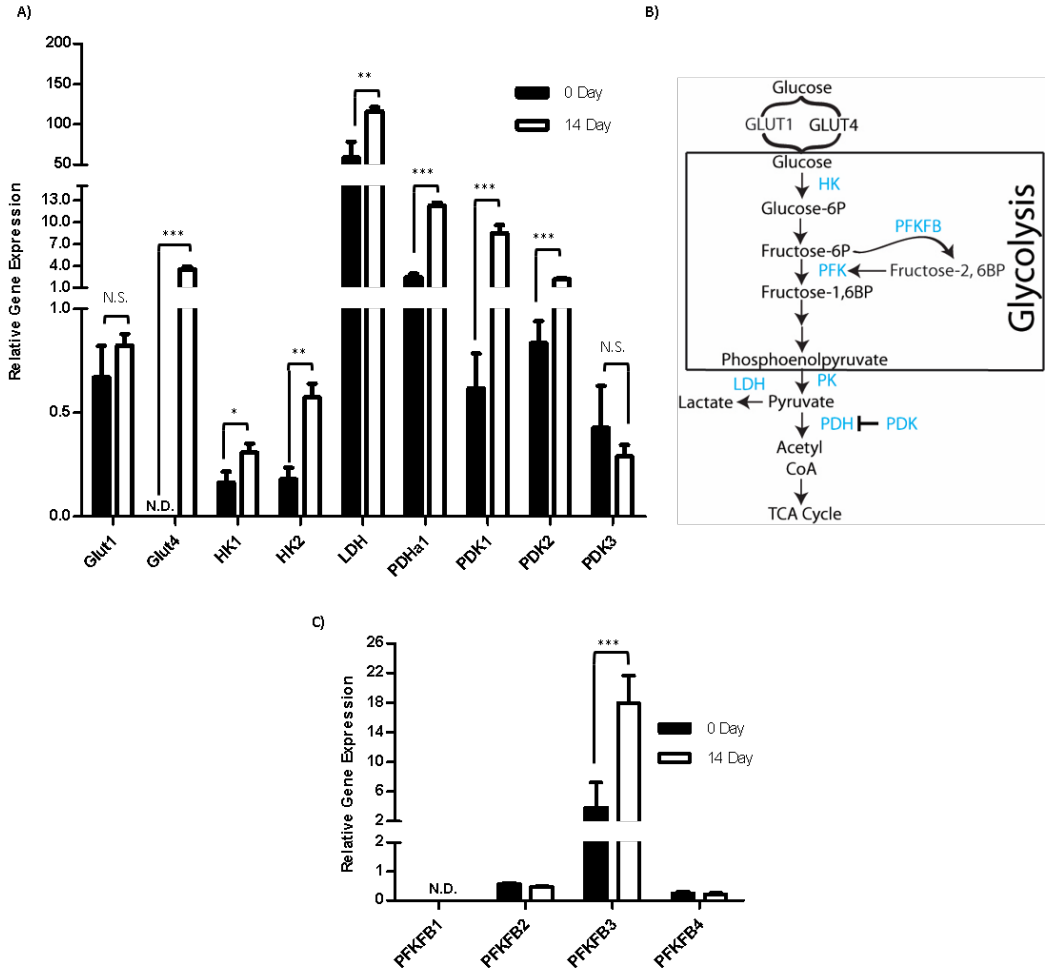

FIGURE 3.13: Adipogenic differentiation upregulates glycolytic genes. (A) Glycolytic genes were significantly induced after 14 days of differentiation (n=3). (B) Schematic representation shows the genes involved at different metabolic steps in gylcolysis. (C) The expression of the allosteric activator of glycolysis PFKFB3 is induced during differentiation as compared to the isoenzymes PFKFB1, PFKFB2, and PFKFB4 (n=3). * $p < 0.05$, ** $p < 0.01$, and *** $p < 0.001$.

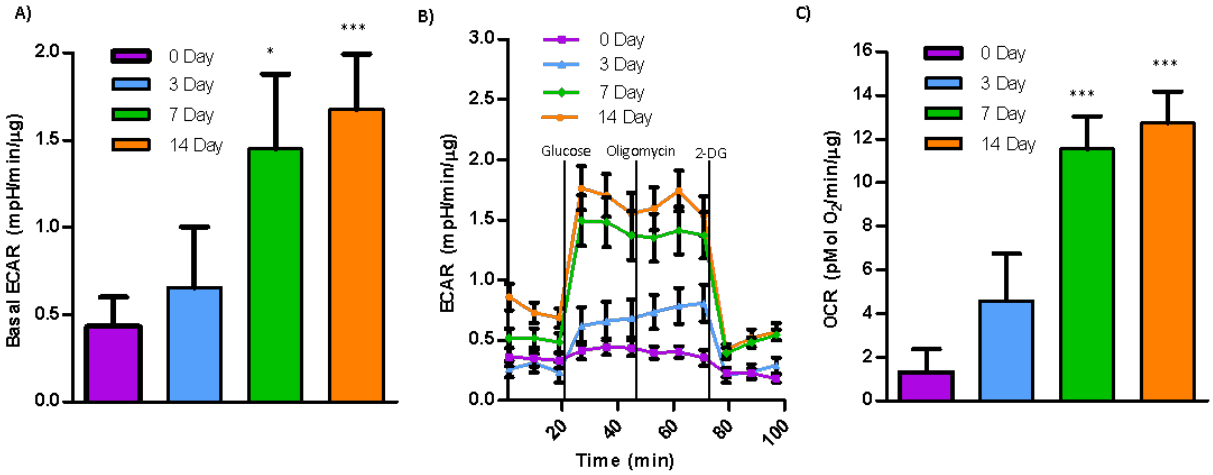

FIGURE 3.14: Adipogenic differentiation enhances glycolysis. (A) ECAR was measured during adipogenic differentiation (n=3). (B) A trace of the average ECAR levels during the glycolysis stress test is shown for different days during differentiation. (C) OCR levels were measured during adipogenic differentiation (n=3). * $p < 0.05$ and *** $p < 0.001$.

3.4.3 Cold Exposure Increases Glucose Uptake and Metabolic Flux

Upon cold exposure, glucose uptake was significantly enhanced (Fig. 3.15) as reported by others [92, 171, 172]. UCP1-dependent thermogenesis necessitates compensation for the loss of ATP production via ATP synthase due to the collapse of the proton gradient, and the cytosolic ATP production needed for compensation requires glucose. In addition to cytosolic ATP production, the anaplerotic reactions for fatty acid oxidation and lipid synthesis also require glucose. An increase in glycolysis may explain the increase in the ATP:ADP ratio over time during cold exposure (Fig. 3.16). Measurements from a ratiometric, fluorescent ATP/ADP biosensor were acquired for a basal warm period followed by an environmental temperature decline in adipocytes. The ATP:ADP ratio was shown to increase following the environmental temperature decline but not during the initial basal warm period. Ratiometric changes observed with high glucose (100 mM), to increase ATP synthesis, followed by 2-DG (100 mM), to prevent further glycolysis and decrease ATP, validated the responsiveness of the biosensor.

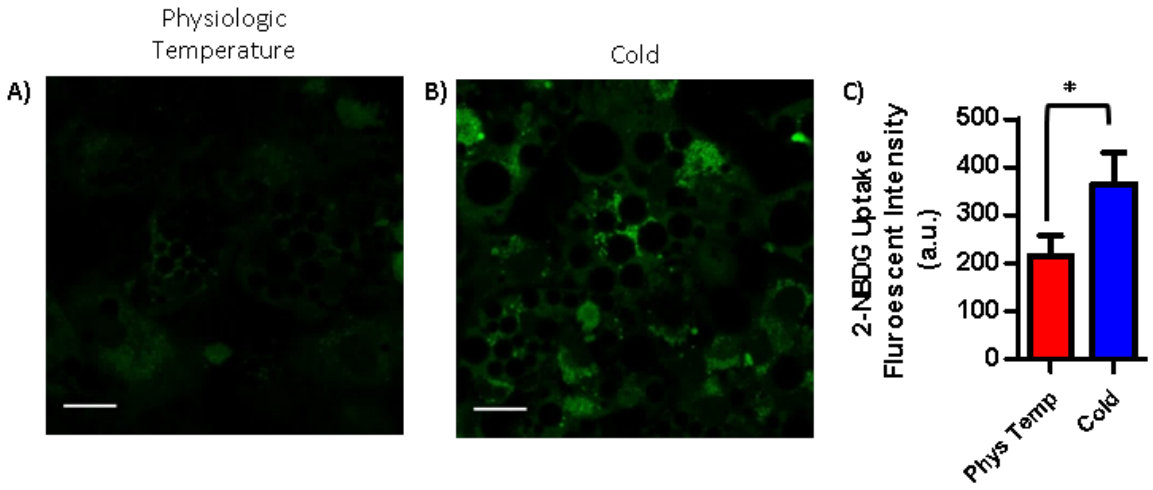

FIGURE 3.15: Cold exposure increases glucose uptake. The uptake of 2-NBDG was assessed by imaging thermogenic adipocytes after 2 h of (A) physiologic temperature and (B) cold exposure. Scale bar: 20 μm. (C) 2-NBDG uptake was quantified in physiologic and cold exposure conditions (n=3). * $p < 0.05$.

The cold condition also demonstrated increased metabolic flux as determined from metabolomic analysis. The ratio of M2 glutamate to M3 pyruvate was used as an indicator of overall metabolic flux (Fig. 3.17). After 10 min, the cold and warm metabolic flux were equal. The metabolic flux in the cold condition was consistently higher than the warm condition at the later 30, 90, and 120 min time points. The increased glucose uptake and cellular energy status, as determined from the ATP:ADP ratio, may account for the increased metabolic flux upon cold exposure.

3.4.4 Glycolysis is Required for Rapid Cold-induced Thermogenesis

To understand the effect that impaired glucose metabolism has on rapid cold-induced thermogenesis in adipocytes, different interventions on the glycolytic pathway were tested (Fig. 3.18). A ten-fold reduction in the amount of glucose in the imaging medium (25 mM reduced to 2.5 mM) prevented the intracellular temperature increase during environmental temperature decline. Prevention of glucose uptake with 2-DG was also tested. Treatment of the cells with 100 mM 2-DG similarly prevented the intracellular temperature

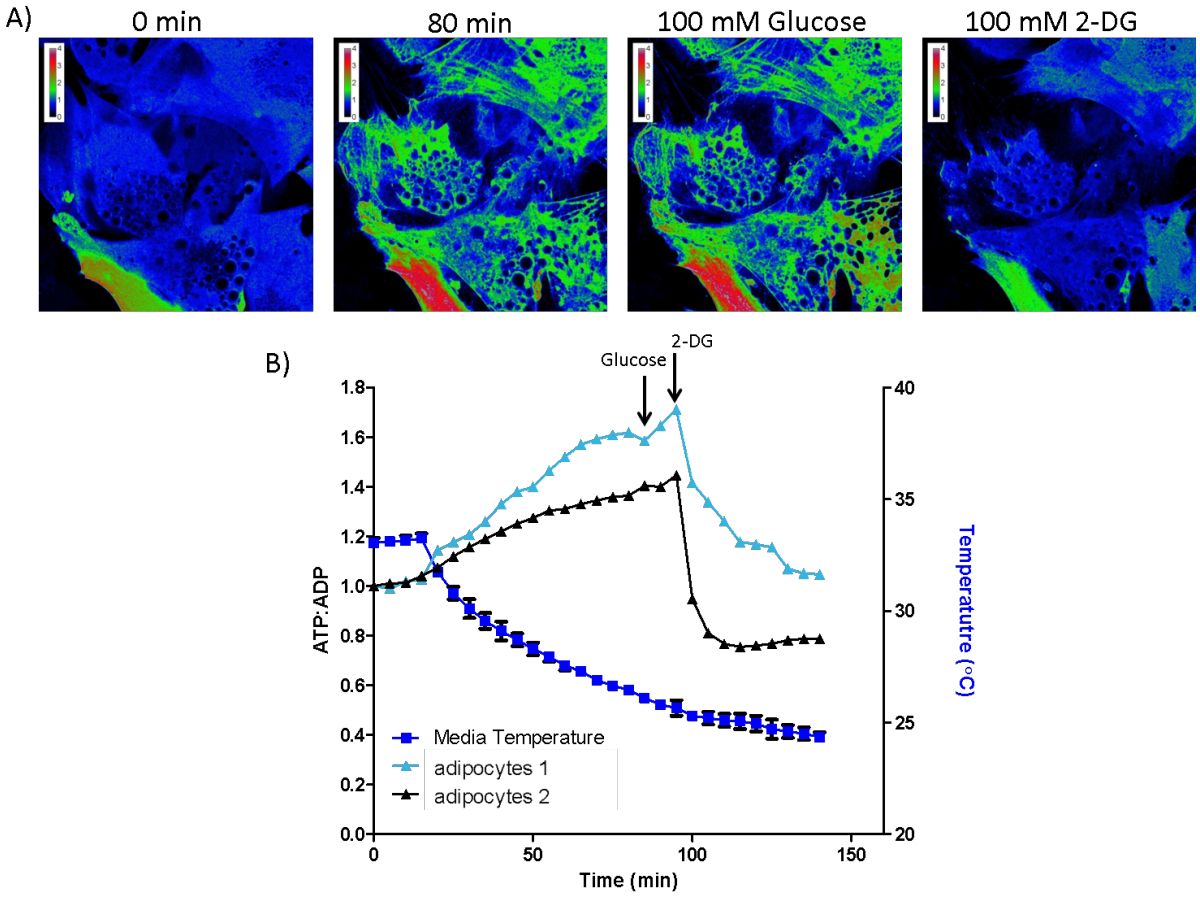

FIGURE 3.16: Cold exposure increases the ATP:ADP ratio. (A) The ratio of ATP to ADP was monitored by imaging thermogenic adipocytes after viral transduction of a fluorescent ATP/ADP biosensor during an environmental temperature decline. (B) The measured ATP:ADP ratio was normalized and both high glucose and subsequent 2-DG treatment confirmed the biosensor response.

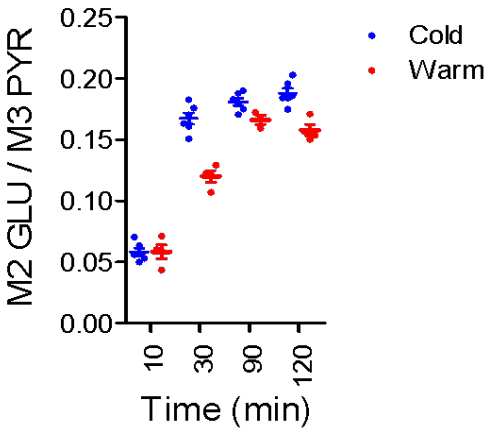

FIGURE 3.17: Cold exposure increases metabolic flux. The ratio of M2 glutamate to M3 pyruvate indicates metabolic flux. Metabolomic analysis was performed by Dr. Ben Olenchock.

increase. Finally, treatment with 10 μM of the specific PFKFB3 inhibitor 3PO had the same effect as the low glucose and 2-DG treatment. Overall, these results demonstrated glycolysis is required for rapid adipocyte thermogenesis in response to cold exposure.

3.5 Adipocyte Co-culture Platform

The adipocyte co-culture platform was developed to control a temperature gradient and monitor co-culture interactions and temperature regulation-associated cell responses in the microenvironment. Our temperature control system offered a landscape for biological analysis of close-proximity interactions between warm- and cold-exposed cells.

3.5.1 Temperature Gradient Simulation

A COMSOL simulation of the heat transfer from the controlled surface of the peltier thermoelectric devices and through the glass coverslips demonstrated a temperature gradient in the cell culture media between the cell monolayers (Fig. 3.19A). The peltier surface for

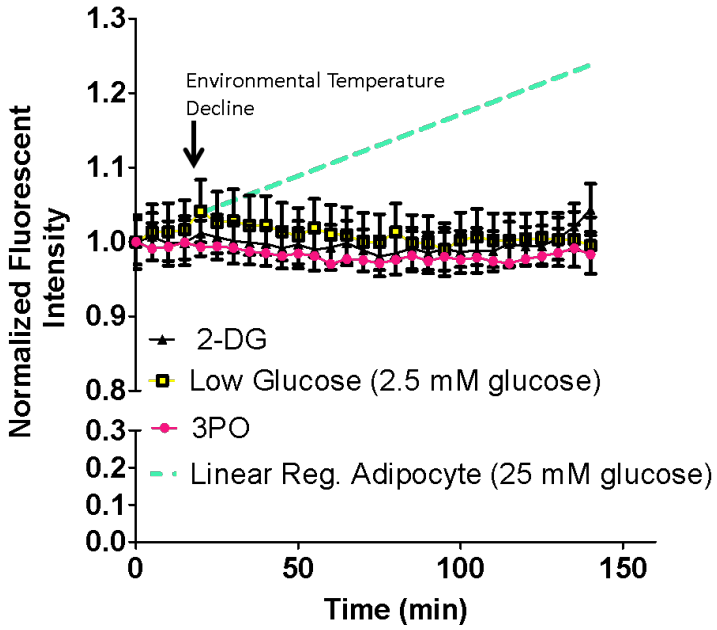

FIGURE 3.18: Impaired glucose metabolism prevents rapid, cold-induced thermogenesis in adipocytes. Low glucose, 2-DG, and PFKFB3 inhibitor 3PO prevent the intracellular temperature increase with environmental temperature decline.

the warm condition was modeled for a $37.5°C$ setpoint while the cold condition was modeled for a $29.5°C$ degree setpoint to offset heat loss through the glass coverslip. A plot of the temperature as a function of the position along the z-axis showed the gradient in the media was linear (Fig. 3.19B).

3.5.2 PGC1α mRNA Upregulation in Adipocytes Exposed to Cold

PGC1α is one of the canonical cold-induced genes in thermogenic adipocytes (see Section 1.2.4.5). Cells on glass coverslips exposed to $30°C$ had significant upregulation of PGC1α mRNA levels after 4 h (Fig. 3.20). An initial pulse of $30°C$ for 15 min or 1 h at the beginning of a 4 h experiment could not initiate events leading to inevitable cold-induced upregulation. Sustained cold-exposure was the only tested condition resulting in an increase in PGC1α mRNA compared to the $37°C$ control.

Real-time upregulation of PGC1α was assessed using SmartFlare technology. The

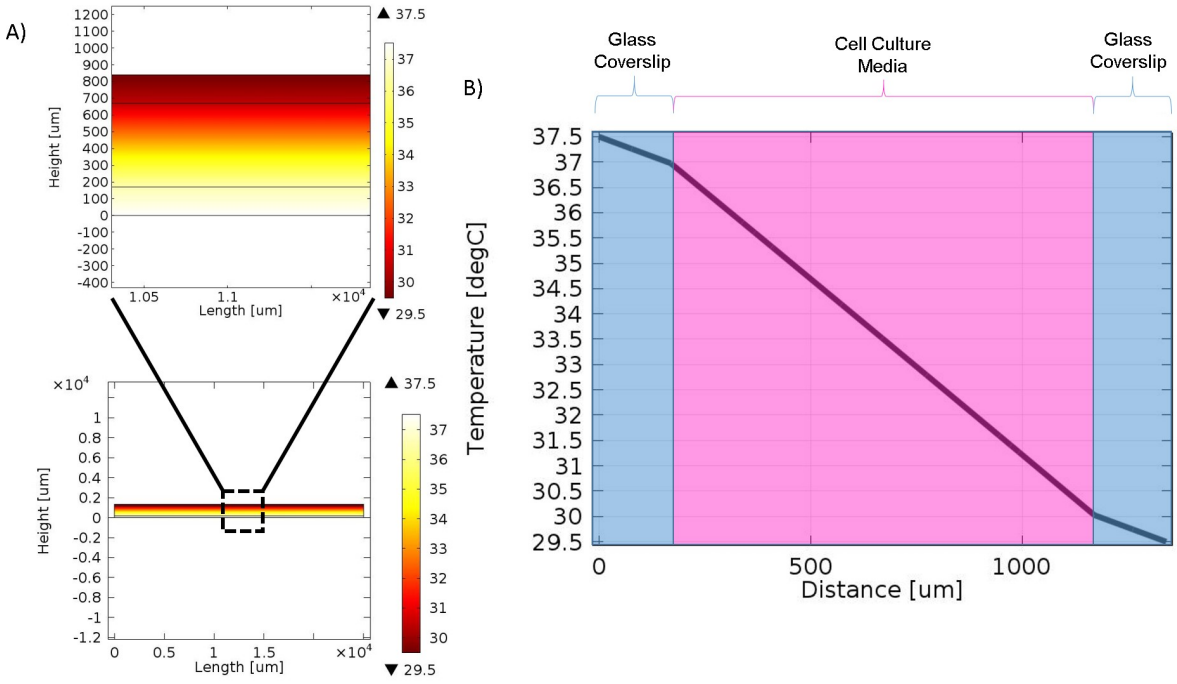

FIGURE 3.19: A linear temperature gradient develops in the media between the co-culture samples. (A) A COMSOL heat transfer simulation demonstrates the temperature gradient between two glass coverslips, on which cell monolayers are cultured, separated by a 1 mm distance as determined by the thickness of the PDMS gaskets. (B) The gradient is plotted as a function of the vertical distance in the co-culture assembly.

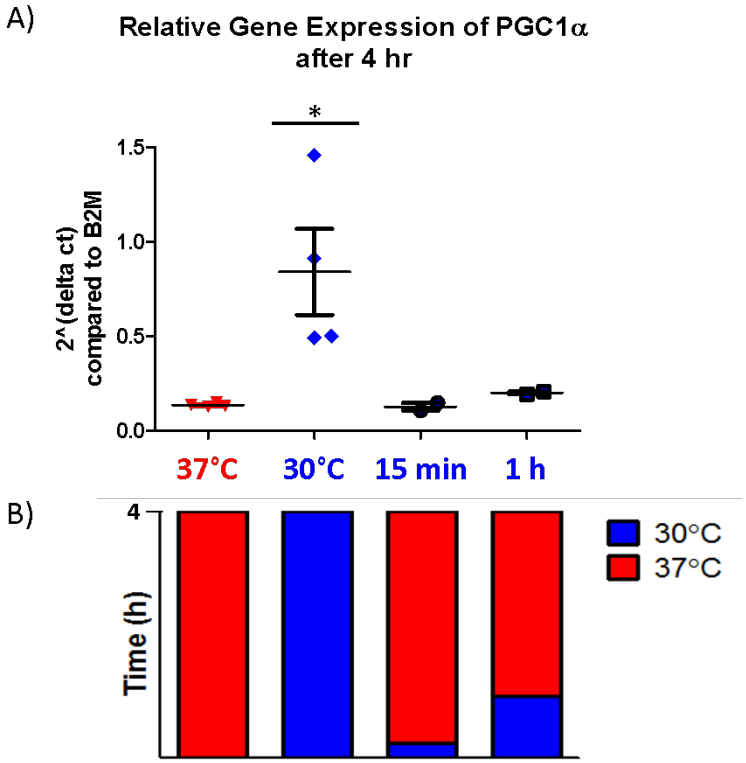

FIGURE 3.20: Sustained cold exposure in adipocytes is necessary for PGC1α mRNA levels to increase. (A) Relative gene expression demonstrates that 4 h of continuous 30°C exposure increases PGC1α mRNA as compared to 15 min or 1 h pulses of 30°C. (B) A graphical representation of the duration of 37°C and 30°C conditions. * $p < 0.05$.

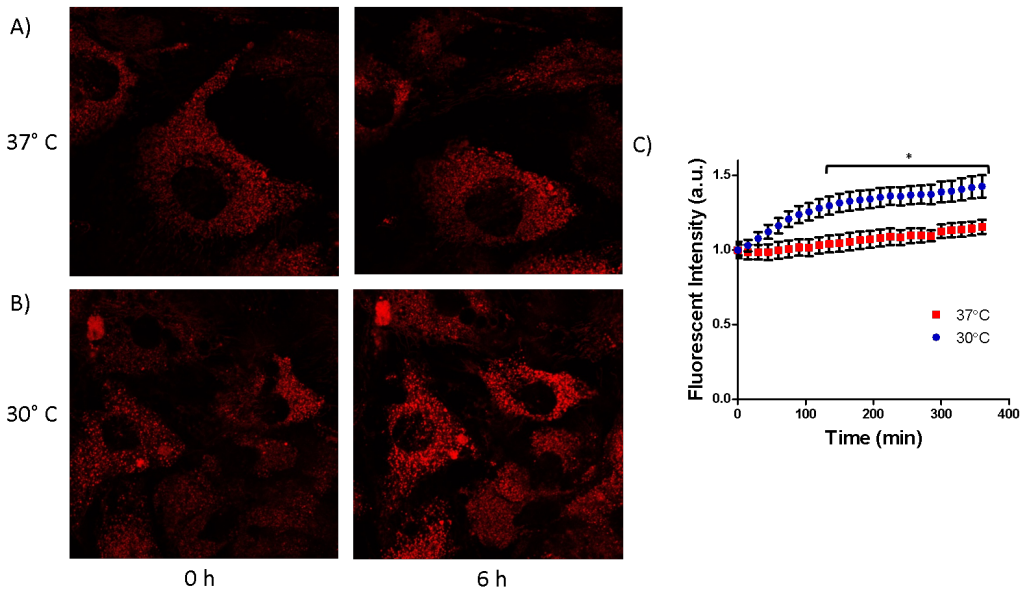

FIGURE 3.21: SmartFlare technology demonstrates real-time PGC1α mRNA upregulation in cold. Real-time imaging of the PGC1α SmartFlare was acquired over 6 h in 5-day differentiated adipocytes (A) maintained at 37°C and (B) exposed at 30°C. (C) Intensity of the SmartFlare was normalized in 37°C and 30°C adipocytes and monitored over time. * $p < 0.05$.

SmartFlare is a method of live-cell RNA detection which utilizes gold nanoparticles with conjugated oligonucleotide capture sequences for a target mRNA. Reporter flare strands with complementary sequences to the capture strands are initially bound to the capture strands. The reporter strands carry a fluorophore, but the fluorophore is quenched by the gold nanoparticle. Target mRNA replaces the reporter strand and then the reporter strand is released. The fluorophore is no longer quenched and fluorescence emission is detected. Cells that had endocytosed the SmartFlare were imaged at 37°C or 30°C for 6 h (Fig. 3.21A-B). Quantification of the fluorescent intensity demonstrated a significant increase in PGC1α mRNA in the cells maintained at 30°C after 135 min (Fig. 3.21C).

3.5.3 Modulation of Thermogenic Signaling in a Temperature Gradient

Real-time paracrine crosstalk between warm and cold adipocytes altered the expression of thermogenic genes. PGC1α is one of the canonical cold-induced genes in thermogenic

adipocytes (see Section 1.2.4.5). The upregulation of PGC1α mRNA seen in homogeneous, cold-exposed adipocyte culture was suppressed when cold-exposed adipocytes were co-cultured with nearby warm adipocytes (Fig. 3.22A) as determined by real-time quantitative PCR. A co-culture of warm adipocytes and warm preadipocytes suppressed PGC1α expression in the adipocytes compared to the homogeneous, warm culture of adipocytes alone. The expression could be increased back to the basal level (the level in the adipocytes cultured alone at $37°$C) if the adipocytes were exposed to $30°$C with warm preadipocytes as the co-culture partner.

Sarco/endoplasmic reticulum Ca^{2+}-ATPase 2 (SERCA2a) is a protein that hydrolyses ATP to transport calcium from the cytosol to the lumen of the endoplasmic reticulum. In adipocytes, SERCA2a has been indicated in a thermogenic mechanism involving intracellular heat generation via futile cycling of calcium in adipocytes [140, 173]. In co-culture combinations, the relative gene expression of SERCA2a in adipocytes was the highest when the adipocytes were exposed to cold and their co-culture partner was warm preadipocytes (Fig. 3.22B). Cold-exposed adipocytes co-cultured with warm adipocytes did not induce gene expression compared to warm co-culture with either preadipocytes or other adipocytes.

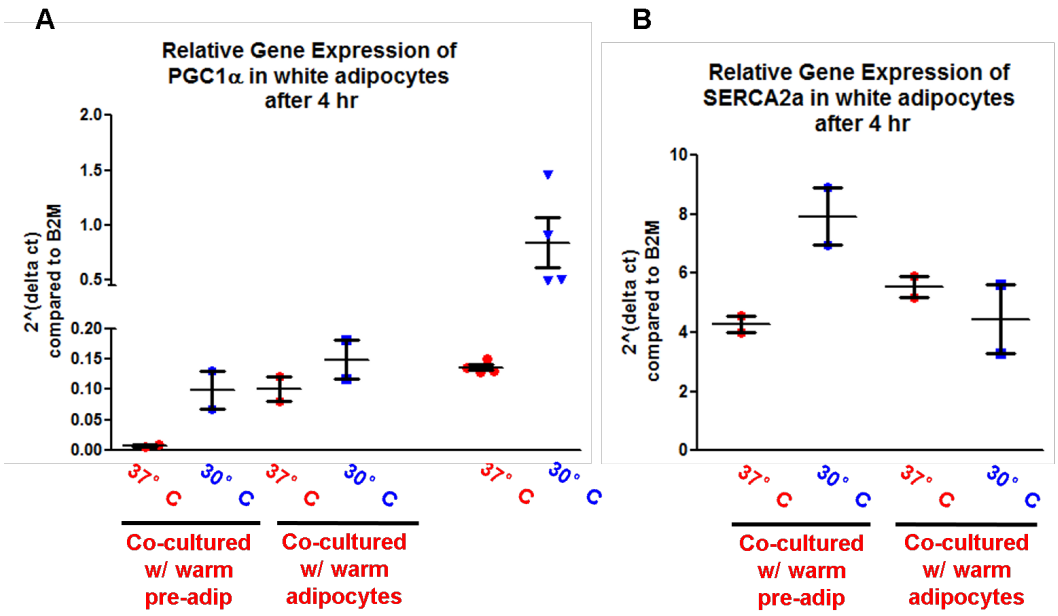

FIGURE 3.22: All data represent relative gene expression in adipocytes. The temperature of the adipocytes and their co-culture partner are indicated below the data point. (A) PGC1α mRNA is suppressed in warm adipocytes co-cultured with warm preadipocytes, and upregulation of PGC1α is blunted in cold-exposed adipocytes co-cultured with warm adipocytes for 4 h. (B) Relative gene expression of SERCA2a increases in cold-exposed adipocytes co-cultured with warm preadipocytes.

CHAPTER 4. DISCUSSION

Portions of this content have previously been published in Rexius-Hall, M. L., Mauleon, G., Malik, A.B., Rehman, J., and Eddington, D.T. (2014) Microfluidic platform generates oxygen landscapes for localized hypoxic activation, Lab Chip. 14(24):4688-95 and Rexius-Hall, M.L., Rehman, J., and Eddington, D.T. (2017) A microfluidic oxygen gradient demonstrates differential activation of the hypoxia-regulated transcription factors HIF-1α and HIF-2α, Integr. Biol. Advance Article DOI 10.1039/C7IB00099E.

4.1 Large-area Oxygen Landscapes

By changing the channel geometries of the underlying microfluidic network layer, we achieved binary dual condition, square wave, oscillating, and linear spatial profiles. Of the different landscapes designs, only the linear gradient required more than two different inlet gas compositions. A steady, linear gradient across the entire device with only two gas compositions was not able to be achieved due to the scale of the device (see Fig. 2.4 for dimensions). The conventional source and sink methods for creating a linear gradient do not work at the scale of the device (centimeters as opposed to millimeters or micrometers), because although there is constant perfusion of different oxygen compositions across the PDMS membrane, there is also exchange with the environment above the media in the open-well format (Fig. 3.2D), creating another source and sink at this large scale. For this reason, equilibration of gas contents in the microfluidic network with those of the surrounding, ambient environment cannot be opposed in a device with this large of an area without providing multiple inlet gas compositions to mix spatially in the device.

The large scale of the overall device was designed to accommodate enough cellular material for standard biological techniques, especially western blotting where tens of μg of protein are needed per lane when running a gel. Although single-cell western blot technology has been developed [174], the method which requires a large, pooled quantity

of protein from a population of lysed cells remains the standard. One of the objectives of our overall design was the compatibility of our device with such standard techniques.

4.2 Dual Condition Oxygen Landscape Device

The immunofluorescent imaging, western blotting, and quantitative PCR results demonstrate analysis of cell responses in the dual condition oxygen landscape. The advantage of having cells with different states of HIF activation in the same open well is that it allows assessment of how the cells interact across an oxygen gradient. This tool presents an opportunity to fundamentally advance hypoxia research because current homogeneous oxygen systems do not allow crosstalk between cells exposed to different oxygen levels. The design lends itself to future study of the crosstalk interactions of differentially oxygenated cells with respect to cell-cell contact (because there is a single confluent monolayer of cells) and secreted factors (because there is a single, shared reservoir of culture medium).

Real-time PCR results of the relative gene expression of LDHA, Glut1, PDK1, and PDK3 demonstrated that the spatial layout of the oxygen landscape can be resolved in the expression of genes that are under the transcriptional activity of HIF-1α. By examining metabolic genes in MSCs, it was showed for the first time the metabolic profile of hypoxic cells in an oxygen landscape with normoxic neighbors is similar to that of cells in homogeneous hypoxia. The results from Fig. 3.4 show that that relative gene expression of metabolic genes was not altered in the dual condition platform as compared to the homogeneous controls. However, in addition to regulating MSC metabolism, hypoxia is a central regulator of paracrine signals involved in stem cell maintenance and cancer progression [175, 176]. The hypoxia-induced secretion of molecules and microvesicles is believed to be the primary source of effects reported in hypoxia-conditioned media experiments.

The biological significance of this device is that it allows for the study of additional signaling pathways and growth factors that may be differentially regulated in cells being co-cultured while exposed in real-time to two distinct oxygen levels. For example, hypoxic tumor cells may release paracrine factors that activate angiogenesis in normoxic endothelial cells. Prior to this device, such interactions could not be studied in real-time and had to rely on conditioned media experiments.

Traditional hypoxia-conditioned medium experiments have the disadvantage of having culture media transferred to other cells at a single, selected time point. Using the dual condition oxygen landscape device, normoxic cells can be exposed to factors from hypoxia-conditioned medium in a real-time and continuous fashion, thereby overcoming the rapid degradation and short half-lives of the secreted molecules present in traditional conditioned medium experiments. Therefore, our new platform is ideal for investigations of real-time, hypoxia-induced effects of the MSC secretome on a differentially oxygenated co-culture and lays the framework to address important developmental, regenerative, and pathophysiological responses to oxygen landscapes.

The finding in HLMVECs that PFKFB3 is enhanced in dual condition hypoxia is likely an example of a crosstalk interaction between normoxic and hypoxic cells unveiled by the platform. The promoter sequence of PFKFB3 has multiple HREs for the binding of HIF transcription factors [177] so upregulation in hypoxia is expected. However, there was no significant upregulation of PFKFB3 in the homogeneous hypoxia condition at the 4 h time point. Interestingly, 4 h was enough time to observe significant upregulation in the dual condition hypoxia cells but not homogeneous hypoxia. At 24 h, there was an increase in PFKFB3 at the protein level in both homogeneous hypoxia and dual condition hypoxia. This confirms that there was an expected upregulation effect in the homogeneous hypoxia device. The upregulation of protein in the dual condition hypoxia cells was more pronounced than the homogeneous hypoxia. It may be possible that the dual condition device is effecting the dynamics and extent of PFKFB3 upregulation, and that

paracrine crosstalk between normoxic and hypoxic cells leads to earlier transcription and more robust increase of PFKFB3.

The mechanism by which enhanced induction of PFKFB3 occurs in the dual condition landscape has not yet been elucidated. It has previously been shown that VEGF increases the expression level of the glycolytic activator PFKFB3 [170, 178]. It would be interesting to determine if there is any change in VEGF expression in HLMVECs cultured in the dual condition landscape. Endothelial cells are not typically a VEGF-expressing cell type; they robustly express VEGF receptors and respond to VEGF stimulation. Research suggests endothelial cells are capable of expressing autocrine VEGF [179–181]. If the dual condition landscape were to induce VEGF expression in endothelial cells more than homogeneous hypoxia, it could support the observed enhancement of PFKFB3. There is also evidence that lactate, a secreted metabolite, affects PFKFB3 signaling [182]. It may be possible that the metabolites available in the shared media reservoir of the dual condition device vary substantially compared to metabolites in homogeneous controls. Taken together, the idea of a growth factor or metabolite being responsible for differential expression, particularly of PFKFB3, between homogeneous hypoxia and dual condition hypoxia is a realistic possibility.

4.2.1 Limitations and Future Directions

The current open-well design has some limitations. For instance, resolving the behavior of the subpopulation of cells within the gradient region of the dual condition device has not yet been achieved. While this may be possible using a combination of microscopy and assessments of cellular behavior via fluorescent reporters at known positions, we mainly focused on bulk cell population analysis techniques such as PCR and western blotting as readouts. In the experiments, the cells on the devices were collected in equal thirds after an experiment: a left (hypoxic), middle (gradient-containing), and right (normoxic) section. Analysis was only performed on the left and right sections. At this time, the

average response of the gradient section is not of interest. By analyzing only the far-left and far-right sections, there was confidence reporting a known, homogeneous oxygen tension associated with the site from which the cells were harvested.

The open-well format is also inherently exposed to convective transport processes akin to those that cells experience in Petri dishes and well plates. The platform is dominated by convective processes over diffusive processes. The device lends itself to study paracrine activity because there is a single, shared reservoir of culture medium. During experiments, there is an absence of flow in the open-well platform, but the convective transport would rapidly mix secreted molecules throughout the entire volume of cell culture media. This device is not designed to track the cell source of released paracrine factors because convection will lead to an intermingling of the released factors. However, the open-well nature of the device does allow a researcher to test whether the proximity of cells exposed to distinct oxygen levels results in a different cellular phenotype than if they were exposed to a single oxygen level. While it is not possible, for example, to maintain a gradient of hypoxia-secreted factors that diffuse and affect the neighboring normoxic cells while being received as a concentration gradient, we can offer a system that allows real-time, continuous conditioned medium experiments.

Many enclosed microfluidic channel systems can avoid the convective transport issue, but as the open-well design exists currently, the large-area platform cannot. Future work could include design modifications to transition the existing platform into an enclosed microfluidic system. However, eliminating the open-well format complicates cell harvesting and media replacement which will likely require a syringe pump. Inevitably, this change also introduces a new host of issues, including recurring air bubbles and shear stress. Furthermore, the advantage of the user-friendly, open-well tool is its accessibility to laboratories not necessarily specializing in microfludics. Eliminating the open-well format would remove that advantage, but may be worth the trade-off to probe specific biological questions.

Both the sensitivity and the lower limit of measurable oxygen levels that can be maintained at the cell culture surface matter for biological studies. For cancer studies in the platform, levels of 1-2% O_2 are considered moderate hypoxia that begins to activate mTOR pathways, while 0.1% represents severe hypoxia that is experienced in the core of solid tumors. The described open-well platform is sensitive to the distance away from the membrane (3.2D). It is, therefore, important to know what levels of oxygen can actually be maintained steadily and consistently at the surface for hypoxia study applications. During oxygen modulation, there was constant perfusion of the hypoxic network with 0% oxygen (5% CO_2, balanced nitrogen. The oxygen measurements using both PtOEPK sensors and an optical probe sensor indicated that extremely hypoxic conditions were maintained near the surface of the membrane on which the cells were cultured. Oxygen-scavenging chemicals, such as pyrogallol and sodium sulfite, have been compared to 0% O_2 in microfluidic devices using gas perfusion through channels and diffusion across PDMS membranes to determine the intensity of PtOEPK sensors in the absence of oxygen. We have demonstrated that values obtained from oxygen scavengers and anoxic perfusion closely match [183]. While our oxygen measurements do not have the resolution to precisely determine the hypoxic conditions experienced by the cells on the membrane, the best estimate is that the level directly across the membrane directly above a buried channel perfused with 0% O_2 is $\leq$ 0.5% oxygen.

The constant perfusion of buried microchannels leads to evaporation in the open-well reservoir. For this reason, the current design is suitable for studies up to approximately 24 h. However, we recognize that certain studies require days or weeks of oxygen modulation. For long-term cell culture studies, it may be necessary to replace media in the reservoir with a syringe pump or circulate media with a peristaltic pump. In these long-term cases, it may also be beneficial to add an additional hydration layer to perfuse with PBS to prevent evaporation in the media reservoir.

4.3 Stable Linear Oxygen Gradient Device

The downsized, simplified device allowed for the study of cells exposed to a stable linear oxygen gradient, but it limited the kinds of analyses that were able to be performed with the device. The gradients generated on the scale of millimeters limited analyses to imaging techniques due to the small population of cells.

In our linear gradient platform, we showed that the spatial gradient develops over time, becoming completely developed after several hours due to the bulk PDMS in the diffusion gap on the scale of several millimeters. Although this time to equilibrate may be seen as a limitation of the device, cells could easily be exposed specifically to the fully developed spatial gradient if, for example, the cells were cultured on a gas-permeable PDMS membrane that was placed on top of the base PDMS membrane after several hours of oxygen modulation. Oxygen diffuses across an additional 100 μm PDMS membrane on the scale of tens of seconds [1, 74].

Although our primary focus was demonstrating a linear spatial gradient, we acknowledge that certain oxygen control applications may also call for control of a temporal gradient. Computer-controlled microdispensing nozzles have been successfully used to deliver intermittent hypoxia to a PDMS-based gas perfusion device [184] and could be applied to our platform to temporally control the oxygen levels in the device or change the direction of the gradient. Furthermore, not all physiological gradients are necessarily linear, but for the purpose of defining clear activation thresholds, linear gradients are more suitable.

The differences between the oxygen-dependent stabilities of HIF-1α and HIF-2α are well-documented. HIF-2α has a different sub-nuclear distribution than HIF-1α, lending to its increased stability and slower mobility as compared to HIF-1α [185]. Higher levels of oxygen have been shown to inhibit HIF-2α degradation and allow for rapid accumulation in human endothelial cells as compared to oxygen levels required to inhibit HIF-1α degradation (3.5% O_2 vs. 1.0% O2, respectively) [27]. The vast majority of studies which

have established oxygen level thresholds have been performed in cells exposed to a single, homogeneous oxygen environment (e.g. one cell culture plate is exposed to 3% while a separate plate is exposed to 1%). Using microfluidic devices, we studied whether the threshold of activation differs if cells are cultured in an open-well gradient which allows for biological interactions between cells that are exposed to varying oxygen levels. Here, we show in endothelial cells exposed to an oxygen gradient from 0% to 21% that HIF-2α is activated throughout the entire gradient when compared to cells exposed to homogeneous normoxia, suggesting a "contagion" of HIF-2α activation. Even cells within the spatial gradient that are exposed to continuous normoxia exhibit significant accumulation and nuclear translocation of the HIF-2α transcription factor, likely due to the close proximity of cells exposed to hypoxia within the same gradient.

The activation of HIF-2α demonstrates hyproxya (hypoxia by proxy), which describes the activation of hypoxic signaling in normoxic cells by hypoxic neighbors which may constitute an adaptive signal within a tissue in which localized hypoxia can elicit a broader systemic response. It is noteworthy that this was only true for HIF-2α activation but not for HIF-1α activation, suggesting that HIF-1α is only activated in hypoxic cells and not when neighboring cells experience hypoxia.

The mechanism by which hyproxya of HIF-2α activation occurs is not yet known. It likely involves a multitude of potential signals by which hypoxic cells can act as sentinels for normoxic neighbors and could include paracrine signals such as the secretion of exosomes, metabolites, or growth factors. It has been previously reported that exosomal miRNAs may activate HIF independent of hypoxia [8, 186]. Therefore, one can envision a scenario in which the exosomes from the hypoxia-exposed cells contain miRNAs that activate HIF in the nearby normoxia-exposed cells. Additionally, hypoxia alters cellular metabolism, increasing a cell's dependence on glycolysis over oxidative phosphorylation to produce ATP. As a result, metabolites such as lactate, succinate, and fumarate have

been shown to accumulate intracellularly [187, 188]. These metabolites may then be secreted into the extracellular space and affect surrounding cells. A specific cell surface receptor for lactate and succinate has been identified [189–191].

The source of the reported biological effects in hypoxia-conditioned media experiments is thought to be the secreted molecules or microvesicles. The disadvantage of traditional conditioned media experiments is that there exists a single, isolated time point when cell culture media is harvested and transferred to other cells. Oxygen gradient devices in which differentially-oxygenated cells share media allow for continuous exposure of normoxic cells to the hypoxia-induced secretome. Interestingly, HIF-2α transactivation is reported as being sensitive to the composition of cell culture media. HIF-2α specifically acts as a response factor to glucose concentration in media [192, 193]. Media supplemented with acetate, which can be released by tumors, results in acetylation of HIF-2α and nuclear localization of an acetate-dependent acetyl CoA synthetase ACSS2 required for induction [182]. Hypoxia-conditioned media from cells secreting acetate can induce this HIF-2α acetylation [193].

Understanding how HIF-1α and HIF-2α are differentially regulated in oxygen gradients is critical because HIF-1α and HIF-2α can have opposing roles based on their downstream targets [194–199]. Our findings demonstrate a novel aspect of differential HIF-1α and HIF-2α activation: their upstream activation by low oxygen. HIF-2α activation does not require hypoxia in all cells but can be activated when only selective cells are exposed to low oxygen levels. These results highlight the importance of understanding the effect of cell-cell interactions in an oxygen gradient environment. Further mechanistic studies using the microfluidic device we engineered could allow for the isolation of the intercellular signals which mediate HIF-2α hyproxya —hypoxia by proxy— and allow for therapeutic modulation of HIF-2α levels even in the absence of direct hypoxia.

4.4 Cold-induced Adipocyte Thermogenesis

Our thermogenesis measurements of cells containing a cell-permeable themroprobe have all been ratiometric measurements normalized to baseline. Assigning absolute temperature with intracellular thermoprobes has been an ongoing debate and hotly contested issue in the field [200–203]. Baffou *et al.* have questioned whether single-cell thermogenesis could ever be demonstrated by arguing that dimensional analysis of a standard heat diffusion equation shows a single cell is capable of a temperature increase on the order of 10^{-5} K, and body temperature in organisms increasing by several Kelvin is the result of the collective effect of 10^{13}-10^{14} cells.

On the other hand, numerous probes have reported intracellular temperature differences on the scale of several Kelvins. Kiyonaka *et al.* point out that the conclusions of Baffou *et al.* come from a macroscopic heat diffusion equation applied to the parameters of a single, microscopic cell. Furthermore, Baffou *et al.* used a conductivity value assuming the cell interior is a water-like environment as opposed to a heterogeneous interior of proteins, lipids, and water all possessing different conductivity values. Furthermore, Kiyonaka *et al.* posit that the heat source isn't on the scale of the cell as a whole but on the scale of the mitochondria (10 μm vs. $<$ 100 nm, respectively). The changes in conductivity and the dimension of the heat source alone reduces the heat needed to increase the temperature 1 K in 1 s 100-fold. Additionally, Baffou *et al.* used an equation that assumed uniformity of heat diffusion in a cell, but numerous publications using intracellular thermosensors have shown heterogeneous subcellular temperature distributions [156, 157, 160].

Importantly, Suzuki *et al.* notes that the detection of a 1 K temperature increase would only necessitate a sustained temperature increase in the same volume of water as the thermosensor occupies. This is important considering most thermoprobes used in intracellular thermometry are several orders of magnitude smaller than the 1 μm^3 mitochondrian

volume or diffraction-limited volume of the microscope used by Baffou *et al.* in their calculation.

Different groups have determined the heat power delivered by brown adipocytes using various calorimetric and noncalorimetric techniques. The results have been 1.6 [204], ≈ 5 [205], 2.3 [206], 1 [207], 0.5 [164], and 0.82 nW/cell [150]. The majority of these reported values are an order of magnitude higher than the 100 pW value used by Baffou *et al.* to determine that the expected temperature change is 10^{-5} K in a cell. With so many papers using chemically different thermosensors and yet reporting localized intracellular temperature increases in a variety of cell types of at least 1 K [156, 160, 208], it is hard to dismiss the findings.

The thermoprobe we used in the adipocyte and preadipocytes has been previously reported by Uchiyama *et al.* to demonstrate a 1 K temperature difference between the nuclei and cytosol in HEK293T cells using confocal microscopy [160]. However, the temperature resolution was only (0.29–1.0°C). This resolution was much lower than when the thermoprobe was measured using a spectrofluorometer (0.01–0.25°C). All our measurements were done using microscopy, so with low temperature resolution, we do not claim to be able to assign an absolute temperature to our ratiometric thermoprobe measurements. Based on the normalized measurements compared across different experimental conditions (physiologic temperature vs. environmental temperature decline and preadipocyte vs. adipocyte), we are confident the thermoprobe is sensitive to intracellular temperature changes and can be used to demonstrate thermogenesis in response to different treatments. The thermoprobe is, therefore, a useful tool to demonstrate intracellular heat generation even without assigning absolute temperature values.

Brief cooling was needed to introduce the cell-permeable thermoprobe into adipocytes and preadipocytes. There was concern that cooling as part of the protocol to introduce the thermoprobe would initiate thermogenesis in the differentiated adipocytes, but 37°C incubation for at least 15 minutes after thermoprobe introduction and before imaging

experiments began was performed. The result that no intracellular temperature increase was seen in the warm control adipocytes (even though they required brief cooling during introduction of the thermoprobe) demonstrates that the requirements of the protocol do not preclude the use of the thermoprobe in adipocyte thermogenesis applications.

The mechanism for direct cold sensing by adipocytes has not been identified. We can conclude that there exists a sympathetic nervous system-independent mechanism sufficient to increase glucose uptake, metabolic flux, and intracellular temperature during cold exposure.

The discovery of brown adipose tissue in adults ushered in an era of revitalized interest in brown adipose tissue and nonshivering thermogenesis research. The serendipitous way brown fat was discovered in adults involved glucose uptake (see Section 1.2.4.2). There is some controversy whether thermogenesis requires glucose or if thermogenesis is a prerequisite for the enhanced glucose uptake. Nedergaard *et al.* argues the later [125], citing that norepinephrine has no ability to increase glucose uptake in mice without UCP1 [209]. Albert *et al.* report the former, demonstrating that mice with impaired activation of glucose metabolism (adipose tissue-specific inactivation of mTORC2) were hypothermic and unable to maintain a stable body temperature during cold exposure compared to control mice [92].

Our work supports the conclusions of Albert *et al.* While glucose uptake may require fatty acid metabolism and mitochondrial respiration may enhance glucose transport[210], we have demonstrated that a demonstrable intracellular temperature increase will not proceed when glucose metabolism is impaired.

The mechanism by which glucose controls thermogenesis is not yet known. Others have reported that enhanced glucose uptake is a consequence of the loss of mitochondrial ATP production due to UCP1-dependent uncoupling; glucose uptake and glycolysis are increased to compensate for the lack of mitochondrial ATP production with more

cytosolic ATP production. The glucose may be used to synthesize new triglyceride depots. The glucose may be needed to make pyruvate to then form oxaloacetate from the pyruvate to increase the capacity of the citric acid cycle. Indeed, it has been observed that the activity of pyruvate carboxylase, the enzyme that converts pyruvate into oxaloacetate, is significant in brown fat [211]. Furthermore, pyruvate carboxylation requires ATP, the production of which relies heavily on glycolysis and cytosolic ATP production due to the loss of mitochondrial ATP production. Here, we report impaired activation of glucose metabolism prevents thermogenesis. It follows that future studies to enhance glucose uptake or glycolysis in adipocytes may boost cold-induced thermogenesis.

4.5 Temperature-Controlled Adipocyte Co-culture Platform

Some of the most significant molecular findings in the field of obesity research during the past decade have been the discovery of brown adipose tissue in human adults as well as paracrine interactions with the potential to convert nonthermogenic fat into thermogenic brown fat. A potent stimulus to induce a phenotypic browning of fat is the exposure to cold temperature. Our engineered system which generates a temperature gradient allows us to study paracrine interactions between warm and cold fat cells. Understanding this interaction is fundamentally important because *in vivo* subcutaneous fat tissue closer to the surface of the skin experiences a lower temperature during cold exposure than the deeper fat tissue which is closer to the body's core. By regulating temperature gradients, we study the effect of paracrine factors released by cold-exposed thermogenic cells on nearby cells that are not being directly exposed to cold.

The finding that paracrine interactions between warm and cold adipocytes or preadipocytes modulate gene expression has not previously been shown. Others have reported secreted factors leading to "browning" of adipocytes (as determined from induction of a program of thermogenic genes). Irisin, the most wellknown of these secreted factors, is

not secreted by adipocytes or preadipocytes but by muscle cells [212]. Other secreted factors that have been indicated in promoting browning of adipocytes include cardiac natriuretic peptide (ANP114), bone morphogenetic protein 7 (BMP7), fibroblast growth factor 21 (FGF21), adenosine, and several microRNAs (e.g. miR133a, miR196a, miR193b-365) [213]. If cold-induced adipocytes can secrete a factors or factors to promote browning, the cold-exposed adipocyte coverslip sample has the potential to effect the warm coverslip sample sharing the same media. Presently, we measure relative gene expression based on genes of interest or genes we hypothesize to be subject to differential temperature regulation. Future work could include a transcriptomic screen to identify genes differentially expressed in the temperature gradient co-culture as compared to homogeneous warm co-culture.

The two monolayers cultured on the coverslip samples were maintained $\approx$1 mm away from each other using PDMS gaskets that were irreversibly bonded to the glass coverslips. Two PDMS gaskets formed a seal for the co-culture assembly by reversible PDMS-PDMS contact. The stacking of the peltier and the heat sink on the top coverslip did not cause media to leak out of the co-culture assembly because the PDMS elastomer deformed enough under the pressure to accommodate the volume of media between the coverslips. We have not investigated whether the added pressure has an effect on the biological cell responses. In the future, we could easily demonstrate for genes of interest (e.g. PGC1α or SERCA2a) whether the pressure effect is negligible by comparing relative gene expression of homogeneous warm co-culture assemblies with and without the added pressure of the temperature regulation peltier system.

Once current was running through the peltier, a temperature differential was created between each side. The temperature control and active cooling of one side of the peltier was at the expense of warming the opposite side. The peltiers will work as long as heat is removed from the hot side. Currently, the hot sides of the peltiers are each cooled by a heat sink constructed from a brass disk covered with an ice pack to pull heat from the hot

sides. This setup is able to keep the peltier power output under 100% during the duration of the 4 h experiment. However, for studies requiring longer time points, a better heat sink, such as a computer CPU heat sink, should be integrated into the system.

4.6 Conclusion

The microengineered systems presented here exemplify how control of the microenvironment can help uncover novel biological phenomena. We have called upon engineering methods to probe important questions in cellular biology: Are there paracrine interactions between differentially oxygenated cells? What is the threshold of activation of HIF-1α and HIF-2α in a spatial oxygen gradient? Do cold adipocytes modulate gene expression in warm neighbors? The answers have biological significance and are of great value to biomedical researchers but they also highlight the value of microengineered systems for signaling research.

APPENDICES

CHAPTER A. Protein Lysis Protocol

Protein Lysis

Cells in a culture dish

1. Place cells on ice. (Make sure centrifuge is cold.)

2. Aspirate off media then wash cells in cold PBS (+PMSF). Add some PBS back to the well (10 cm dish –> 200 μl).

3. Scrape the cells off the dish using a cell scraper, then pipet up the cells and PBS into an eppendorf.

4. Spin down the cells (1400 rpm for 5 min), then aspirate off the PBS.

5. Resuspend pellet in lysis buffer (about 2-3X the size of the pellet), and let incubate on ice for 15 min. Vortex intermittently.

6. Store in the -80°C until use.

7. After thawing on ice, spin on high speed for 15 min, then use for protein concentration quantification.

BCA Assay (Lowry) - Biorad reagents

1. Pipet 5 μl of standard (between 2.5 and 0 μg/μl) and sample. Note: Westerns - protein samples in duplicate, Seahorse - protein in singles (2.5, 2.0, 1.5, 1.0, 0.75, 0.5, 0 μg/μl for standard curve.)

(Western samples dilute 1:5 (1 in 5 total)) (Seahorse sample use at full concentration.)

2. Add 20 μl of Reagent S to each ml of Reagent A, then add 25 μl to each well.

3. Add 200 μl of Reagent B to each well.

4. Let sit for 5-10 min then set up the plate reader. Read absorbance at 750 nm (but 595 nm is ok too as long as the curve is linear).

Bradford Assay - Biorad reagents

1. Pipet 10 μl of standard (between 1 and 0 μg/μl) and sample. (1, 0.5, 0.25, 0.125, 0.0625, 0 μg/μl for standard curve.)

(Western samples dilute (5 in 10 total), or (2 in 10 total) depending on how concentrated the samples are.

2. Mix Biorad protein assay dye reagent concentrate 1:4 in water.

3. Add 200 μl of the dye and water mixture to each well.

4. Let sit for 5-10 min then set up the plate reader. Read absorbance at 595 nm.

CHAPTER B. Western Blot Protocol

Western Protocol

Day 1

1. Make cell lysates (see protein lysis protocol). When removing from the -80°C, let thaw on ice. Excess heat will increase protein degradation.

Keep protein lysates on ice. Remove lysis buffer with inhibitors to thaw on ice as well. This is used to equilibrate volumes between samples.

2. Measure protein concentration using BCA or Bradford kit. Run samples and standards in duplicate or triplicate. Protein samples are diluted to fit within the curve. If sample is predicted to have high concentration, dilute your sample 1:5. (Confluent 10 cm with 100 μl lysis –> try 1:4 dilution, tissue samples try 1:10 - will need to determine each independently to figure out the best for each cell type.)

3. Calculate amount of protein necessary for western, then normalize the volume by adding lysis buffer. Each antibody needs to be tested for the amount of protein necessary for desired level of signal. Pipet amount into eppendorf, lysis then protein (all on ice).

4. Set up 2X loading buffer by adding DTT (1:5, 50 ul DTT per 200 ul 2X LB). Add loading buffer at a 1:1 ratio to each protein sample. Vortex to mix, then boil for 5 minutes to denature the protein. Pulse the sample in the centrifuge to get all the sample into the bottom of the tube, then vortex to mix.

5. Set up acrylamide gel - percent is determined by the size of the protein of interest. Larger proteins want a lower percentage gel. If pouring a gel, the polymerization process takes about 60-90 minutes, so pour the resolving gel when removing lysates from the $-80°$C. Gels can be poured the day before, just keep at 4 degrees with running buffer to keep from drying out (I use 20 ml, with a paper towel wrapped around in a ziplock bag or plastic wrap).

8% - anything larger than 120 kDa

10% - 70-120 kDa

13% - 30-80 kDa

15% - smaller than 40 kDa

6. Put gels into the gel box setup (tall plate on the outside, comb on the inside). Align notches to reduce buffer from leaking out of the center between the gels. Add running buffer (1 Liter) to the center of the gels, then remove comb. Clean out each well using a syringe prior to adding sample. If leakage occurs buffer will need to be added to the center to maintain voltage through the gel, disruption will impede gel separation and cause proteins to diffuse in the gel.

7. Load samples into the gel with a protein ladder (10 μl is plenty, do not boil), then start running the current at 100 V until the dye front has entered into the resolving gel. After 30 minutes increase the voltage to 150 V until the desired separation has occurred. Align current such that red goes to red and black to black.

8. Once gel is running, set up the Transfer buffer, mix and store at 4°C to cool and degas (I place in the cold room). One + hour is sufficient.

9. To set up transfer (wet) place sponges, Whatman paper, membrane, cassette in transfer buffer. Remove gel from between the plates and place in transfer buffer to dilute out the SDS.

10. Arrange the cassette (black part) in transfer buffer (covered), then add 1 sponge, 1 whatman paper, the gel, membrane, 1 whatman, 1 sponge. In between each layer roll out bubbles that could interfere with the transfer. Close the cassette and slide lever to lock.

(Looking down from the top after assembly) Clear cassette side Sponge Whatman Paper Membrane Gel Whatman paper Sponge Black cassette edge

11. Once assembled, place cassettes in the transfer box (red/black holder) black facing black. Put cold pack in the box and add all the buffer (minus the amount used to wash the gels). Take the box to the cold room and plug in to the power supply.

12. Transfer for 75 minutes at 100 V. (For large proteins use overnight transfer set up at 30 V.) Set up blocking buffer (3% BSA in TBS - 1 gm in 30 ml). It is important to transfer

in the cold to prevent the buffer from getting too hot and reducing the efficiency of the transfer.

13. Retrieve gel box from the cold room, open cassette and take out membrane. Place membrane in blocking buffer (3% BSA in TBS (can use 10x PBS instead of TBS)). Block membrane for 1 hour. Membranes should show the marker as a marker for a positive transfer. 8% gels rarely show the marker, so to check the efficiency of the transfer the blot can be stained with ponceau. Wash with TBS (no tween) to remove the stain.

14. Make up antibody dilutions in blocking buffer, just enough to cover the blot and keep it from drying out (3-5 ml depending on the size of the box). Add antibody to blots and rotate in cold room overnight.

Day 2

1. Take blots out of cold room and drain off antibody into the sink. Then add fresh TBST (I start with 0.05% tween in my TBS), drain off and then add more TBST and let rotate. Washes should be about 10 minutes each.

2. Repeat washes 2 more times (total of 3 washes). During the second wash make up 5% milk in TBST, vortex, and let rotate with the blots until milk is in solution.

3. Add secondary antibody to 5% milk at 1:5000. Drain off TBST and add secondary. Let rotate for 1 hour to 90 minutes.

4. Repeat washes with TBST (3X), with 10 minute washes.

5. Develop blots according to kit directions.

In general lay saran wrap flat on bench. Add solution 1 and 2 to edge of saran wrap (1 blot - 500 ul of each, amount dependent on size and number of blots) in separate piles (use separate tips to avoid contaminating and spoiling solutions). Take blots out of the tray, drain excess buffer on a kimwipe and place on saran wrap, marker side up. Mix solutions, then cover the blot. Wait 5 minutes. Drain off excess liquid using a kimwipe and place into a sleeve within the cassette. Take cassette, film, and a timer to the dark

room and expose blots to film. I start with a 15 second exposure, then a 2 minute. I adjust the exposure time after the film comes out of the developer.

Western Solutions

10x TBS (1 L)

80 gm NaCl (1.37 M)

2 gm KCl (27 mM)

30 gm Trizma Base (250 mM)

pH to 7.4 with HCl

10X Tris Glycine (1L)

30.3 gm Trizma Base

144.2 gm glycine

2X Loading Buffer (48 ml)

12 ml 0.5 M Tris pH 6.8 (100 mM)

24 ml 10% SDS (4

12 ml 100% Glycerol (20

Bromophenol Blue

Mix. Can stay at RT. Prior to use add DTT.

200 μl 100 mM DTT per 800 μl LB

Running Buffer

1X Tris-Glycine

10 ml 10% SDS

Water to 1L

Transfer Buffer

1X Tris-Glycine

200 ml Methanol

Water to 1L

CHAPTER C. PCR Protocol

TABLE C.1: cDNA Synthesis Reagent Volumes

High-Capacity cDNA Reverse Transcription Kits	
	1 Reaction
10x RT Buffer	2
25x dNTP Mix (100mM)	0.8
10x RT Random Primers	2
MultiScribe Reverse Transcriptase	1
Nuclease-free H2O	4.2
RNA sample	10
Total per reaction	20

TABLE C.2: cDNA Synthesis Thermocycle

Step	Temperature (°C)	Time
1	25	10 min
2	37	120 min
3	85	5 min
4	4	∞

TABLE C.3: PCR Reaction Reagent Volumes

SYBR Green template		
	1x (96well)	1x (384well)
Master mixture (Roche 04913850001)	12.5	6.25
Forward primer (10 uM)	0.75	0.375
Reverse pirmer (10 uM)	0.75	0.375
cDNA template (per well)	2	2
dH2O	9	1
Total	25	10

CHAPTER D. Stern-Volmer Code

```
r= size(INT, 1)
    for i= 1:size(INT,1)
    I1= ; <– (add in calibration intensity at 21%)
    X1 = 21;
    I2= ; <– (add in calibration intensity at 0%)
    X2=0;
    kt(i,1)= (I2-I1)/((X1*I1)-(X2*I2));
    I0(i,1)= (1+kt(i,1)*X1)*I1;
    x1 = 0:1:22;
    y1(i,:)= I0(i,1)./(1+kt(i,1)*x1);
    oxygenpercent(i,:) = ((I0(i,1)./INT(i,1))-1)/kt(i,1)
    hold on
    end
```

	Property	Name	Value	Unit	Property group
✓	Heat capacity at constant pressure	Cp	703[J/(kg*K)]	J/(kg·K)	Basic
✓	Density	rho	2203[kg/m^3]	kg/m³	Basic
✓	Thermal conductivity	k	1.38[W/(m*K)]	W/(m·K)	Basic
	Relative permeability	mur	1	1	Basic
	Electrical conductivity	sigma	1e-14[S/m]	S/m	Basic
	Coefficient of thermal expansion	alpha	0.55e-6[1/K]	1/K	Basic
	Relative permittivity	epsilonr	2.09	1	Basic
	Young's modulus	E	73.1e9[Pa]	Pa	Young's modulus and Poisson's ratio
	Poisson's ratio	nu	0.17	1	Young's modulus and Poisson's ratio
	Refractive index	n	1.45	1	Refractive index
	Refractive index, imaginary part	ki	0	1	Refractive index

FIGURE E.1: The material properties of the glass coverslips in the heat transfer simulation.

Property	Name	Value	Unit	Property group
Thermal conductivity	k	0.15^5	W/(m·K)	Basic
Density	rho	970^6	kg/m³	Basic
Heat capacity at constant pres...	Cp	1500^6	J/(kg·K)	Basic

FIGURE E.2: The material properties of the PDMS gaskets in the heat transfer simulation.

	Property	Name	Value	Unit	Property group
✓	Ratio of specific heats	gamma	1.0	1	Basic
✓	Heat capacity at constant pressure	Cp	Cp(T[1/K])[J/(kg*K)]	J/(kg·K)	Basic
✓	Density	rho	rho(T[1/K])[kg/m^3]	kg/m³	Basic
✓	Thermal conductivity	k	k(T[1/K])[W/(m*K)]	W/(m·K)	Basic
	Dynamic viscosity	mu	eta(T[1/K])[Pa*s]	Pa·s	Basic
	Electrical conductivity	sigma	5.5e-6[S/m]	S/m	Basic
	Speed of sound	c	cs(T[1/K])[m/s]	m/s	Basic

FIGURE E.3: The material properties of the cell culture media in the heat transfer simulation as modeled by water.

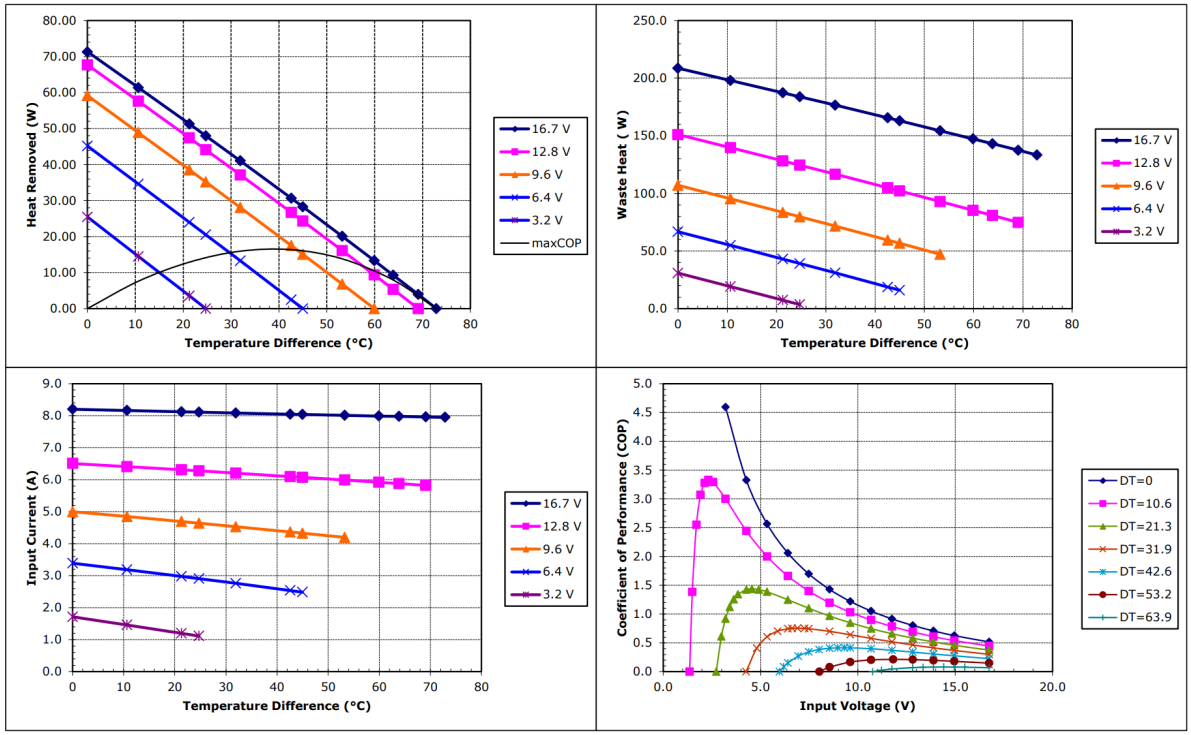

FIGURE F.1: The specifications of the peltier thermoelectric device, including the dependence of the heat removed, waste heat, current drawn, and the coefficient of performance on input voltage and the temperature difference between the hot and cold sides. Reproduced from the manufacturer, TE Technology, Inc.

CHAPTER G. Copyright Permissions Statement

Author reusing their own work published by the Royal Society of Chemistry

You do not need to request permission to reuse your own figures, diagrams, etc, that were originally published in a Royal Society of Chemistry publication. However, permission should be requested for use of the whole article or chapter except if reusing it in a thesis. If you are including an article or book chapter published by us in your thesis please ensure that your co-authors are aware of this.

Reuse of material that was published originally by the Royal Society of Chemistry must be accompanied by the appropriate acknowledgement of the publication. The form of the acknowledgement is dependent on the journal in which it was published originally, as detailed in 'Acknowledgements'.

The Royal Society of Chemistry publishes some journals in partnership with, or on behalf of, other organisations; these journals require a specific wording of the acknowledgement when work is reproduced from them. The text for the acknowledgement for these journals, and the standard wording to be used by all other journals are given below.

Standard acknowledgement

Reproduced from Ref. XX with permission from the Royal Society of Chemistry.

Non-standard acknowledgements

Reproduction of material from NJC (New Journal of Chemistry) Reproduced from Ref. XX with permission from the Centre National de la Recherche Scientifique (CNRS) and the Royal Society of Chemistry.

Reproduction of material from Photochemical Photobiological Sciences (PPS) Reproduced from Ref. XX with permission from the European Society for Photobiology, the European Photochemistry Association, and the Royal Society of Chemistry.

Reproduction of material from PCCP (Physical Chemistry Chemical Physics) Reproduced from Ref. XX with permission from the PCCP Owner Societies.

Reproduction of material from Inorganic Chemistry Frontiers Reproduced from Ref. XX with permission from the Chinese Chemical Society (CCS), Peking University (PKU), and the Royal Society of Chemistry.

Reproduction of material from Organic Chemistry Frontiers Reproduced from Ref. XX with permission from the Chinese Chemical Society (CCS), Shanghai Institute of Organic Chemistry (SIOC), and the Royal Society of Chemistry.

Reproduction of material from articles in the Journal Archive from Geochemical Transactions Reproduced from Ref. XX with permission from the American Chemical Society, Division of Geochemistry and the Royal Society of Chemistry.

CITED LITERATURE

[1] Megan L Rexius-Hall et al. "Microfluidic platform generates oxygen landscapes for localized hypoxic activation." In: *Lab on a chip* 14.24 (2014), pp. 4688–95. DOI: 10.1039/c4lc01168f.

[2] Martin D Brennan et al. "Oxygen control with microfluidics." In: *Lab on a chip* 14.22 (2014), pp. 4305–18. DOI: 10.1039/c4lc00853g.

[3] Shun-Pei Hung et al. "Hypoxia promotes proliferation and osteogenic differentiation potentials of human mesenchymal stem cells." In: *Journal of orthopaedic research : official publication of the Orthopaedic Research Society* 30.2 (Mar. 2012), pp. 260–266. DOI: 10.1002/jor.21517.

[4] Zoran Ivanovic. "Hypoxia or in situ normoxia: The stem cell paradigm." In: *Journal of cellular physiology* 219.2 (May 2009), pp. 271–275. DOI: 10.1002/jcp.21690.

[5] Gianluca D'Ippolito et al. "Low oxygen tension inhibits osteogenic differentiation and enhances stemness of human MIAMI cells." In: *Bone* 39.3 (Sept. 2006), pp. 513–522. DOI: 10.1016/j.bone.2006.02.061.

[6] Wolfgang K R Barnikol and Harald Pötzschke. "A novel, non-invasive diagnostic clinical procedure for the determination of an oxygenation status of chronic lower leg ulcers using peri-ulceral transcutaneous oxygen partial pressure measurements: results of its application in chronic venous insufficien". In: *German medical science : GMS e-journal* 10 (Jan. 2012), Doc11. DOI: 10.3205/000162.

[7] Christopher W Pugh and Peter J Ratcliffe. "Regulation of angiogenesis by hypoxia: role of the HIF system." In: *Nature medicine* 9.6 (2003), pp. 677–684. DOI: 10.1038/nm0603-677.

[8] G Ghosh et al. "Hypoxia-induced microRNA-424 expression in human endothelial cells regulates HIF-alpha isoforms and promotes angiogenesis". In: *J Clin Invest* 120.11 (2010), pp. 4141–4154. DOI: 10.1172/JCI42980DS1.

[9] Sally L. Dunwoodie. "The Role of Hypoxia in Development of the Mammalian Embryo". In: *Developmental Cell* 17.6 (2009), pp. 755–773. DOI: 10.1016/j.devcel.2009.11.008.

[10] M Celeste Simon and Brian Keith. "The role of oxygen availability in embryonic development and stem cell function." In: *Nature reviews. Molecular cell biology* 9.4 (2008), pp. 285–96. DOI: 10.1038/nrm2354.

[11] Ahmed Mohyeldin, Tomás Garzón-Muvdi, and Alfredo Quiñones-Hinojosa. "Oxygen in stem cell biology: a critical component of the stem cell niche." In: *Cell stem cell* 7.2 (Aug. 2010), pp. 150–161. DOI: 10.1016/j.stem.2010.07.007.

[12] Julie Mathieu et al. "Hypoxia induces re-entry of committed cells into pluripotency". In: *Stem Cells* 31.9 (2013), pp. 1737–1748. DOI: 10.1002/stem.1446. arXiv: NIHMS150003.

[13] Daniele M Gilkes, Gregg L Semenza, and Denis Wirtz. "Hypoxia and the extracellular matrix: drivers of tumour metastasis." In: *Nature reviews. Cancer* 14.6 (2014), pp. 430–9. DOI: 10.1038/nrc3726.

[14] P. Vaupel. "The Role of Hypoxia-Induced Factors in Tumor Progression". In: *The Oncologist* 9.suppl_5 (Nov. 2004), pp. 10–17. DOI: 10.1634/theoncologist.9-90005-10.

[15] G L Semenza. "Defining the role of hypoxia-inducible factor 1 in cancer biology and therapeutics". In: *Oncogene* 29.5 (2010), pp. 625–634. DOI: 10.1038/onc.2009.441.

[16] G-H Fong and K Takeda. "Role and regulation of prolyl hydroxylase domain proteins". In: *Cell Death and Differentiation* 15.4 (Apr. 2008), pp. 635–641. DOI: 10.1038/cdd.2008.10.

[17] E. Metzen and P. J. Ratcliffe. "HIF hydroxylation and cellular oxygen sensing". In: *Biological Chemistry* 385.3-4 (Jan. 2004), pp. 223–230. DOI: 10.1515/BC.2004.016.

[18] Rasheduzzaman Chowdhury et al. "The human oxygen sensing machinery and its manipulation". In: *Chemical Society Reviews* 37.7 (June 2008), p. 1308. DOI: 10.1039/b701676j.

[19] Cheng-Jun Hu et al. "Differential roles of hypoxia-inducible factor 1alpha (HIF-1alpha) and HIF-2alpha in hypoxic gene regulation." In: *Molecular and cellular biology* 23.24 (Dec. 2003), pp. 9361–74. DOI: 10.1128/mcb.23.24.9361-9374.2003.

[20] S A Patel and M C Simon. "Biology of hypoxia-inducible factor-2alpha in development and disease." In: *Cell death and differentiation* 15.4 (Apr. 2008), pp. 628–34. DOI: 10.1038/cdd.2008.17.

[21] Tokujiro Uchida et al. "Prolonged hypoxia differentially regulates hypoxia-inducible factor (HIF)-1α and HIF-2α expression in lung epithelial cells: Implication of natural antisense HIF-1α". In: *Journal of Biological Chemistry* 279.15 (2004), pp. 14871–14878. DOI: 10.1074/jbc.M400461200.

[22] Brian Keith, Randall S Johnson, and M Celeste Simon. "HIF1α and HIF2α: sibling rivalry in hypoxic tumour growth and progression." In: *Nature reviews. Cancer* 12.1 (Dec. 2011), pp. 9–22. DOI: 10.1038/nrc3183.

[23] S Lee et al. "Nuclear/cytoplasmic localization of the von Hippel-Lindau tumor suppressor gene product is determined by cell density." In: *Proceedings of the National Academy of Sciences of the United States of America* 93.5 (Mar. 1996), pp. 1770–5.

[24] Isabelle Groulx and Stephen Lee. "Oxygen-dependent ubiquitination and degradation of hypoxia-inducible factor requires nuclear-cytoplasmic trafficking of the

von Hippel-Lindau tumor suppressor protein." In: *Molecular and cellular biology* 22.15 (Aug. 2002), pp. 5319–36. DOI: 10.1128/mcb.22.15.5319-5336.2002.

[25] Michael J Gray et al. "HIF-1α, STAT3, CBP/p300 and Ref-1/APE are components of a transcriptional complex that regulates Src-dependent hypoxia-induced expression of VEGF in pancreatic and prostate carcinomas". In: *Oncogene* 24.19 (Apr. 2005), pp. 3110–3120. DOI: 10.1038/sj.onc.1208513.

[26] Rachida S Belaiba et al. "Hypoxia up-regulates hypoxia-inducible factor-1alpha transcription by involving phosphatidylinositol 3-kinase and nuclear factor kappaB in pulmonary artery smooth muscle cells." In: *Molecular biology of the cell* 18.12 (Dec. 2007), pp. 4691–7. DOI: 10.1091/mbc.E07-04-0391.

[27] Haixia Gong et al. "HIF2?? signaling inhibits adherens junctional disruption in acute lung injury". In: *Journal of Clinical Investigation* 125.2 (2015), pp. 652–664. DOI: 10.1172/JCI77701.

[28] Brooke M Emerling et al. "PTEN regulates p300-dependent hypoxia-inducible factor 1 transcriptional activity through Forkhead transcription factor 3a (FOXO3a)." In: *Proceedings of the National Academy of Sciences of the United States of America* 105.7 (Feb. 2008), pp. 2622–7. DOI: 10.1073/pnas.0706790105.

[29] P J Lee et al. "Hypoxia-inducible factor-1 mediates transcriptional activation of the heme oxygenase-1 gene in response to hypoxia." In: *The Journal of biological chemistry* 272.9 (Feb. 1997), pp. 5375–81. DOI: 10.1074/JBC.272.9.5375.

[30] Matthew R Pawlus et al. "Upstream stimulatory factor 2 and hypoxia-inducible factor 2α (HIF2α) cooperatively activate HIF2 target genes during hypoxia." In: *Molecular and cellular biology* 32.22 (Nov. 2012), pp. 4595–610. DOI: 10.1128/MCB.00724-12.

[31] G. Bellot et al. "Hypoxia-Induced Autophagy Is Mediated through Hypoxia-Inducible Factor Induction of BNIP3 and BNIP3L via Their BH3 Domains". In: *Molecular and Cellular Biology* 29.10 (May 2009), pp. 2570–2581. DOI: 10.1128/MCB.00166-09.

[32] Elisa Conde et al. "Hypoxia Inducible Factor 1-Alpha (HIF-1 Alpha) Is Induced during Reperfusion after Renal Ischemia and Is Critical for Proximal Tubule Cell Survival". In: *PLoS ONE* 7.3 (Mar. 2012). Ed. by Emmanuel A. Burdmann, e33258. DOI: 10.1371/journal.pone.0033258.

[33] Xuanchun Wang et al. "Insulin Downregulates the Transcriptional Coregulator CITED2, an Inhibitor of Proangiogenic Function in Endothelial Cells". In: *Diabetes* 65.12 (2016).

[34] Longbo Zhang et al. "Hypoxia-inducible factor-1a contributes to dendritic overgrowth in tuberous sclerosis". In: *Neuroscience Letters* 612 (Jan. 2016), pp. 43–47. DOI: 10.1016/j.neulet.2015.11.038.

[35] A. Kuschel, P. Simon, and S. Tug. "Functional regulation of HIF-1α under normoxia-is there more than post-translational regulation?" In: *Journal of Cellular Physiology* 227.2 (Feb. 2012), pp. 514–524. DOI: 10.1002/jcp.22798.

[36] Agnes Görlach. "Regulation of HIF-1alpha at the transcriptional level." In: *Current pharmaceutical design* 15.33 (2009), pp. 3844–52.

[37] Kyung Jin Woo et al. "Desferrioxamine, an iron chelator, enhances HIF-1α accumulation via cyclooxygenase-2 signaling pathway". In: *Biochemical and Biophysical Research Communications* 343.1 (2006), pp. 8–14. DOI: 10.1016/j.bbrc.2006.02.116.

[38] Anastasia Triantafyllou et al. "Cobalt induces hypoxia-inducible factor-1α (HIF-1α) in HeLa cells by an iron-independent, but ROS-, PI-3K- and MAPK-dependent mechanism". In: *Free Radical Research* 40.8 (Jan. 2006), pp. 847–856. DOI: 10.1080/10715760600730810.

[39] Vasantha Kumar Bhaskara et al. "Intermittent hypoxia regulates stem-like characteristics and differentiation of neuroblastoma cells." In: *PloS one* 7.2 (Jan. 2012), e30905. DOI: 10.1371/journal.pone.0030905.

[40] Mingli Han et al. "MiR-21 regulates epithelial-mesenchymal transition phenotype and hypoxia-inducible factor-1α expression in third-sphere forming breast cancer stem cell-like cells." In: *Cancer science* 103.6 (June 2012), pp. 1058–1064. DOI: 10.1111/j.1349-7006.2012.02281.x.

[41] Lynn A Dudash et al. "Endothelial cell attachment and shear response on biomimetic polymer-coated vascular grafts." In: *Journal of biomedical materials research. Part A* 100.8 (Aug. 2012), pp. 2204–2210. DOI: 10.1002/jbm.a.34119.

[42] Chih-Wen Ni, Haiwei Qiu, and Hanjoong Jo. "MicroRNA-663 upregulated by oscillatory shear stress plays a role in inflammatory response of endothelial cells." In: *American journal of physiology. Heart and circulatory physiology* 300.5 (May 2011), H1762–9. DOI: 10.1152/ajpheart.00829.2010.

[43] Syotaro Obi et al. "Differentiation of circulating endothelial progenitor cells induced by shear stress". In: *2012 International Symposium on Micro-NanoMechatronics and Human Science (MHS)*. IEEE, Apr. 2012, pp. 54–58. ISBN: 978-1-4673-4813-3. DOI: 10.1109/MHS.2012.6492452.

[44] S G Charati and S A Stern. "Diffusion of Gases in Silicone Polymers: Molecular Dynamics Simulations". In: *Macromolecules* 31.16 (Aug. 1998), pp. 5529–5535. DOI: 10.1021/ma980387e.

[45] Min-Cheol Kim et al. "Mathematical analysis of oxygen transfer through polydimethylsiloxane membrane between double layers of cell culture channel and gas chamber in microfluidic oxygenator". In: *Microfluidics and Nanofluidics* 15.3 (Feb. 2013), pp. 285–296. DOI: 10.1007/s10404-013-1142-8.

[46] Mark Polinkovsky et al. "Fine temporal control of the medium gas content and acidity and on-chip generation of series of oxygen concentrations for cell cultures." In: *Lab on a chip* 9.8 (Apr. 2009), pp. 1073–1084. DOI: 10.1039/b816191g.

[47] Ludwig Wilhelm Winkler and Richard Charles Whaley. *The determination of dissolved oxygen in water*. 1888.

[48] J R Clark Leland C. et al. "Continuous Recording of Blood Oxygen Tensions by Polarography". In: *J Appl Physiol* 6.3 (Sept. 1953), pp. 189–193.

[49] Raymond H W Lam, Min-Cheol Kim, and Todd Thorsen. "Culturing aerobic and anaerobic bacteria and mammalian cells with a microfluidic differential oxygenator." In: *Analytical chemistry* 81.14 (July 2009), pp. 5918–5924. DOI: 10.1021/ac9006864.

[50] Joseph R Lakowicz. *Principles of Fluorescence Spectroscopy Principles of Fluorescence Spectroscopy*. 2006. ISBN: 978-0-387-31278-1 (Print) 978-0-387-46312-4 (Online). DOI: 10.1007/978-0-387-46312-4.

[51] C Holleyman, D Larson, and K Hunter. "Simulation of ischemic reperfusion in endothelial cell culture increases apoptosis." In: *The Journal of extra-corporeal technology* 33.3 (Sept. 2001), pp. 175–180.

[52] L Wyld, M W Reed, and N J Brown. "The influence of hypoxia and pH on aminolaevulinic acid-induced photodynamic therapy in bladder cancer cells in vitro." In: *British journal of cancer* 77.10 (May 1998), pp. 1621–1627.

[53] Samantha Grist et al. "Microfluidic cell culture systems with integrated sensors for drug screening". In: *SPIE MOEMS-MEMS*. Ed. by Holger Becker and Bonnie L Gray. International Society for Optics and Photonics, Feb. 2012, p. 825103. DOI: 10.1117/12.911427.

[54] Eric Leclerc, Yasuyuki Sakai, and Teruo Fujii. "Microfluidic PDMS (polydimethylsiloxane) bioreactor for large-scale culture of hepatocytes." In: *Biotechnology progress* 20.3 (), pp. 750–755. DOI: 10.1021/bp0300568.

[55] Adam P Vollmer et al. "Development of an integrated microfluidic platform for dynamic oxygen sensing and delivery in a flowing medium." In: *Lab on a chip* 5.10 (Oct. 2005), pp. 1059–1066. DOI: 10.1039/b508097e.

[56] Micha Adler et al. "Generation of oxygen gradients with arbitrary shapes in a microfluidic device." In: *Lab on a chip* 10.3 (Feb. 2010), pp. 388–391. DOI: 10.1039/b920401f.

[57] Shawn C Oppegard et al. "Modulating temporal and spatial oxygenation over adherent cellular cultures." In: *PloS one* 4.9 (Jan. 2009), e6891. DOI: 10.1371/journal.pone.0006891.

[58] Shawn C Oppegard et al. "Precise control over the oxygen conditions within the Boyden chamber using a microfabricated insert." In: *Lab on a chip* 10.18 (Sept. 2010), pp. 2366–2373. DOI: 10.1039/c004856a.

[59] Hasan E Abaci et al. "Microbioreactors to manipulate oxygen tension and shear stress in the microenvironment of vascular stem and progenitor cells." In: *Biotechnology and applied biochemistry* 59.2 (2012), pp. 97–105. DOI: 10.1002/bab.1010.

[60] Kenichi Funamoto et al. "A novel microfluidic platform for high-resolution imaging of a three-dimensional cell culture under a controlled hypoxic environment." In: *Lab on a chip* 12.22 (Nov. 2012), pp. 4855–4863. DOI: 10.1039/c2lc40306d.

[61] J M Higgins et al. "Sickle cell vasoocclusion and rescue in a microfluidic device." In: *Proceedings of the National Academy of Sciences of the United States of America* 104.51 (Dec. 2007), pp. 20496–20500. DOI: 10.1073/pnas.0707122105.

[62] Joe F Lo et al. "Microfluidic wound bandage: localized oxygen modulation of collagen maturation." In: *Wound repair and regeneration : official publication of the Wound Healing Society [and] the European Tissue Repair Society* 21.2 (2013), pp. 226–34. DOI: 10.1111/wrr.12021.

[63] Xin Cui et al. "Microfluidic long-term differential oxygenation for bacterial growth characteristics analyses". In: *RSC Advances* 4.32 (Apr. 2014), p. 16662. DOI: 10.1039/c4ra01577k.

[64] David K Wood et al. "A biophysical indicator of vaso-occlusive risk in sickle cell disease." In: *Science translational medicine* 4.123 (Feb. 2012), 123ra26. DOI: 10.1126/scitranslmed.3002738.

[65] Gerardo Mauleon, Christopher P Fall, and David T Eddington. "Precise spatial and temporal control of oxygen within in vitro brain slices via microfluidic gas channels." In: *PloS one* 7.8 (Jan. 2012), e43309. DOI: 10.1371/journal.pone.0043309.

[66] Gerardo Mauleon et al. "Enhanced loading of Fura-2/AM calcium indicator dye in adult rodent brain slices via a microfluidic oxygenator." In: *Journal of neuroscience methods* 216.2 (June 2013), pp. 110–117. DOI: 10.1016/j.jneumeth.2013.04.007.

[67] Amy G Tsai et al. "Microvascular and tissue oxygen gradients in the rat mesentery". In: 95 (1998), pp. 6590–6595.

[68] BRIAN R. DULING and ROBERT M. BERNE. "Longitudinal Gradients in Periarteriolar Oxygen Tension". In: *Circulation Research* 27.5 (1970).

[69] A. G. TSAI, P. C. JOHNSON, and M. INTAGLIETTA. "Oxygen Gradients in the Microcirculation". In: *Physiological Reviews* 83.3 (2003), pp. 933–963. DOI: 10.1152/physrev.00034.2002.

[70] R N Pittman. "Oxygen gradients in the microcirculation." In: *Acta physiologica (Oxford, England)* 202.3 (July 2011), pp. 311–22. DOI: 10.1111/j.1748-1716.2010.02232.x.

[71] Roland Pittman. "Oxygen Transport and Exchange in the Microcirculation". In: *Microcirculation* 12.1 (Feb. 2005), pp. 59–70. DOI: 10.1080/10739680590895064.

[72] R. N. Pittman. "Oxygen gradients in the microcirculation". In: *Acta Physiologica* 202.3 (July 2011), pp. 311–322. DOI: 10.1111/j.1748-1716.2010.02232.x.

[73] Micha Adler et al. "Studies of bacterial aerotaxis in a microfluidic device." In: *Lab on a chip* 12.22 (Nov. 2012), pp. 4835–4847. DOI: 10.1039/c2lc21006a.

[74] Joe F Lo, Elly Sinkala, and David T Eddington. "Oxygen gradients for open well cellular cultures via microfluidic substrates." In: *Lab on a chip* 10.18 (Sept. 2010), pp. 2394–2401. DOI: 10.1039/c004660d.

[75] Jared W Allen and Sangeeta N Bhatia. "Formation of steady-state oxygen gradients in vitro: application to liver zonation." In: *Biotechnology and bioengineering* 82.3 (May 2003), pp. 253–262. DOI: 10.1002/bit.10569.

[76] Jared W Allen, Salman R Khetani, and Sangeeta N Bhatia. "In vitro zonation and toxicity in a hepatocyte bioreactor." In: *Toxicological sciences : an official journal of the Society of Toxicology* 84.1 (Mar. 2005), pp. 110–119. DOI: 10.1093/toxsci/kfi052.

[77] Maciej Skolimowski et al. "Microfluidic dissolved oxygen gradient generator biochip as a useful tool in bacterial biofilm studies." In: *Lab on a chip* 10.16 (Aug. 2010), pp. 2162–2169. DOI: 10.1039/c003558k.

[78] Yung-Ann Chen et al. "Generation of oxygen gradients in microfluidic devices for cell culture using spatially confined chemical reactions." In: *Lab on a chip* 11.21 (Nov. 2011), pp. 3626–3633. DOI: 10.1039/c1lc20325h.

[79] Lei Wang et al. "Construction of oxygen and chemical concentration gradients in a single microfluidic device for studying tumor cell-drug interactions in a dynamic hypoxia microenvironment." In: *Lab on a chip* 13.4 (Feb. 2013), pp. 695–705. DOI: 10.1039/c2lc40661f.

[80] W T Coakley. "Hyperthermia effects on the cytoskeleton and on cell morphology." In: *Symposia of the Society for Experimental Biology* 41 (1987), pp. 187–211.

[81] P A Almeida and V N Bolton. "The effect of temperature fluctuations on the cytoskeletal organisation and chromosomal constitution of the human oocyte." In: *Zygote (Cambridge, England)* 3.4 (Nov. 1995), pp. 357–65.

[82] Hiroyuki Suzuki, Tomomi Kumai, and Masatoshi Matsuzaki. "Effect of Temperature Decline on the Cytoskeletal Organization of the Porcine Oocyte". In: *Journal of Mammalian Ova Research* 24.3 (Oct. 2007), pp. 107–113. DOI: 10.1274/jmor.24.107.

[83] Guilhem Velve-Casquillas et al. "A fast microfluidic temperature control device for studying microtubule dynamics in fission yeast." In: *Methods in cell biology* 97 (2010), pp. 185–201. DOI: 10.1016/S0091-679X(10)97011-8.

[84] J. G. Moner and R. O. Berger. "RNA synthesis and cell division in cold-synchronized cells ofTetrahymena pyriformis". In: *Journal of Cellular Physiology* 67.2 (Apr. 1966), pp. 217–223. DOI: 10.1002/jcp.1040670203.

[85] Don Moir et al. "COLD-SENSITIVE CELL-DIVISION-CYCLE MUTANTS OF YEAST: ISOLATION, PROPERTIES, AND PSEUDOREVERSION STUDIES". In: *Genetics* 100.4 (1982).

[86] Shintaro Imamura, Nobuhiko Ojima, and Michiaki Yamashita. "Cold-inducible expression of the cell division cycle gene CDC48 and its promotion of cell proliferation during cold acclimation in zebrafish cells ¹". In: *FEBS Letters* 549.1-3 (Aug. 2003), pp. 14–20. DOI: 10.1016/S0014-5793(03)00723-3.

[87] Conly L Rieder and Richard W Cole. "Cold-shock and the Mammalian cell cycle." In: *Cell cycle (Georgetown, Tex.)* 1.3 (), pp. 169–75.

[88] J L KAVANAU. "Enzyme kinetics and the rate of biological processes." In: *The Journal of general physiology* 34.2 (Nov. 1950), pp. 193–209.

[89] Sylvie Breton and Dennis Brown. "Cold-Induced Microtubule Disruption and Relocalization of Membrane Proteins in Kidney Epithelial Cells". In: ().

[90] Andrea Baruchin et al. "Effects of Cold Exposure on Rat Adrenal Tyrosine Hydroxylase: An Analysis of RNA, Protein, Enzyme Activity, and Cofactor Levels". In: *Journal of Neurochemistry* 54.5 (May 1990), pp. 1769–1775. DOI: 10.1111/j.1471-4159.1990.tb01232.x.

[91] Alex G. Little and Frank Seebacher. "Thermal conditions experienced during differentiation affect metabolic and contractile phenotypes of mouse myotubes". In: *American Journal of Physiology - Regulatory, Integrative and Comparative Physiology* 311.3 (2016).

[92] Verena Albert et al. "mTORC2 sustains thermogenesis via Akt-induced glucose uptake and glycolysis in brown adipose tissue." In: *EMBO molecular medicine* 8.3 (Mar. 2016), pp. 232–46. DOI: 10.15252/emmm.201505610.

[93] D C Greenway and J Himms-Hagen. "Increased calcium uptake by muscle mitochondria of cold-acclimated rats." In: *The American journal of physiology* 234.1 (Jan. 1978), pp. C7–13.

[94] K. Suto and H. Gotoh. "Calcium signaling in cold cells studied in cultured dorsal root ganglion neurons". In: *Neuroscience* 92.3 (June 1999), pp. 1131–1135. DOI: 10.1016/S0306-4522(99)00063-9.

[95] Nicholas M Teets et al. "Calcium signaling mediates cold sensing in insect tissues." In: *Proceedings of the National Academy of Sciences of the United States of America* 110.22 (May 2013), pp. 9154–9. DOI: 10.1073/pnas.1306705110.

[96] David Julius et al. "The capsaicin receptor: a heat-activated ion channel in the pain pathway". In: *Nature* 389.6653 (Oct. 1997), pp. 816–824. DOI: 10.1038/39807.

[97] David Julius et al. "A capsaicin-receptor homologue with a high threshold for noxious heat". In: *Nature* 398.6726 (Apr. 1999), pp. 436–441. DOI: 10.1038/18906.

[98] Andrea M. Peier et al. "A Heat-Sensitive TRP Channel Expressed in Keratinocytes". In: *Science* 296.5575 (2002).

[99] Ali Deniz Güler et al. "Heat-Evoked Activation of the Ion Channel, TRPV4". In: *Journal of Neuroscience* 22.15 (2002).

[100] David D. McKemy, Werner M. Neuhausser, and David Julius. "Identification of a cold receptor reveals a general role for TRP channels in thermosensation". In: *Nature* 416.6876 (Mar. 2002), pp. 52–58. DOI: 10.1038/nature719.

[101] Shuangtao Ma et al. "Activation of the cold-sensing TRPM8 channel triggers UCP1-dependent thermogenesis and prevents obesity". In: *Journal of Molecular Cell Biology* 4.2 (Apr. 2012), pp. 88–96. DOI: 10.1093/jmcb/mjs001.

[102] Guilhem Velve-Casquillas et al. "Microfluidic tools for cell biological research." In: *Nano today* 5.1 (Feb. 2010), pp. 28–47. DOI: 10.1016/j.nantod.2009.12.001.

[103] Elena M Lucchetta et al. "Dynamics of Drosophila embryonic patterning network perturbed in space and time using microfluidics." In: *Nature* 434.7037 (Apr. 2005), pp. 1134–8. DOI: 10.1038/nature03509.

[104] Thomas M. Pearce et al. "Integrated microelectrode array and microfluidics for temperature clamp of sensory neurons in culture". In: *Lab on a Chip* 5.1 (Dec. 2005), p. 97. DOI: 10.1039/b407871c.

[105] Chuanhai Fu et al. "Phospho-regulated interaction between kinesin-6 Klp9p and microtubule bundler Ase1p promotes spindle elongation." In: *Developmental cell* 17.2 (Aug. 2009), pp. 257–67. DOI: 10.1016/j.devcel.2009.06.012.

[106] Alex Groisman et al. "A microfluidic chemostat for experiments with bacterial and yeast cells". In: *Nature Methods* 2.9 (Sept. 2005), pp. 685–689. DOI: 10.1038/nmeth784.

[107] Chunsun Zhang et al. "PCR microfluidic devices for DNA amplification". In: *Biotechnology Advances* 24.3 (May 2006), pp. 243–284. DOI: 10.1016/j.biotechadv.2005.10.002.

[108] Qingqing Cao, Min-Cheol Kim, and Catherine Klapperich. "Plastic microfluidic chip for continuous-flow polymerase chain reaction: simulations and experiments." In: *Biotechnology journal* 6.2 (Feb. 2011), pp. 177–84. DOI: 10.1002/biot.201000100.

[109] JC Peltier. "Nouvelles experiences sur la caloricite des courants electrique". In: *Ann. Chim. Phys* 56.371 (1834), p. 371.

[110] Thomas Johann Seebeck. "Ueber die magnetische Polarisation der Metalle und Erze durch Temperaturdifferenz". In: *Annalen der Physik* 82.3 (1826), pp. 253–286.

[111] M. Miranda et al. "Spectroscopic evidence of anthropogenic compounds extraction from polymers by fluorescent dissolved organic matter in natural water". In: *Journal of the European Optical Society: Rapid Publications* 11.0 (Apr. 2016), p. 16014. DOI: 10.2971/jeos.2016.16014.

[112] George Maltezos, Matthew Johnston, and Axel Scherer. "Thermal management in microfluidics using micro-Peltier junctions". In: *Applied Physics Letters* 87.15 (Oct. 2005), p. 154105. DOI: 10.1063/1.2089174.

[113] BARBARA CANNON and JAN NEDERGAARD. "Brown Adipose Tissue: Function and Physiological Significance". In: *Physiological Reviews* 84.1 (2004).

[114] Miroslava Cedikova et al. "Mitochondria in White, Brown, and Beige Adipocytes". In: *Stem Cells International* 2016 (Mar. 2016), pp. 1–11. DOI: 10.1155/2016/6067349.

[115] Joan Sanchez-Gurmaches et al. "PTEN Loss in the Myf5 Lineage Redistributes Body Fat and Reveals Subsets of White Adipocytes that Arise from Myf5 Precursors". In: *Cell Metabolism* 16.3 (Sept. 2012), pp. 348–362. DOI: 10.1016/j.cmet.2012.08.003.

[116] Vivian Peirce, Stefania Carobbio, and Antonio Vidal-Puig. "The different shades of fat". In: *Nature* 510.7503 (June 2014), pp. 76–83. DOI: 10.1038/nature13477.

[117] M. E. Lidell, M. J. Betz, and S. Enerbäck. "Brown adipose tissue and its therapeutic potential". In: *Journal of Internal Medicine* 276.4 (Oct. 2014), pp. 364–377. DOI: 10.1111/joim.12255.

[118] Paul D. Boyer. "the Atp Synthase—a Splendid Molecular Machine". In: *Annual Review of Biochemistry* 66.1 (1997), pp. 717–749. DOI: 10.1146/annurev.biochem.66.1.717.

[119] Joachim Weber and Alan E. Senior. "ATP synthesis driven by proton transport in F1F0-ATP synthase". In: *FEBS Letters* 545.1 (2003), pp. 61–70. DOI: 10.1016/S0014-5793(03)00394-6.

[120] H Engel et al. "Whole-body PET: physiological and artifactual fluorodeoxyglucose accumulations." In: *Journal of nuclear medicine : official publication, Society of Nuclear Medicine* 37.3 (Mar. 1996), pp. 441–6.

[121] R L Wahl et al. "The potential of 2-deoxy-2[18F]fluoro-D-glucose (FDG) for the detection of tumor involvement in lymph nodes." In: *Journal of nuclear medicine : official publication, Society of Nuclear Medicine* 31.11 (Nov. 1990), pp. 1831–5.

[122] S F Barrington and M N Maisey. "Skeletal muscle uptake of fluorine-18-FDG: effect of oral diazepam." In: *Journal of nuclear medicine : official publication, Society of Nuclear Medicine* 37.7 (July 1996), pp. 1127–9.

[123] Thomas F. Hany et al. "Brown adipose tissue: a factor to consider in symmetrical tracer uptake in the neck and upper chest region". In: *European Journal of Nuclear Medicine and Molecular Imaging* 29.10 (Oct. 2002), pp. 1393–1398. DOI: 10.1007/s00259-002-0902-6.

[124] Henry W D Yeung et al. "Patterns of (18)F-FDG uptake in adipose tissue and muscle: a potential source of false-positives for PET." In: *Journal of nuclear medicine : official publication, Society of Nuclear Medicine* 44.11 (Nov. 2003), pp. 1789–96.

[125] Jan Nedergaard, Tore Bengtsson, and Barbara Cannon. "Unexpected evidence for active brown adipose tissue in adult humans". In: *American Journal of Physiology - Endocrinology and Metabolism* 293.2 (2007).

[126] D G Nicholls and R M Locke. "Thermogenic mechanisms in brown fat." In: *Physiological reviews* 64.1 (Jan. 1984), pp. 1–64.

[127] Ajit S Divakaruni, Dickon M Humphrey, and Martin D Brand. "Fatty acids change the conformation of uncoupling protein 1 (UCP1)." In: *The Journal of biological chemistry* 287.44 (Oct. 2012), pp. 36845–53. DOI: 10.1074/jbc.M112.381780.

[128] Andriy Fedorenko et al. "Mechanism of fatty-acid-dependent UCP1 uncoupling in brown fat mitochondria." In: *Cell* 151.2 (Oct. 2012), pp. 400–13. DOI: 10.1016/j.cell.2012.09.010.

[129] Edward T. Chouchani et al. "Mitochondrial ROS regulate thermogenic energy expenditure and sulfenylation of UCP1". In: *Nature* 532.7597 (Mar. 2016), pp. 112–116. DOI: 10.1038/nature17399.

[130] L Ye et al. "Fat cells directly sense temperature to activate thermogenesis". In: *Proceedings of the National Academy of Sciences of the United States of America* 110.30 (2013), pp. 12480–12485. DOI: DOI10.1073/pnas.1310261110. arXiv: arXiv:1408.1149.

[131] N J Rothwell and M J Stock. "Luxuskonsumption, diet-induced thermogenesis and brown fat: the case in favour." In: *Clinical science (London, England : 1979)* 64.1 (Jan. 1983), pp. 19–23.

[132] Shingo Kajimura et al. "Initiation of myoblast to brown fat switch by a PRDM16 – C/EBP-β transcriptional complex". In: *Nature* 460.7259 (Aug. 2009), pp. 1154–1158. DOI: 10.1038/nature08262.

[133] D L Hansen et al. "Thermogenic effects of sibutramine in humans." In: *The American journal of clinical nutrition* 68.6 (Dec. 1998), pp. 1180–6.

[134] Eric Colman et al. "The FDA's Assessment of Two Drugs for Chronic Weight Management". In: *New England Journal of Medicine* 367.17 (Oct. 2012), pp. 1577–1579. DOI: 10.1056/NEJMp1211277.

[135] Kristin I. Stanford et al. "Brown adipose tissue regulates glucose homeostasis and insulin sensitivity". In: *Journal of Clinical Investigation* 123.1 (Jan. 2013), pp. 215–223. DOI: 10.1172/JCI62308.

[136] Xiaomeng Liu et al. "Brown adipose tissue transplantation improves whole-body energy metabolism". In: *Cell Research* 23.6 (June 2013), pp. 851–854. DOI: 10.1038/cr.2013.64.

[137] Helin Liu et al. "Intracellular Temperature Sensing : An Ultra-bright Luminescent Nanothermometer with Non- sensitivity to pH and Ionic Strength". In: *Nature Publishing Group* September (2015), pp. 1–8. DOI: 10.1038/srep14879.

[138] Sven Enerbäck et al. "Mice lacking mitochondrial uncoupling protein are cold-sensitive but not obese". In: *nature* 387.6628 (May 1997), pp. 90–94. DOI: 10.1038/387090a0.

[139] Zhiguo Zhang et al. "Berberine activates thermogenesis in white and brown adipose tissue." In: *Nature communications* 5 (2014), p. 5493. DOI: 10.1038/ncomms6493.

[140] Jozef Ukropec et al. "UCP1-independent thermogenesis in white adipose tissue of cold-acclimated Ucp1-/- mice." In: *The Journal of biological chemistry* 281.42 (Oct. 2006), pp. 31894–908. DOI: 10.1074/jbc.M606114200.

[141] B. Cousin et al. "Occurrence of brown adipocytes in rat white adipose tissue: molecular and morphological characterization". In: *Journal of Cell Science* 103.4 (1992).

[142] C Guerra et al. "Emergence of brown adipocytes in white fat in mice is under genetic control. Effects on body weight and adiposity." In: *Journal of Clinical Investigation* 102.2 (July 1998), pp. 412–420. DOI: 10.1172/JCI3155.

[143] Bingzhong Xue et al. "Transcriptional synergy and the regulation of Ucp1 during brown adipocyte induction in white fat depots." In: *Molecular and cellular biology* 25.18 (Sept. 2005), pp. 8311–22. DOI: 10.1128/MCB.25.18.8311-8322.2005.

[144] Daisuke Suzuki, Yoshiharu Murata, and Sen-Ichi Oda. "Changes in Ucp1, D2 (Dio2) and Glut4 (Slc2a4) mRNA Expression in Response to Short-Term Cold Exposure in the House Musk Shrew (Suncus murinus)". In: *Exp. Anim* 56.4 (2007), pp. 279–288.

[145] Jieun Lee, Jessica M. Ellis, and Michael J. Wolfgang. "Adipose Fatty Acid Oxidation Is Required for Thermogenesis and Potentiates Oxidative Stress-Induced Inflammation". In: *Cell Reports* 10.2 (Jan. 2015), pp. 266–279. DOI: 10.1016/j.celrep.2014.12.023.

[146] Lucia A. de Jesus et al. "The type 2 iodothyronine deiodinase is essential for adaptive thermogenesis in brown adipose tissue". In: *Journal of Clinical Investigation* 108.9 (Nov. 2001), pp. 1379–1385. DOI: 10.1172/JCI13803.

[147] Marco Rossato et al. "Human white adipocytes express the cold receptor TRPM8 which activation induces UCP1 expression, mitochondrial activation and heat production". In: *Molecular and Cellular Endocrinology* 383.1-2 (Mar. 2014), pp. 137–146. DOI: 10.1016/j.mce.2013.12.005.

[148] Annie Moisan et al. "White-to-brown metabolic conversion of human adipocytes by JAK inhibition." In: *Nature cell biology* 17.1 (Jan. 2015), pp. 57–67. DOI: 10.1038/ncb3075.

[149] S. B. Prusiner, B. Cannon, and O. Lindberg. "Oxidative Metabolism in Cells Isolated from Brown Adipose Tissue. 1. Catecholamine and Fatty Acid Stimulation of Respiration". In: *European Journal of Biochemistry* 6.1 (Oct. 1968), pp. 15–22. DOI: 10.1111/j.1432-1033.1968.tb00413.x.

[150] JAN NEDERGAARD, BARBARA CANNON, and OLOV LINDBERG. "Microcalorimetry of isolated mammalian cells". In: *Nature* 267.5611 (June 1977), pp. 518–520. DOI: 10.1038/267518a0.

[151] Nina Mohell, Jan Nedergaard, and Barbara Cannon. "Quantitative differentiation of α- and β-adrenergic respiratory responses in isolated hamster brown fat cells: Evidence for the presence of an α1-adrenergic component". In: *European Journal of Pharmacology* 93.3-4 (Sept. 1983), pp. 183–193. DOI: 10.1016/0014-2999(83)90136-X.

[152] A Matthias et al. "Thermogenic responses in brown fat cells are fully UCP1-dependent. UCP2 or UCP3 do not substitute for UCP1 in adrenergically or fatty scid-induced thermogenesis." In: *The Journal of biological chemistry* 275.33 (Aug. 2000), pp. 25073–81. DOI: 10.1074/jbc.M000547200.

[153] Susanne Keipert and Martin Jastroch. "Brite/beige fat and UCP1 — is it thermogenesis?" In: *Biochimica et Biophysica Acta (BBA) - Bioenergetics* 1837.7 (July 2014), pp. 1075–1082. DOI: 10.1016/j.bbabio.2014.02.008.

[154] Stefano Bartesaghi et al. "Thermogenic Activity of UCP1 in Human White Fat-Derived Beige Adipocytes". In: *Molecular Endocrinology* 29.1 (Jan. 2015), pp. 130–139. DOI: 10.1210/me.2014-1295.

[155] Jui-ming Yang, Haw Yang, and Liwei Lin. "Reveal Heterogeneous Local Thermogenesis in Living Cells". In: 6 (2011), pp. 5067–5071.

[156] Kohki Okabe et al. "fluorescence lifetime imaging microscopy". In: *Nature Communications* 3 (2012), pp. 705–709. DOI: 10.1038/ncomms1714.

[157] Shigeki Kiyonaka et al. "Genetically encoded fluorescent thermosensors visualize subcellular thermoregulation in living cells". In: 10.12 (2013). DOI: 10.1038/nmeth.2690.

[158] Satoshi Arai et al. "monitors intracellular temperature gradient †". In: *Chemical Communications* 51.0 (2015), pp. 8044–8047. DOI: 10.1039/C5CC01088H.

[159] Masahiro Nakano et al. "Genetically encoded ratiometric fluorescent thermometer with wide range and rapid response". In: (2017), pp. 1–14. DOI: 10.1371/journal.pone.0172344.

[160] Seiichi Uchiyama et al. "A cationic fl uorescent polymeric thermometer for the ratiometric sensing of intracellular temperature". In: (2015), pp. 4498–4506. DOI: 10.1039/c5an00420a.

[161] Masaaki K Sato et al. "Temperature Changes in Brown Adipocytes Detected with a Bimaterial Microcantilever". In: *Biophysj* 106.11 (2014), pp. 2458–2464. DOI: 10.1016/j.bpj.2014.04.044.

[162] Changling Wang et al. "Determining intracellular temperature at single-cell level by a novel thermocouple method." In: *Cell research* 21.10 (Oct. 2011), pp. 1517–9. DOI: 10.1038/cr.2011.117.

[163] Fan Yang et al. "Measurement of local temperature increments induced by cultured HepG2 cells with micro- thermocouples in a thermally stabilized system". In: *Scientific Reports* April (2017), pp. 1–12. DOI: 10.1038/s41598-017-01891-1.

[164] Rókus Kriszt et al. "Optical visualisation of thermogenesis in stimulated single-cell brown adipocytes." In: *Scientific reports* 7.1 (May 2017), p. 1383. DOI: 10.1038/s41598-017-00291-9.

[165] Bi-Chang Chen et al. "Lattice light-sheet microscopy: imaging molecules to embryos at high spatiotemporal resolution." In: *Science (New York, N.Y.)* 346.6208 (Oct. 2014), p. 1257998. DOI: 10.1126/science.1257998.

[166] Liang Gao et al. "Noninvasive imaging beyond the diffraction limit of 3D dynamics in thickly fluorescent specimens." In: *Cell* 151.6 (Dec. 2012), pp. 1370–85. DOI: 10.1016/j.cell.2012.10.008.

[167] Alex M. Valm et al. "Applying systems-level spectral imaging and analysis to reveal the organelle interactome". In: *Nature* 546.7656 (May 2017), pp. 162–167. DOI: 10.1038/nature22369.

[168] Simón Méndez-Ferrer et al. "Mesenchymal and haematopoietic stem cells form a unique bone marrow niche". In: *Nature* 466.7308 (Aug. 2010), pp. 829–834. DOI: 10.1038/nature09262.

[169] Keiyo Takubo et al. "Regulation of Glycolysis by Pdk Functions as a Metabolic Checkpoint for Cell Cycle Quiescence in Hematopoietic Stem Cells". In: *Cell Stem Cell* 12.1 (2013), pp. 49–61. DOI: https://doi.org/10.1016/j.stem.2012.10.011.

[170] Katrien De Bock et al. "Role of PFKFB3-Driven Glycolysis in Vessel Sprouting". In: *Cell* 154.3 (Aug. 2013), pp. 651–663. DOI: 10.1016/j.cell.2013.06.037.

[171] H Shibata et al. "Cold exposure reverses inhibitory effects of fasting on peripheral glucose uptake in rats." In: *The American journal of physiology* 257.1 Pt 2 (July 1989), R96–101.

[172] Janne Orava et al. “Blunted metabolic responses to cold and insulin stimulation in brown adipose tissue of obese humans”. In: *Obesity* 21.11 (Nov. 2013), pp. 2279–2287. DOI: 10.1002/oby.20456.

[173] Leslie A Rowland et al. “Uncoupling Protein 1 and Sarcolipin Are Required to Maintain Optimal Thermogenesis, and Loss of Both Systems Compromises Survival of Mice under Cold Stress.” In: *The Journal of biological chemistry* 290.19 (May 2015), pp. 12282–9. DOI: 10.1074/jbc.M115.637603.

[174] Alex J Hughes et al. “Single-cell western blotting”. In: *Nature Methods* 11.7 (June 2014), pp. 749–755. DOI: 10.1038/nmeth.2992.

[175] Christina Scheel et al. “Paracrine and Autocrine Signals Induce and Maintain Mesenchymal and Stem Cell States in the Breast”. In: *Cell* 145.6 (2011), pp. 926–940. DOI: 10.1016/j.cell.2011.04.029.

[176] Jeanine M.L. Roodhart et al. “Mesenchymal Stem Cells Induce Resistance to Chemotherapy through the Release of Platinum-Induced Fatty Acids”. In: *Cancer Cell* 20.3 (Sept. 2011), pp. 370–383. DOI: 10.1016/j.ccr.2011.08.010.

[177] Mercè Obach et al. “6-Phosphofructo-2-kinase (pfkfb3) gene promoter contains hypoxia-inducible factor-1 binding sites necessary for transactivation in response to hypoxia.” In: *The Journal of biological chemistry* 279.51 (Dec. 2004), pp. 53562–70. DOI: 10.1074/jbc.M406096200.

[178] Yiming Xu et al. “Endothelial PFKFB3 plays a critical role in angiogenesis.” In: *Arteriosclerosis, thrombosis, and vascular biology* 34.6 (June 2014), pp. 1231–9. DOI: 10.1161/ATVBAHA.113.303041.

[179] A Namiki et al. “Hypoxia induces vascular endothelial growth factor in cultured human endothelial cells.” In: *The Journal of biological chemistry* 270.52 (Dec. 1995), pp. 31189–95. DOI: 10.1074/JBC.270.52.31189.

[180] Sunyoung Lee et al. "Autocrine VEGF signaling is required for vascular homeostasis." In: *Cell* 130.4 (Aug. 2007), pp. 691–703. DOI: 10.1016/j.cell.2007.06.054.

[181] Khalid Al-Nedawi et al. "Endothelial expression of autocrine VEGF upon the uptake of tumor-derived microvesicles containing oncogenic EGFR." In: *Proceedings of the National Academy of Sciences of the United States of America* 106.10 (Mar. 2009), pp. 3794–9. DOI: 10.1073/pnas.0804543106.

[182] Min Xu et al. "An acetate switch regulates stress erythropoiesis." In: *Nature medicine* 20.9 (2014), pp. 1018–26. DOI: 10.1038/nm.3587. arXiv: NIHMS150003.

[183] Martin D. Brennan, Megan L. Rexius-Hall, and David T. Eddington. "A 3D-printed oxygen control insert for a 24-well plate". In: *PLoS ONE* 10.9 (2015), pp. 1–9. DOI: 10.1371/journal.pone.0137631.

[184] Joe F Lo et al. "Islet preconditioning via multimodal microfluidic modulation of intermittent hypoxia." In: *Analytical chemistry* 84.4 (Feb. 2012), pp. 1987–93. DOI: 10.1021/ac2030909.

[185] S. E. Taylor et al. "Differential sub-nuclear distribution of hypoxia-inducible factors (HIF)-1 and -2 alpha impacts on their stability and mobility". In: *Open Biology* 6.9 (2016), p. 160195. DOI: 10.1098/rsob.160195.

[186] Chung Ji Liu et al. "miR-31 ablates expression of the HIF regulatory factor FIH to activate the HIF pathway in head and neck carcinoma". In: *Cancer Research* 70.4 (2010), pp. 1635–1644. DOI: 10.1158/0008-5472.CAN-09-2291.

[187] G M Tannahill et al. "Succinate is an inflammatory signal that induces IL-1β through HIF-1α." In: *Nature* 496.7444 (2013), pp. 238–42. DOI: 10.1038/nature11986. arXiv: NIHMS150003.

[188] Jack L Arbiser. "Fumarate esters as angiogenesis inhibitors: key to action in psoriasis?" In: *The Journal of investigative dermatology* 131.6 (2011), pp. 1189–91. DOI: 10.1038/jid.2011.45.

[189] Hongfei Ge et al. "Elucidation of signaling and functional activities of an orphan GPCR, GPR81." In: *Journal of lipid research* 49.4 (2008), pp. 797–803. DOI: 10.1194/jlr.M700513-JLR200.

[190] Christina L. Roland et al. "Cell surface lactate receptor GPR81 is crucial for cancer cell survival". In: *Cancer Research* 74.18 (2014), pp. 5301–5310. DOI: 10.1158/0008-5472.CAN-14-0319.

[191] Weihai He et al. "Citric acid cycle intermediates as ligands for orphan G-protein-coupled receptors." In: *Nature* 429.6988 (2004), pp. 188–193. DOI: 10.1038/nature02488.

[192] Koen Brusselmans et al. "Hypoxia-inducible Factor-2?? (HIF-2??) Is Involved in the Apoptotic Response to Hypoglycemia but Not to Hypoxia". In: *Journal of Biological Chemistry* 276.42 (2001), pp. 39192–39196. DOI: 10.1074/jbc.C100428200.

[193] Rui Chen et al. "The acetate/ACSS2 switch regulates HIF-2 stress signaling in the tumor cell microenvironment". In: *PLoS ONE* 10.2 (2015). DOI: 10.1371/journal.pone.0116515.

[194] K S Chae et al. "Opposite functions of HIF-α isoforms in VEGF induction by TGF-β1 under non-hypoxic conditions." In: *Oncogene* 30.10 (2011), pp. 1213–1228. DOI: 10.1038/onc.2010.498.

[195] Raju R Raval et al. "Contrasting properties of hypoxia-inducible factor 1 (HIF-1) and HIF-2 in von Hippel-Lindau-associated renal cell carcinoma." In: *Molecular and cellular biology* 25.13 (2005), pp. 5675–86. DOI: 10.1128/MCB.25.13.5675-5686.2005.

[196] Takaaki Imamura et al. "NIH Public Access". In: *International Journal* 124.4 (2009), pp. 617–643. DOI: 10.1002/ijc.24032.HIF-1.

[197] Urszula Florczyk et al. “Opposite effects of HIF-1?? and HIF-2?? on the regulation of IL-8 expression in endothelial cells”. In: *Free Radical Biology and Medicine* 51.10 (2011), pp. 1882–1892. DOI: 10.1016/j.freeradbiomed.2011.08.023.

[198] Attila Szendrői et al. “Opposite prognostic roles of HIF1 a and HIF2 a expressions in bone metastatic clear cell renal cell cancer”. In: *Oncotarget* (2016). DOI: 10.18632/oncotarget.9669.

[199] Tim D Eubank et al. “Opposing roles for HIF-1alpha and HIF-2alpha in the regulation of angiogenesis by mononuclear phagocytes.” In: *Blood* 117.1 (2011), pp. 323–332. DOI: 10.1182/blood-2010-01-261792.

[200] Guillaume Baffou et al. “A critique of methods for temperature imaging in single cells”. In: *Nature Methods* 11.9 (Aug. 2014), pp. 899–901. DOI: 10.1038/nmeth.3073.

[201] Shigeki Kiyonaka et al. “Validating subcellular thermal changes revealed by fluorescent thermosensors”. In: *Nature Methods* 12.9 (Aug. 2015), pp. 801–802. DOI: 10.1038/nmeth.3548.

[202] Guillaume Baffou et al. “Reply to: "Validating subcellular thermal changes revealed by fluorescent thermosensors" and "The 105 gap issue between calculation and measurement in single-cell thermometry"”. In: *Nature Methods* 12.9 (Aug. 2015), pp. 803–803. DOI: 10.1038/nmeth.3552.

[203] Madoka Suzuki et al. “The 105 gap issue between calculation and measurement in single-cell thermometry”. In: *Nature Methods* 12.9 (Aug. 2015), pp. 802–803. DOI: 10.1038/nmeth.3551.

[204] ‡ Erik A. Johannessen † et al. “Micromachined Nanocalorimetric Sensor for Ultra-Low-Volume Cell-Based Assays”. In: (2002). DOI: 10.1021/AC011028B.

[205] Dallas G Clark, Menno Brinkman, and Sally D Neville. "Microcalorimetric measurements of heat production in brown adipocytes from control and cafeteria-fed rats". In: *Biochem. J* 235 (1986), pp. 337–342.

[206] Erik Steen Hansen and Jens Knudsen. "Parallel Measurements of Heat Production and Thermogenin Content in Brown Fat Cells during Cold Acclimation of Rats". In: *Bioscience Reports* 6.1 (1986).

[207] Naoki Inomata et al. "Pico calorimeter for detection of heat produced in an individual brown fat cell". In: *Applied Physics Letters* 100.15 (Apr. 2012), p. 154104. DOI: 10.1063/1.3701720.

[208] G. Kucsko et al. "Nanometre-scale thermometry in a living cell". In: *Nature* 500.7460 (July 2013), pp. 54–58. DOI: 10.1038/nature12373.

[209] Ken-ichi Inokuma et al. "Uncoupling Protein 1 Is Necessary for Norepinephrine-Induced Glucose Utilization in Brown Adipose Tissue". In: *Diabetes* 54.5 (2005).

[210] A Marette and L J Bukowiecki. "Noradrenaline stimulates glucose transport in rat brown adipocytes by activating thermogenesis. Evidence that fatty acid activation of mitochondrial respiration enhances glucose transport". In: *Biochemical Journal* 277.1 (1991).

[211] Barbara CANNON and Jan NEDERGAARD. "The Physiological Role of Pyruvate Carboxylation in Hamster Brown Adipose Tissue". In: *European Journal of Biochemistry* 94.2 (Mar. 1979), pp. 419–426. DOI: 10.1111/j.1432-1033.1979.tb12909.x.

[212] Pontus Boström et al. "A PGC1-α-dependent myokine that drives brown-fat-like development of white fat and thermogenesis." In: *Nature* 481.7382 (2012), pp. 463–8. DOI: 10.1038/nature10777.

[213] Thomas Tsiloulis and Matthew J. Watt. "Exercise and the Regulation of Adipose Tissue Metabolism". In: 2015, pp. 175–201. DOI: 10.1016/bs.pmbts.2015.06.016.

VITA

Megan L. Rexius
Bioengineering Department, University of Illinois at Chicago
Chicago, IL

Education

INSTITUTION AND LOCATION	DEGREE	YEAR(s)	FIELD OF STUDY
Boston University, Boston, Massachusetts	B.S.	2005-2009	Biomedical Engineering
Technische Universität Dresden, Dresden, Germany (study abroad semester)		Spring 2007	Biomedical Engineering
University of Illinois at Chicago, Chicago, Illinois	Ph.D.	2011-2017	Bioengineering

Research and Professional Experience

2007-2009 Research Assistant, College of Engineering, Boston University, Boston, MA

2009-2011 Associate Engineer, CFD Research Corporation, Huntsville, AL

2011-2017 Graduate Research Assistant, College of Engineering and College of Medicine, University of Illinois at Chicago, Chicago, IL

Awards and Honors

2005-09 Engineering Scholar College of Engineering Scholarship, Boston University, Boston, MA.

2006 Summer Term Alumni Research Scholars (STARS) Award, Boston University, Boston, MA.

2009 *Magna Cum Laude*, Boston University, Boston, MA.

2012 CCTS Predoctoral Support for Translational Research Award, University of Illinois at Chicago, Chicago, IL

2013 Chemical and Biological Microsystems Society Travel Grant, μTAS 2013 Conference, Freiburg, Germany

2016 Dean's Scholar Fellowship, University of Illinois at Chicago, Chicago, IL

2017 American Physiological Society Endocrinology and Metabolism Research Recognition Award, Experimental Biology 2017 Meeting, Chicago, IL

Professional Memberships

2007-present	Member, Tau Beta Pi National Engineering Honor Society
2007-present	Member, Alpha Eta Mu Beta National Biomedical Engineering Honor Society
2012-present	Member, Biomedical Engineering Society (BMES)
2012-present	Member, American Heart Association (AHA)

Abstracts Presented at National or International Conferences

1. M.L. Rexius, T. de Groot (2009**).** *A Thermoplastic Micro-Electro-Mechanical System (MEMS) for Microfluidic Diagnostic Platforms*. 24th Annual Senior Design Project Conference, Boston, MA.
2. M.L. Rexius, Y. Zhang, A. B. Malik, J. Rehman, and D. T. Eddington (2012). *Studying the Vascular Endothelium and Mesenchymal Stem Cells in an Oxygen Landscape.* Stem Cell and Regenerative Medicine Symposium, Chicago, IL.
3. M.L. Rexius, P. Toth, N. Chandel, A. B. Malik, D. T. Eddington, and J. Rehman (2013). *An Oxygen Gradient Landscape Generated in a Microfluidic Device Demonstrates Crosstalk between Normoxic and Hypoxic Stem Cells*. International Society for Stem Cell Research 11th Annual Meeting, Boston, MA.
4. M. L. Rexius, A. B. Malik, J. Rehman, and D. T. Eddington (2012). *Creating an Oxygen Landscape for the Vascular Endothelium and Mesenchymal Stem Cells.* Biomedical Engineering Society 2012 Annual Meeting, Atlanta, GA.
5. M. L. Rexius, A. B. Malik, D. T. Eddington, and J. Rehman (2013). *An Oxygen Gradient Landscape in a Microfluidic Device for Cell Culture*. National Clinical and Translational Sciences Predoctoral Programs Meeting, Rochester, MN.
6. M.L. Rexius, J. Rehman, A.B. Malik, and D.T. Eddington. (2013). *Paracrine Interactions between Normoxic and Hypoxic Stem Cells in a Microfluidic Oxygen Landscape Alter VEGF Transcription*. Biomedical Engineering Society 2013 Annual Meeting, Seattle, WA.
7. M.L. Rexius, Z. Wang, S.C. Oppegard, J. Cheng, J. Rehman, and D.T. Eddington (2013). *Large-Area Open-Well Oxygen Landscapes via Microfluidic Networks for Biological Analysis*. The 17th International Conference on Miniaturized Systems for Chemistry and Life Sciences (μTAS), Freiburg, Germany.
8. M.L. Rexius, D.T. Eddington, and J. Rehman (2014). *Oxygen Landscape Microfluidic Platform Demonstrates Crosstalk Between Normoxic and Hypoxic Endothelial Cells.* The 18th International Conference on Miniaturized Systems for Chemistry and Life Sciences (μTAS), San Antonio, TX.
9. M.L. Rexius, D.T. Eddington, and J. Rehman (2014). *Microfluidic Oxygen Control Demonstrates Crosstalk Between Normoxic and Hypoxic Stem Cells*. Great Lakes Chapter ASPET Regional Meeting, North Chicago, IL.

10. M.L. Rexius-Hall, D.T. Eddington, and J. Rehman (2016). *Cold-temperature Induced Transcriptional Regulation of Thermogenesis in Human Adipocytes*. Cell Symposium: Transcription and Development (and Disease). Chicago, IL.
11. M.L. Rexius-Hall, S. Uchiyama, D.T. Eddington, and J. Rehman (2017). *Glycolysis is Required for Rapid Adipocyte Thermogenesis Induced by Cold Stress*. Experimental Biology. Chicago, IL.

Patents

Eddington D.T., Mauleon G., Lo J.F., **Rexius M.L.**, and Rehman J. Microfluidic device and method for modulating a gas environment of cell cultures and tissues. US Patent App. 13/840,570.

Peer-reviewed Publications

1. Brennan M.D., **Rexius-Hall M.L.**, Elgass L.J., and Eddington D.T. Oxygen control with microfluidics. *Lab on a Chip* 14 (22): 4305-4318, 2014.
2. **Rexius-Hall M.L.**, Mauleon G., Malik A.B., Rehman J., and Eddington D.T. Microfluidic platform generates oxygen landscapes for localized hypoxic activation. *Lab on a Chip* 14 (24): 4688-4695, 2014.
3. Brennan M.D., **Rexius-Hall M.L.**, and Eddington D.T. A 3D-printed oxygen control insert for a 24-well plate. *PLOS ONE* 10 (9): e0137631, 2015.
4. **Rexius-Hall M.L.**, Rehman J., and Eddington D.T. Linear oxygen gradient microdevice demonstrates multiple thresholds of HIF1α and HIF2α activation. (Under review).
5. **Rexius-Hall M.L.**, Uchiyama S., Olenchock B., Eddington D.T., and Rehman J. Glycolysis is required for rapid adipocyte thermogenesis induced by cold stress. (In preparation).

Other Publications

1. Wei J., Kofke M., **Rexius M.**, Singhal S., Wang Y., and Waldeck D.H. Nano-plasmonics sensing and integration with microfluidics for a lab-on-chip biosensor. Technical Proceedings of the 2011 Nsti Nanotechnology Conference and Expo 3: 79-82, 2011.
2. **Rexius M.L.**, Zhang W., Oppegard S.C., Cheng J., Rehman J., and Eddington D.T. Large-area open-well oxygen landscapes via microfluidic networks for biological analysis. Technical Proceedings of 17th International Conference on Miniaturized Systems for Chemistry and Life Sciences 3: 401-404, 2013.
3. Chen K., **Rexius M.**, and Eddington D.T. Analyzing the behavior of normoxic and hypoxic cells through the use of microfluidic devices. Journal of Undergraduate Research 6: 6-10, 2013.
4. **Rexius M.L.**, Eddington D.T., and Rehman J. Oxygen landscape microfluidic platform demonstrates crosstalk between normoxic and hypoxic endothelial cells. Technical

Proceedings of 18th International Conference on Miniaturized Systems for Chemistry and Life Sciences 4: 651-654, 2014.